

Dissertation

zur Erlangung des akademischen Grades

doktor rerum naturalium (Dr. rer. nat.)

Monte Carlo Simulations for Dosimetry and Treatment Planning in Hadron Therapy

vorgelegt der

Mathematisch-Naturwissenschaftlich-Technischen Fakultät
(mathematisch-naturwissenschaftlicher Bereich)

der Martin-Luther-Universität Halle-Wittenberg

von Frau

Dipl.-Phys.(Med.) Katrin Henkner
geb. am: 16. Mai 1983 in: Grimma

Gutachter:

1. Prof. Dr. Steffen Trimper, Halle
2. Prof. Dr. Oliver Jäkel, Heidelberg
3. Prof. Dr. Dirk Vordermark, Halle

Halle (Saale), 05.02.2010

This PhD thesis was carried out between

October 2006 and September 2009

at the

Heavy Ion Therapy Research Group
German Cancer Research Center (DKFZ)
Heidelberg, Germany

and at the

Physics Research Group
Massachusetts General Hospital (MGH)
Boston, USA

Zusammenfassung

Strahlentherapie mit geladenen Teilchen ermöglicht eine sehr viel präzisere Bestrahlung von Tumoren bei gleichzeitiger Schonung von gesundem Gewebe als dies mit Photonen möglich ist. Die Reichweite von Ionenstrahlen in Gewebe oder anderen Medien, sowie Dosisverteilungen werden anhand von computertomografischen (CT) Aufnahmen der Zielregion im Bestrahlungsplanungssystem berechnet. In der klinischen Routine werden dazu Näherungsalgorithmen verwendet, welche Transport und die Wechselwirkung von Teilchen mit dem Medium in kurzer Zeit, jedoch nur für Wasser berechnen. In der Dosisberechnung ergeben sich dadurch Ungenauigkeiten.

Sehr viel genauer und unter Berücksichtigung der atomaren Zusammensetzung des Mediums können Dosisverteilungen mit der Monte Carlo (MC) Methode berechnet werden. Für die Simulation von geladenen Teilchen in Medien wird in dieser Arbeit SHIELD-HIT verwendet, da es in umfangreichen Analysen mit experimentellen Daten gute Ergebnisse für Tiefendosiskurven und Fragmentverteilungen von Teilchenstrahlen lieferte.

Im Zentrum dieser Arbeit steht einerseits die Genauigkeit von MC basierten Simulationen von Tiefendosiskurven für die Therapieplanung im Vergleich zu Ergebnissen die mit dem Näherungsverfahren berechnet wurden. Insbesondere werden dabei Reichweiten und die Form der Tiefendosiskurve für Kohlenstoffionen in unterschiedlichen gewebeäquivalenten Medien und Titan mit denen in Wasser verglichen. Daraus werden Korrekturfaktoren für die Reichweite, Höhe und Breite des sogenannten Braggpeaks abgeleitet. Die Genauigkeit der Reichweitenberechnung mit MC wird maßgeblich vom Ionisierungspotential des Mediums bestimmt. Das Ionisierungspotential für das Referenzmedium Wasser wurde anhand von experimentellen Braggpeak Positionen auf einen Wert von 80.7 eV neu bestimmt und mit Literaturwerten verglichen. In einem weiteren Teil der Arbeit wird der Einfluss des Ionisierungspotentials von Wasser und Luft auf das Verhältnis der Massenbremsvermögen Wasser/Luft untersucht. Es zeigt sich, dass dieser Wert um ca. 1 % überschätzt wird und keine Konstante, wie in der Literatur angenommen, ist.

MC Programme werden primär noch nicht klinisch eingesetzt, jedoch werden sie verwendet um unter anderem Fragmentverteilungen in Medien zu berechnen. Fragmente beeinflussen die Form der Bragg Kurve und die Wirkung des Ionenstrahls im Gewebe. SHIELD-HIT wird in dieser Arbeit mit gemessenen Winkel- und Tiefenverteilungen von Kohlenstoffionen und Fragmenten eines eingestrahlt Kohlenstoffstrahls verglichen und an die Messergebnisse angepasst. Damit wird eine deutliche Verbesserung in der Berechnung der Höhe der Tiefendosiskurve und der Anzahl der Fragmente erreicht. Das Wechselwirkungsmodell für Protonen wird außerdem mit Ladungsmessungen, welche mit einem Multi Layer Faraday Cup durchgeführt wurden, verglichen. Es konnte gezeigt werden, dass Ladungsverteilungen von Kohlenstoffstrahlen keine zusätzlichen Informationen über Fragmente liefern, die über die Tiefendosis wesentlich hinausgehen.

SHIELD-HIT wurde mit zwei weiteren MC Programmen verglichen. Aus diesem Vergleich ging hervor, dass die Reichweite und die laterale Streuung mit SHIELD-HIT geringer ist, als die mit den anderen MC Programmen berechneten. Als eine direkt klinisch relevante Anwendung der in dieser Arbeit verwendeten MC Programme, wurde die Neutronenbelastung, ein Maß für das strahleninduzierte Krebsrisiko, des Patienten bei Kohlenstoffbestrahlung der Hirnregion mit dem MC Programm Geant4 untersucht.

Abstract

Radiation therapy with ions, such as protons and carbon ions, attempts to focus radiation induced damage in the tumor while sparing the surrounding healthy tissue. Dose distributions required to remove the tumor and to spare the healthy tissue are calculated with analytical algorithms according to patient computer tomography (CT) images. Analytical algorithms calculate physical processes, e.g. particle transport and electromagnetic and nuclear interactions, only in water. The processes are not calculated according to the elemental composition of the target medium, e.g. human tissue, which decreases the accuracy of the treatment. In contrast, Monte Carlo hadron transport codes calculate ranges and dose distributions according to the elemental composition of the media. Hence, nuclear and electromagnetic interactions in inhomogeneous media are considered for the calculation of dose. The MC code used in this work is SHIELD-HIT and was successfully applied to heavy ion therapy which qualifies it for the studies in this dissertation.

Within the focus of this work is the accuracy of MC absorbed dose and range calculations in water, tissue equivalent media and titanium compared to the analytical model. In particular, correction factors are derived describing the differences in range and depth-dose curve parameters in these media between MC and the analytical algorithm.

The accuracy of range calculations with MC is mainly affected by the mean ionization potential (I-value) of the medium and its accuracy. Here, the I-value of water is revised from newly experimental Bragg peak positions to be 80.7 eV and is compared to data from the literature. Furthermore, its influence on the water-to-air stopping power ratio is studied.

MC programs are not clinically used since the calculation time is not practical yet, but they are used to calculate fragment distributions. Fragments influence the shape of the depth-dose curve and the response of the tissue to the radiation. To improve fragment calculations with SHIELD-HIT, it is benchmarked to differential cross sections from primary carbon ions. Considerable improvements in depth-dose curve and differential cross section calculations are achieved by adjusting SHIELD-HIT results to measured data.

SHIELD-HIT calculations are compared to charge measurements from a Multi Layer Faraday Cup for protons. For carbon ions the Multi Layer Faraday Cup is not sensitive to fragments, which makes it less useful for benchmarks.

An estimation on MC program specific model implementations is determined in a comparison to two other codes used in heavy ion therapy. Calculated ranges are shifted toward lower depth and the lateral scattering is less with SHIELD-HIT.

Furthermore, preliminary data of the dose from secondary neutrons in human phantom geometries, calculated with Geant4 for carbon ion therapy in the brain region is shown.

Contents

List of Abbreviations	i
List of Figures	iii
List of Tables	ix
1 Introduction	1
2 Materials and Methods	5
2.1 Interactions of charged particles with matter	5
2.1.1 The Stopping Power	6
2.1.2 The Excitation Potential	7
2.1.3 Energy Straggling	8
2.1.4 Scattering Theory	9
2.1.5 The Fragmentation of Carbon Ions	9
2.2 The Monte Carlo Method	10
2.2.1 Monte Carlo Hadron Transport Codes	11
2.2.2 The Monte Carlo Code SHIELD-HIT	11
2.2.3 The Monte Carlo code Geant4	14
2.2.4 The Monte Carlo code FLUKA	14
2.3 Basics of Dosimetry	15
2.3.1 The Absorbed Dose	15
2.3.2 Parameters of a Depth-Dose Curve	16
2.3.3 Ionization Chamber Dosimetry	17
2.4 Basics of Treatment Planning	19
2.4.1 Treatment Delivery Systems	19
2.4.2 Heavy Ion Radiotherapy at GSI	20
2.4.3 The Beam Model at GSI	22
2.4.4 The Water Equivalent Path Length	23
2.5 Performed Measurements	24
2.6 Monte Carlo Simulations for Dosimetry	26
2.6.1 Determination of the I-value for Water	26
2.6.2 The I-Value for Compounds	27
2.6.3 The Water-to-Air Stopping Power Ratio	27
2.6.4 Required Size of a Water Tank for Dosimetry	27
2.7 Monte Carlo Simulations for Treatment Planning	29
2.7.1 Benchmark on the Measurements at GSI	29
2.7.2 Simulations on the Water Equivalent Path Length	29
2.7.3 A Scaling Method for Carbon Ion Depth-Dose Curves	29
2.8 A Dose Comparison of SHIELD-HIT to Geant4 and FLUKA	31
2.9 Benchmark of SHIELD-HIT08	32

2.9.1	The Influence of PARLEV(39) on the Fragmentation Process	32
2.9.2	Test of the Total Inelastic Cross Section with a Multi Layer Faraday Cup	32
2.9.3	Benchmark of Differential Cross Sections of Fragments	34
2.10	Neutron Equivalent Dose from Carbon Ion Treatment	35
3	Results	37
3.1	Determination of the mean I-Value for Water	37
3.2	The Accuracy of the mean I-Value for Compounds	38
3.3	The Water-to-Air Stopping Power Ratio	38
3.4	Required Size of a Water Tank for Dosimetry	41
3.5	Depth-Dose Distributions Measured at GSI	42
3.6	The Water Equivalent Path Length	44
3.7	Scaling Method for Carbon Ion Depth-Dose Curves	46
3.8	Comparison of SHIELD-HIT to Geant4 and FLUKA	49
3.8.1	Depth Distributions for Protons and Carbon Ions	49
3.8.2	Beam Profiles for Protons and Carbon Ions	54
3.9	The Influence of PARLEV(39) on the Fragmentation Process	59
3.10	Test of the Total Inelastic Cross Section with an MLFC	60
3.10.1	The MLFC for a 160 MeV Proton Beam	60
3.10.2	The MLFC for Carbon Ions	61
3.11	Distributions of Fragments in a Carbon Ion Beam	62
3.12	Neutron Equivalent Dose from Carbon Ion Treatment	72
4	Discussion	73
4.1	Monte Carlo Simulations for Dosimetry	73
4.1.1	The I-Value for Water and other Media	73
4.1.2	The Water-to-Air Stopping Power Ratio	74
4.1.3	Lateral Water Tank Length	75
4.2	Monte Carlo Simulations for Treatment Planning	76
4.2.1	GSI Measurements and the WEPL	76
4.2.2	Carbon Ion Beam Depth-Dose Curve Scaling	77
4.3	Comparison of SHIELD-HIT to Geant4 and FLUKA	80
4.3.1	Depth Distributions	80
4.3.2	Beam Profiles	82
4.4	Benchmark of SHIELD-HIT	82
4.4.1	The MLFC for Protons and Carbon Ions	82
4.4.2	Distributions of Fragments in a Carbon Ion Beam	83
4.5	Neutron Equivalent Dose from Carbon Ion Treatment	84
5	Conclusions and Outlook	85
	Bibliography	89
A	Comparison of MC codes	I
B	Depth Distributions measured at GSI	III
C	Deviations between Measured and Simulated Angular Distributions	V

D	Data Table from ICRU37 and 44	VII
E	Data Table from Gammex Phantom Descriptions	IX
F	Data Table from ICRU49	XI
G	Publications resulting from this thesis	XIII

List of Abbreviations

CT	Computer Tomography
CSDA	Continuous Slowing Down Approximation
D	Dose, A Dosimetric Quantity as a Measure of the Cell Damage
DEW	Distal Edge Width
EM	Electromagnetic
FWHM	Lateral Full Width at Half Maximum of the Beam
FWHM _{BC}	Full Width at Half Maximum of the Bragg Peak
GSI	Helmholtzzentrum für Schwerionenforschung mbH Darmstadt, Germany
Gy	Gray, Unit of the Dose
HU	Hounsfield Unit, Unit of CT values
I_x or I-value	Mean Excitation Potential of the Medium x
IAEA	International Atomic Energy Agency
ICRP	International Commission on Radiological Protection
ICRU	International Commission on Radiation Units and Measurements
IMRT	Intensity Modulated Radiation Therapy
MC	Monte Carlo
MeV/cm^3	Deposited Energy per Volume
MLFC	Multi Layer Faraday Cup
PED	Peak-Entrance-Dose Ratio
PTW	Physikalisch-Technische Werkstätten, Freiburg, Germany
QA	Quality Assurance
RBE	Radio Biological Effectiveness
SOBP	Spread Out Bragg Peak
$S_{w/air}$	Water-To-Air Stopping Power Ratio
TPS	Treatment Planning System
WEPL	Water Equivalent Path Length

List of Figures

1.1	Depth-dose curves for photons (blue), protons (green) and carbon ions (red) in water. Depth-dose curves for ions are also called Bragg curves.	1
1.2	Treatment plan based on CT data for a skull base tumor (pink, thick lined structure in the middle). The critical structures (red, yellow, violet, light violet and green) are organs where the dose is limited. The carbon ion field is coming from the left side of the patient. The legend on the right relates each isodose line (thin lines representing regions of constant dose) to a percentage of the prescription dose.	3
2.1	The energy loss $\Delta E = E_0 - E_1$ of particle 'A' crossing a target of atoms 'B' and thickness Δx	6
2.2	Influence of the I-value on the Bragg peak position of a 270 MeV/u carbon ion depth-dose curve in water simulated with SHIELD-HIT.	8
2.3	Depth-dose curve of a 400 MeV/u primary carbon ion beam in water simulated with SHIELD-HIT. The total dose (black), dose from all carbon isotopes (red) and primary carbons (blue) are shown in (a). In (b) lighter fragments are shown.	10
2.4	2D view of the cylindrical scoring volume to simulate a depth dependent dose distribution in SHIELD-HIT.	13
2.5	Definition of parameters describing any depth-dose curve of a particle beam.	16
2.6	Basic layout of an ionization chamber.	17
2.7	Schematic of a plane-parallel ionization chamber which integrates charge over the sensitive volume defined by the size of the measuring electrode.	19
2.8	The SOBP as a superposition of weighted single Bragg peaks. The modulation width is 60 mm at 70 mm penetration depth.	20
2.9	Particle beam scanning as used at GSI, Darmstadt and at HIT, Heidelberg.	20
2.10	Scheme of the treatment planning process at GSI, Darmstadt. It consists of three main parts. First the physical dose is optimized to the target volume, second the RBE is calculated and the biological dose is optimized and finally, the control files for the scanner system are calculated.	21
2.11	TRiP98 calculated physical and biological dose distributions (left y-axes) and RBE (right y-axes) for a carbon ion SOBP at 50 mm and 100 mm modulation width in water. The biological dose is the product of the RBE and the physical dose.	22
2.12	The concept of WEPL for Bragg curves of the same energy. The curve obtained in water (blue) and a more dense medium with dimension d (black) are shifted by the amount of the WEPL.	23
2.13	Correlation between CT Hounsfield units and the WEPL.	24

2.14	Setup for ionization chamber based depth-dose curve measurements. The beam comes through the beam exit window, passes the Bragg peak chamber, the MP3 wall, 10 mm of water, the substitute and the Roos- or Advanced Roos chamber which measure the dose.	25
2.15	The used medium samples (a) and the Bragg Peak chamber within a holder to fix it in front of the water phantom in (b). The Roos- and Advanced Roos chamber look very similar to the Bragg peak chamber and differ only in their size.	26
2.16	Relative depth-dose curves of 180 MeV and 250 MeV protons and 350 MeV/u and 450 MeV/u carbon ions. The positions of the dose scoring volumes are shown by the grey rectangles.	28
2.17	Geometry implemented in SHIELD-HIT. Geant4 and FLUKA. Within the apertures of brass, three different structures are simulated. Depth-dose curves are scored along z and beam profiles along the abscissa.	31
2.18	Picture of the MLFC as used for the experiment with 160 MeV protons.	32
2.19	The concept of the MLFC and possible events are shown in A, B and C.	33
2.20	Measurement setup used at GSI to obtain angular distributions from secondary particles of a 400 MeV/u carbon ion beam, which are not yet published.	34
3.1	I-value for water against primary beam energy, determined from experimental Bragg peak positions.	37
3.2	The water-to-air stopping power ratio for a 140 MeV proton beam with I-values according to the sets in Table 2.5.	39
3.3	Water-to-air stopping power ratio for protons of different energies in MeV simulated with set 3 and 5.	40
3.4	The stopping power ratio according to the residual range of proton beams (a) and carbon beams (b) of different energies in MeV/u for set 5. Figure 3.4 (b) is taken from [Henkner et al., 2009a] in appendix G.	41
3.5	Simulated proton dose relative to the dose for a 500 x 500 x 500 mm ³ water tank. The initial beam energy is 180 MeV in (a) and 250 MeV in (b). The abscissa shows the lateral dimension of the water tank while the depth is constant at 500 mm. The symbols in the legend belong the position of the center of the 10x10x10 mm ³ volumes on the central beam axis at 100, 200 and 300 mm depth.	41
3.6	Simulated carbon dose relative to the dose for a 500 x 500 x 500 mm ³ water tank. The initial beam energy is 350 MeV/u in (a) and 450 MeV/u in (b). The abscissa shows the lateral dimension of the water tank while the depth is constant at 500 mm. The symbols in the legend belong the position of the center of the 10x10x10 mm ³ volumes on the central beam axis at 100, 200 and 300 mm depth.	42
3.7	Measurements (squares) and SHIELD-HIT calculations (line) on the GSI experiment with samples from the Gammex phantom. Curves obtained in “water” means without samples and in “adipose”, or “cortical bone”, or “titanium” means with either of this media samples in the beam path.	43

3.8	SHIELD-HIT simulated and experimentally obtained WEPL for the first six media in Table 3.4. The thickness of the Gammex samples during measurements at GSI are 56.2 mm, and 20 mm at HIT. The thicknesses were 20, 40 and 60 mm for SHIELD-HIT simulations.	45
3.9	Measured and SHIELD-HIT simulated WEPL for cortical bone and titanium. The dimensions for cortical bone samples are the same as in Figure 3.8. The titanium sample is 2.83 mm thick in the measurements and 1, 3 and 5 mm in the simulations.	46
3.10	FWHM_{BC} against carbon ion energy in MeV/u (a) and with applied scaling (b). The γ in eq. 2.31 is 0.26 and C is 0.93 for titanium, 1.4 for inflated lung and 1.0 for all other media. The black line in (b) is within eq. 3.1.	47
3.11	The DEW before (a) and after the scaling (b). The γ in eq. 2.31 is 0.26 and C is 0.93 for titanium, 1.46 for inflated lung and 1.0 for all other media. The black line in (b) is within eq. 3.2.	48
3.12	The PED $D_{\text{peak}}/D_{\text{plateau}}$ against the initial carbon ion energy (a) and the abscissa after the scaling (b). The γ in eq. 2.31 is 0.1 and C is 0.93 for titanium and 1.0 for all other media. The black line in (b) is within eq. 3.3.	48
3.13	Energy distributions in water downstream of air for 100 and 200 MeV protons (left) and 200 and 400 MeV/u carbon ions (right). The whole water depth is shown in appendix A on page I.	51
3.14	Energy distributions in water downstream of lung/air for 100 and 200 MeV protons (left) and 200 and 400 MeV/u carbon ions (right). The whole water depth for (c) and (d) is shown in appendix A on page I.	52
3.15	Energy distributions in water downstream of bone/air for 100 and 200 MeV protons and 200 and 400 MeV/u carbon ions. The whole water depth for (c) and (d) is shown in appendix A on page I.	53
3.16	Beam profiles at 50 mm depth with SHIELD-HIT (black), Geant4 (blue) and FLUKA (orange) downstream of interfaces from Figure 2.17. On the left for 100 MeV protons and on the right for 200 MeV/u carbon ion beams.	56
3.17	Beam profiles at 50 mm depth with SHIELD-HIT (black), Geant4 (blue) and FLUKA (orange) downstream of interfaces from Figure 2.17. On the left for 200 MeV protons and on the right for 400 MeV/u carbon ion beams.	57
3.18	Beam profiles at 100 mm depth with SHIELD-HIT (black), Geant4 (blue) and FLUKA (orange) downstream of interfaces from Figure 2.17. On the left for 200 MeV protons and on the right for 400 MeV/u carbon ion beams.	58
3.19	Influence of PARLEV(39) on the depth distribution for a 270 MeV/u primary carbon ion beam. PARLEV(39)=0.8 is shown in red and PARLEV(39)=1.0 in blue in (a). The histograms in (b) show the ratio between both PARLEV values depending on the generation of particles.	59
3.20	Results from calculations and measurements on the MLFC for SHIELD-HIT in (a) and (c), and Geant4 in (b) and (d). The abscissa is in absolute values. The semi logarithmical scale in (c) and (d) is used to show the influence of electromagnetic interactions.	61
3.21	Shown are the charge distributions of particles of different generation against channel number. For a 270 MeV/u primary carbon ion beam PARLEV(39) is set to 1.0 and 0.8 in (a) and (b), respectively. The ordinate is shown up to 60 pC/(10^9 ^{12}C).	62

3.22	The difference of the charge for a 270 MeV/u primary carbon ion beam with PARLEV(39)=0.8 and 1.0. The charge from all particles and primary carbon ions in (a) and from different generations in (b).	62
3.23	Depth distributions derived from the measurements and calculations are shown in (a). The dash-dotted lines in blue show the positions (59, 159, 258, 279 and 347 mm) where the angular distributions of the fragments are obtained. The number of carbon ions normalized to the number of incident particles against water depth is shown in (b).	63
3.24	Angular distributions of carbon ions simulated with SHIELD-HIT (straight) and measured (dots) for water depth of 159 mm and 258 mm. The colors refer to the parameters given in Table 3.9.	64
3.25	In (a) to (d) the differential cross sections of hydrogen fragments are demonstrated. The abscissa shows number of hydrogen fragments N normalized to the number of incident particles N_0 per solid angle sr. In (e) the number of fragments, integrated between $0^\circ - 10^\circ$, are shown against water depth. The colors refer to the parameters given in Table 3.9. . . .	67
3.26	In (a) to (d) the differential cross sections of helium fragments are demonstrated. The abscissa shows number of helium fragments N normalized to the number of incident particles N_0 per solid angle sr. In (e) the number of fragments, integrated between $0^\circ - 10^\circ$, are shown against water depth. The colors refer to the parameters given in Table 3.9.	68
3.27	In (a) to (d) the differential cross sections of lithium fragments are demonstrated. The abscissa shows number of lithium fragments N normalized to the number of incident particles N_0 per solid angle sr. In (e) the number of fragments, integrated between $0^\circ - 10^\circ$, are shown against water depth. The colors refer to the parameters given in Table 3.9.	69
3.28	In (a) to (d) the differential cross sections of beryllium fragments are demonstrated. The abscissa shows number of beryllium fragments N normalized to the number of incident particles N_0 per solid angle sr. In (e) the number of fragments, integrated between $0^\circ - 10^\circ$, are shown against water depth. The colors refer to the parameters given in Table 3.9. . . .	70
3.29	In (a) to (d) the differential cross sections of boron fragments are demonstrated. The abscissa shows number of boron fragments N normalized to the number of incident particles N_0 per solid angle sr. In (e) the number of fragments, integrated between $0^\circ - 10^\circ$, are shown against water depth. The colors refer to the parameters given in Table 3.9.	71
3.30	Geant4 simulated neutron equivalent doses from initial carbon beams for several organs of an eleven year old male phantom irradiated in the brain.	72
3.31	Geant4 simulated neutron equivalent doses from proton beams for several organs of an eleven year old male phantom irradiated in the brain. The neutron equivalent dose shown here is only from neutrons produced inside the patient.	72
4.1	Comparison of old and new ICRU73 stopping power data. The ratio of new and old ICRU73 stopping power data is shown in (a) and the resulting depth distributions for a 270 MeV/u carbon ion beam in (b).	74

4.2	Bragg curves for a 300 MeV/u carbon ion beam after applying the WEPL scaling. The deposited energy is normalized to the maximum against water depth in (a), which is shown only up to 0.8, and in absolute deposited energy in (b).	78
4.3	SHIELD-HIT calculations (PARLEV(39)=0.8) and measurements of a 270 and 330 MeV/u primary carbon ion beam in (a). SHIELD-HIT overestimates the fragment tail but describes the peak height very well.	82
4.4	Influence of PARLEV(34) and (33) on the Bragg curve for a 400 MeV/u carbon ion beam. The deposited energy is increased in the tail region up to 5 % for values of 17 and 0.3 for PARLEV(34) and (33) in green.	84
A.1	MC simulated proton and carbon ion depth-dose curves in water downstream of air in (a) and (b), lung/air for 200 MeV protons in (c) and 400 MeV/u carbon ions in (d) and bone/air in (e) and (f).	I
B.1	Measurements (squares) and SHIELD-HIT calculations (line) on the GSI experiment with samples from the Gammex phantom. Black and blue colored curves represent the data for the Advanced Roos chamber and grey and orange curves for the Roos chamber.	III

List of Tables

2.1	Overview of published mean excitation potentials for water I_w	8
2.2	Contribution of particles to dose on the integral dose for a 400 MeV/u carbon ion beam in water.	9
2.3	Main characteristics of the ionization chambers which are used for the measurements.	25
2.4	Maximum uncertainty of the mean I-value as given in ICRU49 and 37.	27
2.5	An overview of the combination of I-values for water and air, which are used for stopping power ratio calculations. The set numbers are taken from Table II on page 1232 in [Henkner et al., 2009a] for comparison.	28
3.1	Measured minus calculated ($I_w=67.2$ eV) Bragg peak positions and the I-values required in SHIELD-HIT to achieve the measured positions. Values in brackets are errors from the fit in 2.6.1.	38
3.2	Shift of simulated 270 MeV/u carbon ion beams in a medium according to the uncertainty in the I-value of ICRU.	39
3.3	I-values obtained from the comparison of measured and simulated depth-dose curves downstream of different media in water.	42
3.4	Density and WEPL for various media obtained from measurements at GSI and HIT and SHIELD-HIT simulations. The WEPL for SHIELD-HIT is the arithmetic mean and the standard deviation in brackets. The last column shows the difference between the mean WEPL with SHIELD-HIT and the mean WEPL from the experiments.	44
3.5	Calculated effective atomic charge Z_m for the studied media.	46
3.6	Mean shift of Bragg peaks from protons and carbon beams downstream of different media from Figure 2.17. The shift is determined at the root position of the lateral fall-off with SHIELD-HIT (S) minus Geant4 (G) or FLUKA (F).	50
3.7	Maximum difference in the profiles in % for Geant4 and FLUKA compared to SHIELD-HIT. The 's' means within statistical uncertainties of 1.5 % and the direction '+' and '-' over- and underestimation of the SHIELD-HIT results.	55
3.8	Difference in the penumbra determined at the 80% and 20% position of deposited energy for SHIELD-HIT (S) to Geant4 (G) and FLUKA (F). For positive values the penumbra of Geant4 or FLUKA is smaller than with SHIELD-HIT and vice versa.	55
3.9	SHIELD-HIT setup to simulate angular distributions. One setup belongs to one color, which is afterwards used in Figures 3.23 to 3.29. The I-value for water is always set to 80.8 eV.	63
3.10	Deviations between SHIELD-HIT and the experiment at about 0° and 2° for set A and D (± 3 %).	65

3.11	Deviations of calculated to measured differential cross sections for various water thicknesses for set A and D ($\pm 3\%$).	66
4.1	FWHM _{BC} and PED from Figure 4.2 in comparison to that weighted from the scaling in 3.7. The values for water in comparison are 6.22 mm and 5.24 or the FWHM _{BC} and PED. The values in brackets show percentage deviation to the values in water.	79
4.2	Mean root position and standard deviation in brackets derived from protons (P) and carbon ions (C) traveling through air.	80
C.1	Deviation between SHIELD-HIT data (set A) and the experiment at angles of 0° and 2° and various water depth. The value is rounded up and gives only an estimation on the differences.	V
D.1	Density, mean excitation energy and compositions of media from ICRU37.	VII
D.2	Density, mean excitation energy and compositions of inflated lung from ICRU 44.	VIII
E.1	Mass density and compositions of media according to the Gammex phantom 467.	IX
F.1	Excitation energy for several elements and compounds according ICRU49. The <i>I</i> for liquids and solids not listed in the table, the elemental values times 1.13 are used.	XI

1 Introduction

Radiation therapy, along with surgery and chemotherapy, is one of the three main modalities for cancer therapy. Conventional treatment with photons uses 3-dimensional conformal radiation therapy, while a more advanced technique is Intensity Modulated Radiation Therapy (IMRT). Therapy with heavy charged particles offers a considerable improvement compared to photons for treating deep seated or radio resistant tumors due to their beneficial depth-dose curve, see Figure 1.1.

These depth-dose curves show relative dose against penetration depth of a particle field in water. The dose describes the amount of absorbed energy in a medium and is a measure of the cell damage. The main differences between ions, e.g. protons and carbon,

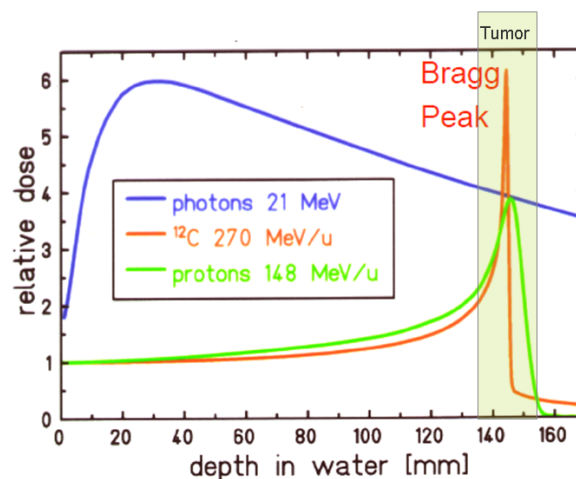


Figure 1.1: Depth-dose curves for photons (blue), protons (green) and carbon ions (red) in water. Depth-dose curves for ions are also called Bragg curves.

and photons are the position, width and height of the dose maximum. The dose outside of the maximum is smaller for ions than for photons.

Depending on the initial beam energy, the maximum dose for photons is only up to 40 - 50 mm in depth, whereas for ions, known as the Bragg peak, it can be shifted toward 300 mm depth by increasing the primary particle energy. For treatments of deep seated tumors the number of beam directions (up to 7, depending on the tumor) is large for photons, because the required dose in the tumor is achieved only by adding up depth-dose distributions from various beam directions. For ions fewer beam directions are needed, because the maximum dose can be adjusted by the primary beam energy to the depth of the tumor. However, there is a difference in the depth-dose curves between proton and carbon ions as well. The lateral scattering and energy straggling (width of the Bragg peak) is smaller for carbon ions, which increases the dose maximum compared

to protons. The dose tail with carbon ions downstream of the Bragg peak comes from lighter fragments (hydrogens up to boron) which occur while the carbon beam traverses through the medium. Another advantage of carbon ions compared to protons is the increase of the ionization density in the Bragg peak. This increases the radiobiological effectiveness (RBE), which describes the response of the tissue to the radiation. With carbon the RBE increases toward the particle range while with protons the RBE is constant. Hence, less dose is needed with carbon ions than with protons for the same tissue response and the dose in the entrance region is smaller for carbon than for protons.

[Wilson, 1946] noted the potential of protons and heavier ions for radiation treatment while working at the Harvard Cyclotron Laboratory. Besides the double scattering method [Koehler et al., 1977], physicists and engineers at the Lawrence Berkeley Laboratory (LBL) developed the raster scan technique to conform the radiation field to the tumor. This technique was first successfully applied clinically at GSI (Helmholtzzentrum für Schwerionenforschung mbH Darmstadt, Germany) in 1997 and is now used at HIT (Heidelberg Ion beam Therapy Center, Germany [Jäkel et al., 2007]). In a scanning system [Haberer et al., 1993], the beam is deflected by orthogonal magnetic fields in two dimensions. Compared to a scattering technique, the scanning is more precise and does not need additional material in the beam path to adjust the beam shape to the shape of the tumor. The penetration depth is varied by varying the primary particle energy in the synchrotron.

More than 430 patients had been treated at GSI since 1997. About 50 % were patients with chordomas, which are slow-growing tumors around the neuroaxis and arise from the skull base or the spine. The tumor is relatively radio resistant and therefore preferred for carbon ion treatment. Other examples of treated tumors are chondrosarcomas (from cartilage), adenoid cystic carcinoma (ACC) in the head and neck region and bone or prostate tumors. Moving tumors, like lung tumors, which move with breath or heartbeat are not treated yet.

Several steps are required for treatment planning in general. First, a CT scan of the tumor area is made on which the tumor and critical structures are outlined and the maximum dose is prescribed. After defining the beam directions, the dose distributions are calculated with a computer system using a special treatment planning software.

An example of a treatment plan is shown in Figure 1.2. In this CT slice, the outer border of the tumor and the critical structures, where dose is to be avoided, are contoured with thick lines. The tumor lies within the large, almost rectangular pink contour. The isodoses, lines of constant dose, are represented according to the color scale on the right by thin lines. The legend on the right shows percentage of the reference dose (mean dose in the tumor). Here, the beam comes from the left side of the patient (right side in the figure) and covers the tumor volume by a superposition of single Bragg curves of different energies.

The largest energy is chosen corresponding to the water equivalent range of ions required to stop at the distal part of the tumor (farthest boundary of the tumor from the beam entrance). The smallest energy is chosen upon the water equivalent range to the boundary closest to the beam entrance. To prevent dose damage in critical structures of healthy tissue the dose in these structures is limited. Figure 1.2 shows that high accuracy is needed to calculate the dose and the range of the ion beams to successfully kill the tumor cells and spare the healthy tissue. If the range is not calculated correctly an under dosage in the tumor can cause a recurrence of the tumor, while an over dosage in the healthy tissue can cause side effects. The treatment plan in Figure 1.2 is not the

final one, but shows the necessity of accurate calculations on, e.g. the range and lateral scattering. A second opposing beam is used for treatment to better spare the critical structures and to decrease effects of dose uncertainties.

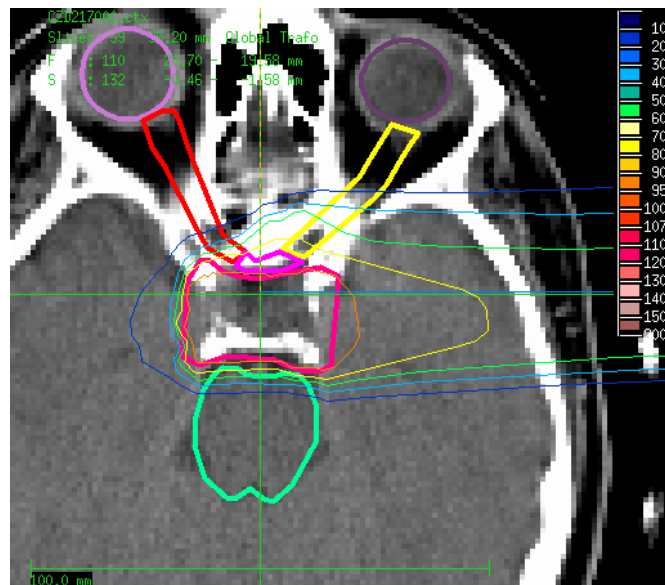


Figure 1.2: Treatment plan based on CT data for a skull base tumor (pink, thick lined structure in the middle). The critical structures (red, yellow, violet, light violet and green) are organs where the dose is limited. The carbon ion field is coming from the left side of the patient. The legend on the right relates each isodose line (thin lines representing regions of constant dose) to a percentage of the prescription dose.

The most accurate method to calculate dose distributions and to benefit from the increased dose conformity and biological effectiveness from ion radiotherapy, is the Monte Carlo (MC) method, which is already clinically used for photons. In hadron therapy, in contrast, the particle transport and nuclear- and electromagnetic interactions are more complex and MC hadron transport codes are still under development.

Instead, pencil beam algorithms are used as an approximation. They treat different media as water of different densities and are therefore much faster than MC codes. However, they do not calculate the particle transport and interactions according to the elemental composition like MC hadron transport codes do. Hence, MC hadron transport codes are more accurate in the calculation of particle spectra, especially in inhomogeneous media which will improve the accuracy of treatment planning.

In this dissertation the MC code SHIELD-HIT [SHIELD-HIT, 2008] is used. It was successfully applied to heavy ion therapy, which qualifies it for the following studies in this work:

1. SHIELD-HIT is used to further improve range and dose calculations in various media as well as dose measurements with ionization chambers. Therefore, the following studies have been performed:
 - The I-value published for water is revised. Because there is an inconsistency of data observed from publications, the influence of the I-value for water on the range of particle beams is studied. Furthermore, the I-value for water is revised from newly experimentally Bragg peak positions. (2.6.1)

- The effect of inaccuracies given for the published I-values on the range calculated with SHIELD-HIT is studied for water, titanium and several tissue equivalent media. Furthermore, a comparison to experimental depth-dose curves as well as the effect of media inhomogeneities is studied. (2.6.2)
 - The influence of the I-value of water on the water-to-air stopping power ratio is studied. The water-to-air stopping power ratio is recalculated from the newly derived I-value for water to improve ionization chamber dosimetry. (2.6.3)
 - The minimum side length of a water tank used to measure the dose of a particle beam under special conditions in ion beam quality assurance is compared to photons. (2.6.4)
 - The I-values for adipose, cortical bone and titanium are revised from depth-dose curve measurements. From these measurements the effect of inhomogeneities on depth-dose curves is studied in a comparison to SHIELD-HIT results. (2.7.1)
2. The main focus in the treatment planning chapter is a comparison of depth-dose curves calculated with SHIELD-HIT and the pencil beam model as used in treatment planning. To benefit from ion therapy several scaling factors are derived from SHIELD-HIT calculations which can be applied on the pencil beam model in order to improve their accuracy.
 - The already established concept of a constant water equivalent path length (WEPL) for a medium is studied toward primary beam energy and media thickness dependency with SHIELD-HIT. (2.7.2)
 - The shape of depth-dose curves obtained in homogeneous media for various carbon ion beam energies is studied. From these distributions a scaling to obtain water equivalent depth-dose curve parameters is developed. The scaling is afterward discussed for inhomogeneous media. (2.7.3)
 3. To estimate MC program specific model implementations, SHIELD-HIT is compared to Geant4 and FLUKA, two other codes used in ion therapy. Therefore, depth-dose curves and lateral beam profiles are calculated according to the same geometry, media and initial beam parameters. (2.8)
 4. To increase the accuracy of simulating fragments from nuclear interactions needed for radiobiological calculations, the total inelastic cross section in SHIELD-HIT is compared to charge measurements from a Multi Layer Faraday Cup (MLFC) for protons. For carbon ions, SHIELD-HIT is used to study the sensitivity of the MLFC to fragmentation. To estimate the accuracy of SHIELD-HIT calculated differential cross sections of a carbon ion beam, a comparison to measured data downstream of a water phantom is made. A significant improvement in the calculations of depth-dose and fragment distributions is achieved by adjusting three free parameters relating to different physical models. (2.9)
 5. As a directly clinically relevant application of MC hadron transport codes, neutron equivalent doses are calculated for carbon ion treatment plans with Geant4 in comparison to the same planes for proton treatments.

2 Materials and Methods

This chapter contains in the first part theoretical aspects of the physics of ions, the Monte Carlo (MC) method and the basics of dosimetry and treatment planning (2.1 to 2.4). In the second part it describes measurements performed in this work as well as applications of MC calculations for dosimetry and treatment planning. Furthermore, it introduces the methods of a comparison of MC codes as well as a comprehensive benchmark study to experimental charge distributions and differential cross sections (2.5 to 2.9).

2.1 Interactions of charged particles with matter

Charged particles like electrons, protons or carbon ions undergo electromagnetic interactions with target electrons and atomic nuclei. Generally, various reaction channels may be realized when a particle 'A' travels through a medium of atoms 'B'. These are:

- $A+B \rightarrow A+B$: elastic scattering
- $A+B \rightarrow A'+B^*$: inelastic scattering with excitation of the atom
- $A+B \rightarrow A'+B^*+e$: inelastic scattering with ionization of the atom
- charge exchange, fragmentation, bremsstrahlung, etc.

The probability of an A+B interaction is characterized by the total effective cross section σ . It is the sum of the total elastic and inelastic cross section:

$$\sigma = \sigma_{el} + \sigma_{inel} \quad (2.1)$$

The inelastic scattering cross section, or partial cross sections σ_n , arises from the sum over of excitation processes of discrete levels of an atom n and ionization of the atom by:

$$\sigma_{inel} = \sum_{n \neq 0} \sigma_n = \sigma_{excit} + \sigma_{ioniz} \quad (2.2)$$

From the hypothesis of independent successive collisions, the ionization loss of a particle 'A' traveling through a medium equals the sum of the excitation of individual atoms 'B'. According to Figure 2.1 the particle loses a certain amount of energy ($\epsilon_n - \epsilon_0$) when traveling through a medium of thickness Δx . This energy ionizes the atoms, which undergo a transition from the ground state $|0\rangle$ into a discrete excited state $|n\rangle$. The energy loss ΔE of ΔN number of inelastic collisions in a thin layer Δx is expressed by:

$$\Delta E = (\epsilon_n - \epsilon_0) \Delta N_n \quad (2.3)$$

With $\Delta N = n_0 \sigma_n \Delta x$, defined in terms of the partial cross sections σ_n and the electron density, the energy loss becomes:

$$-\frac{dE}{dx} = -\frac{\Delta E}{\Delta x} \Big|_{\Delta x \rightarrow 0} = n_0 \sum_n (\epsilon_n - \epsilon_0) \sigma_n \quad (2.4)$$

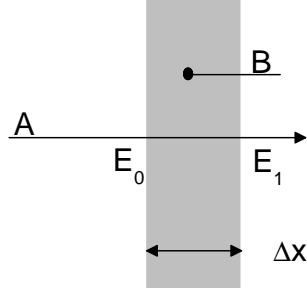


Figure 2.1: The energy loss $\Delta E = E_0 - E_1$ of particle 'A' crossing a target of atoms 'B' and thickness Δx .

2.1.1 The Stopping Power

The stopping power is defined as the energy loss per unit distance traversed and is given by $S = -dE/dx$, where E is the particle energy and x is the path length [ICRU49, 1993]. It was first calculated by Bohr and later by Bethe and Bloch using quantum mechanical approaches and is finally expressed by:

$$S = -\frac{dE}{dx} = \frac{4\pi Z_p^2 e^4}{m_e v^2} n_0 \left[\ln \left(\frac{2m_e v^2}{I} \right) + \ln \left(\frac{1}{1 - \beta^2} \right) - \beta^2 - \delta \right] \quad (2.5)$$

Z_p is the charge of the projectile, m_e the electron mass, v the velocity of the particle and $\beta = v/c$. $n_0 = N_A Z_m \rho / A$ is the electron density of the target medium where N_A is the Avogadro constant, Z_m the atomic number, ρ the mass density and A the atomic mass of the target. I is the mean excitation potential of the target medium.

The relativistic effect of 'compression' of the electric field of a traversing particle is described by the factor $\ln(1/(1 - \beta^2)) - \beta^2$ and enhances the effective stopping power. The term δ corrects for the polarization of the medium.

For low energies, the projectile can pick up electrons from the target which reduces its velocity [Hubert et al., 1989]. This effect is described by the reduced relative velocity η according to the velocity stripping criterion in [Brandt, 1975] and [Yarlagadda et al., 1978] by:

$$\eta = \frac{v_p}{v_0} Z_p^{-\gamma}, \quad (2.6)$$

where v_p is the ion velocity, v_0 the Bohr velocity and Z_p the charge of the projectile. The γ is determined from experimental findings to 2/3. The scaling factor η is used in 2.3.2 as a scaling factor for carbon ion depth-dose curves.

Usually the mass stopping power $S/\rho = -(1/\rho)(dE/dx)$ is used, which was introduced

to eliminate mass density effects on the stopping power. The stopping power is the basis of simulating the energy loss of charged particles in Monte Carlo hadron transport codes (see 2.2), from which ranges and doses of ions in media are calculated. Due to the rapid dose fall-off behind the Bragg peak for ions, it is very important to calculate correct stopping power values.

The range R or maximum penetration depth of an ion of initial energy E_0 in a medium in the “Continuous Slowing Down Approximation” (CSDA) is defined from the inverse stopping power S . In the CSDA, carbon ions are assumed to lose their energy continuously along their path length.

$$R = \int_0^{E_0} \left(\frac{dE}{dx} \right)^{-1} dE = \int_0^{E_0} (S)^{-1} dE \quad (2.7)$$

The dose D to a medium is calculated from the stopping power and energy fluence Φ by:

$$D = \int dE \cdot (S(E)/\rho)_E \cdot \Phi_E \quad (2.8)$$

2.1.2 The Excitation Potential

The I-value, I , of a medium is defined as a geometric mean of the excitation potentials of the constituent atoms, and depends on the atomic number of this medium. The I-value of an element is analytically derived from oscillator strength functions. The most frequently used method to obtain mean I-values of compounds is to determine them from experimental stopping power data using the Bethe-Bloch equation, where I is represented in a logarithmic term [ICRU49, 1993]. For compound media it can be calculated by Bragg’s additivity rule from the I-values I_i of the compound elements, by the relative weight w_i , the atomic mass A_i and the atomic number Z_i of element i , according to the following equation:

$$\ln I = \frac{\sum_i w_i Z_i / A_i \ln I_i}{\sum_i w_i Z_i / A_i} \quad (2.9)$$

The influence of the I-value for water, I_w , on SHIELD-HIT simulated depth-dose curve of a 270 MeV/u carbon ion beam is shown in Figure 2.2. An increase in I_w of 1 eV increases the depth by about 0.24 mm for 270 MeV/u carbon ions with SHIELD-HIT, and is further discussed in [Andreo, 2009].

There is a big controversy in the literature about the I-value. The International Commission on Radiation Units and Measurements (ICRU) recommends I-values for several elements and compounds and also provides stopping power values tabulated against energy. ICRU published inconsistent data for I_w . Whereas ICRU49 [ICRU49, 1993] recommends an I_w of 75 ± 3 eV for protons and helium, for all heavier particles in ICRU73 [ICRU73, 2005] the value is 67.2 eV^1 . This gives the impression that I_w from ICRU is particle dependent which is not expected from theory and not supported by publications summarized in Table 2.1. The recently published I-value for water is 80.8 eV in [Paul et al., 2007].

¹The value of 67.2 eV is calculated from the tabulated stopping power in ICRU73 in [Paul et al., 2007]

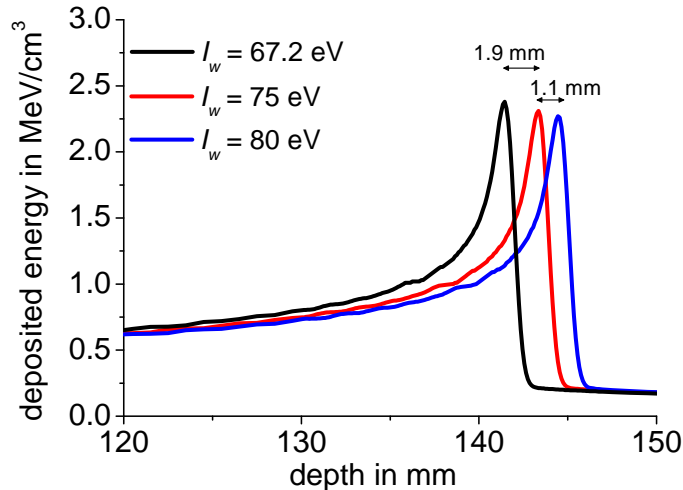


Figure 2.2: Influence of the I-value on the Bragg peak position of a 270 MeV/u carbon ion depth-dose curve in water simulated with SHIELD-HIT.

Table 2.1: Overview of published mean excitation potentials for water I_w .

I_w	Reference
67.2 eV	[ICRU73, 2005]
75 ± 3 eV	[ICRU49, 1993]
78 eV	[Schardt et al., 2008]
78.4 ± 1 eV	[Kumazaki et al., 2007]
80 eV	[Bichsel and Hiraoka, 1992]
80.8 eV	[Paul et al., 2007]

2.1.3 Energy Straggling

The Bethe-Bloch equation gives only the mean ionization loss. Actually, the ionization loss of charged particles contains fluctuations in a given layer of the medium. This phenomenon is called energy straggling. For thick targets, where the number of interactions between the projectile and the target is huge, the spread of the energy loss around its mean can be described with a Gaussian distribution ([Remizovich et al., 1988] and [Rossi, 1953]). For thin targets, the Landau-Vavilov distribution, which is asymmetric and the most likely ionization loss becomes smaller than the mean ionization loss, is more accurate [Vavilov, 1957]. The energy straggling for carbon ions is smaller than for protons, which is an effect of the projectile mass. The Bragg peak is a superposition of stopping power curves for different energies according to the local energy spectrum in depth. Furthermore, the energy spectrum from the accelerator influences the shape of the Bragg curve.

2.1.4 Scattering Theory

Scattering characterizes the deflection of particles on their way through the medium according to the Coulomb theory of multiple scattering. The differential scattering cross section $d\sigma/d\Omega$ within Rutherford's scattering theory is expressed by:

$$\frac{d\sigma}{d\Omega} = \left(\frac{1}{4\pi\epsilon_0} \frac{Z_p Z_m e^2}{2E_0} \right)^2 \frac{1}{\sin^4\left(\frac{\vartheta}{2}\right)}, \quad (2.10)$$

where Z_p and Z_m are the atomic mass of the projectile and the target, respectively. E_0 is the initial energy of the projectile, $\epsilon_0 = 8.859 \cdot 10^{-12} \frac{\text{C}}{\text{Vm}}$, and ϑ the scattering angle. The distribution of scattering angles is described by a Gaussian distribution for small angles and by Molière's theory for larger angles [Molière's, 1984]. The Gaussian distribution is identical to Molière's distribution in the first order.

2.1.5 The Fragmentation of Carbon Ions

Particles traveling through a medium do not just lose energy through inelastic interactions with the target electrons. They also undergo collisions with the target nucleus. Fragmentation processes are simplified within the abrasion-ablation model, which characterizes nuclear-nuclear interactions based on geometrical arguments [Tuli, 1987]. It describes the fragmentation as a two step process. First, the projectile and the target overlap and an excited prefragment is formed. In the second step the prefragment breaks into single nucleons and smaller complexes and the projectile evaporates nucleons until the energy falls below the binding energy.

Table 2.2: Contribution of particles to dose on the integral dose for a 400 MeV/u carbon ion beam in water.

Particle (all isotopes)	C	H	He	Li	Be	B
fraction on total dose	0.559	0.148	0.095	0.037	0.058	0.103

The contribution of fragments to the integral dose for a 400 MeV/u carbon ion beam simulated with SHIELD-HIT is shown in Table 2.2 and in Figure 2.3. The Bragg peak from primary carbon ions (blue) in (a) is more narrow than from primary and secondary carbon ions (red), and is most broad for doses from all primary and secondary particles (black).

Lighter fragments have a big impact on the shape of the dose curve. The fragment build up contributes significant to the plateau region and influences the Bragg peak. Fragments are also responsible for the dose tail downstream of the Bragg peak. Whereas the red and blue curves from carbon ions go down to zero, the total energy deposition has still a value of 24 % of the maximum dose. This dose tail comes from fragments which are lighter than carbon and therefore have a larger range. Protons and boron ions contribute about 15 % and 10 %, respectively, to the total dose from a 270 MeV/u carbon ion in the Bragg peak. The contribution from He, Li and Be is lower.

The deposited energy shows some variations between 250 and 300 mm depth in Figure

2.3 (b), which is due to the resolution of 0.01 mm to simulate the Bragg peak correctly and the resulting statistical noise (low number of primary particles). The number of fragments is very small, so even for 2.2 million primary particles the noise is significant. The step between 250 and 300 mm which is dominantly observed for H(1,1) is probably from a physical process switched on or off in the MC. Those small effects can be detected with a resolution of 0.1 mm bins, but have no influence on the total dose.

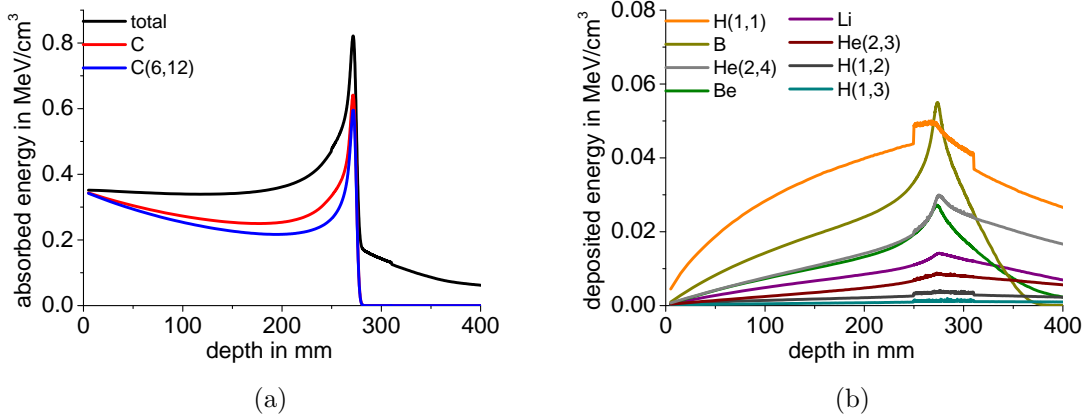


Figure 2.3: Depth-dose curve of a 400 MeV/u primary carbon ion beam in water simulated with SHIELD-HIT. The total dose (black), dose from all carbon isotopes (red) and primary carbons (blue) are shown in (a). In (b) lighter fragments are shown.

2.2 The Monte Carlo Method

The name Monte Carlo has its origin in the corresponding district of Monaco, which is famous for its casinos, and was coined in the 1940's [Metropolis and Ulam, 1949]. MC covers a class of computational algorithms which, in general, use random numbers and probability distributions to solve physical and mathematical problems numerically.

In radiotherapy, MC is used to simulate particle tracks and interaction events with the target atoms such as patients, phantoms, beam modifiers and accelerators. MC hadron transport codes calculate particle ranges (eq. 2.7) and dose distributions from the stopping power and particle fluences (eq. 2.8).

In Monte Carlo hadron transport codes the stopping power is used to calculate particle energy dependent mean free path length λ . The distance s between interactions in a medium is determined by:

$$s = -\lambda \ln(1 - \xi), \quad (2.11)$$

where ξ is a random number $0 \leq \xi \leq 1$. The type of interaction occurring after the step is sampled with another random number. It selects the interaction event, e.g. nuclear or electromagnetic interactions, depending on the relative probabilities at particle energy. The relative probability is described by the ratio of single cross sections to the total cross sections of the interactions, which are determined from experiments. From a sufficient number of particles, an average fluence distribution is derived from which the dose is

calculated. A more detailed description of the general Monte Carlo technique for photons can be found in [Andreo, 1991].

2.2.1 Monte Carlo Hadron Transport Codes

The origin of developing hadron transport codes goes back to the 1960's. The codes developed by [Barashenkov and Toneev, 1973], and the Nucleon Transport Code (NTC) by [Kinney, 1964] were based on the cascade evaporation model (CEM). It describes the nuclear collision as a superposition of nucleon-nucleon interactions. From the status of NTC further developments were brought to the Nucleon-Meson Transport code (NMTC) [Coleman and Armstrong, 1971] and SHIELD [Sobolevsky, 1970].

The most common codes in ion therapy are SHIELD-HIT [Gudowska et al., 2004], Geant4 [Agostinelli et al., 2003], FLUKA [Fasso et al., 2005], PHITS [Iwase et al., 2002] and MCNPX [Hughes et al., 1997].

2.2.2 The Monte Carlo Code SHIELD-HIT

The MC code SHIELD-HIT is based on SHIELD, which was developed in the 1970's in the Fortran programming language. The first version of SHIELD was completely rewritten in 1989-90 under Windows by N. Sobolevsky and N. Dementjev. In 1995 the code successfully passed the benchmarking of hadron transport codes by the European Atomic Energy Agency. In 1997 the code was extended to simulate atomic nuclei of different atomic mass. SHIELD was applied to several physical issues, e.g. the calculation of radiation fluxes behind the shielding of the MIR space station and the radiation damage on MIR structural materials.

With the development of ion therapy, SHIELD was extended to SHIELD-HIT (**H**heavy **I**on **T**ransport) and became a useful calculation tool for particle therapy. A detailed description of the capabilities of SHIELD and SHIELD-HIT is found in [SHIELD-HIT, 2008]. The main features and improvements of SHIELD-HIT compared to SHIELD are:

- Implementation of multiple Coulomb electromagnetic scattering and Vavilov or Gaussian energy straggling distributions.
- Stopping power values are calculated from the Bethe-Bloch equation (introduced in 2.1.1), where the mean I-value is calculated with the Bragg additivity rule (eq. 2.9). The density correction is calculated according to [Sternheimer and Peierls, 1971] and the shell correction is omitted. The effective charge is calculated according to [Hubert et al., 1989] and by the Lindhard-Scharff formula to correct for electron capture for energies below 0.3 MeV/u [Geithner, 2006].
- The particle transport cut-off energy is decreased to 0.25 keV/u, to deal with ranges of particles that correspond to dosimetry chamber dimensions.
- Additionally to the stopping power calculations, the ICRU49 and 73 data tables are implemented as external files. They contain stopping power values as a function of energy for protons up to argon.

Inelastic nuclear interactions are modeled by the Multi Stage Dynamical Model (MSDM) which was developed at the Institute for Nuclear Research of the Russian

Academy of Science (INR RAS, Moscow) and in the Joint Institute for Nuclear Research (JINR, Dubna). As a default model it considers:

- a fast cascade stage, which brings the interaction between the projectile and target to a sequence of binary collisions between nuclear constituents and/or produced hadrons [Toneev and Gudima, 1983]
- pre-equilibrium emission, in which nuclei can emit particles during thermalization [Gudima et al., 1983]
- equilibrium de-excitation of residual nuclei with Fermi break up of light nuclei, evaporation/fission competition and Multi-fragmentation of highly excited nuclei [Botvina et al., 1987]

Further improvements in SHIELD-HIT are implemented in this work released in the versions SHIELD-HIT07 and SHIELD-HIT08 from years 2007 and 2008, respectively.

Version SHIELD-HIT07

SHIELD-HIT07 is used for all calculations on dosimetry in this work. Prominent changes introduced during this work are:

- 1.) To improve the resolution of the calculations, the number of value scoring arrays is increased from 500 to 3000. E.g. for a 300 mm large volume with a resolution of 0.1 mm SHIELD-HIT has to calculate and store the values within 3000 volumes, which requires an array of the same size.
- 2.) The total number of elements describing a medium is increased from 9 to 13. To describe a compound medium like water, SHIELD-HIT needs information about the elements of the compound and their weight proportions. For water only two elements are defined (H and O), but for example for muscle 13 elements are needed.
- 3.) Moreover, the code is converted to run on a Linux based computer cluster to increase the number of calculations.
- 4.) Molière's multiple scattering theory is implemented according to [CERN, 1994] and is successfully tested in [Hollmark et al., 2008].

Version SHIELD-HIT08

Major improvements in the main code and several subprograms are implemented in the recent version SHIELD-HIT08 in this work:

- 1.) The main improvement is the adjustment of PARLEV(39), (34) and (33) toward measured depth-dose curves, Bragg peak heights and differential cross sections for proton up to carbon particles.
- 2.) Implementation of a model to simulate charge. This is used to test the nuclear interaction model and is described in 2.9.2.
- 3.) Stopping power values from the ATIMA code can be used from external files as for the ICRU data [ATIMA, 2007].
- 4.) Improvement of elastic nucleon-nucleon scattering in the intra nuclear cascade and the p/n elastic scattering on H in a medium.

The structure of SHIELD-HIT

The executable file requires three main input files. File FOR022 contains information about the target media (mass density, compound elements and their corresponding partial concentrations, partial densities and their I-values).

FOR023 contains the initial beam setup (particle type, energy, energy spread and lateral beam spread). Furthermore, the user can chose between Vavilov and Gaussian energy straggling, Molière and Gaussian scattering and the absence of nuclear reactions for special studies.

PASIN defines the geometry according to the concept of combinatorial geometry (3D geometrical objects linked to bodies to describe the system). SHIELD-HIT can use external ICRU stopping power data but requires an external file containing this data on a default energy grid.

A sketch of a 3D geometry to score depth-dose curves is shown in 2D in Figure 2.4. Usually a cylindrical volume separated into slabs (or bins) of thickness Δh is used. The total length of the cylinder depends on the range of the particle and is typically 300 mm. The slabs define the spatial resolution of the calculations. The energy loss is simulated within one slab and the deposited energy is integrated over the whole slab volume $\pi r^2 \Delta h$.

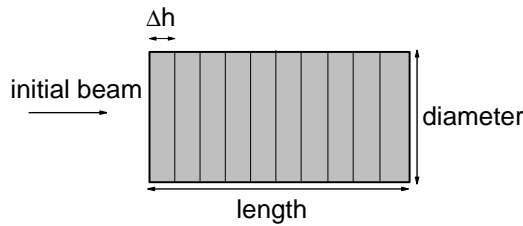


Figure 2.4: 2D view of the cylindrical scoring volume to simulate a depth dependent dose distribution in SHIELD-HIT.

The setup of SHIELD-HIT related to GSI parameters

Besides the initial beam energy and the particle type, several parameters in SHIELD-HIT influence the results. The parameters which are discussed to adjust the measurements during this work are the following:

- $\frac{\Delta E}{E}$; the initial energy spread of the beam
- $\sigma_x = \sigma_y$; Gaussian spread of the beam in x and y direction
- I_x ; the mean excitation potential of the medium x
- PARLEV(39), PARLEV(34) and PARLEV(33); 3 of 40 free parameters in the physical models in SHIELD-HIT. They are adjusted to achieve agreement with experimental data and are 1.0 as default.

$\Delta E/E$, σ_x and σ_y are defined by the properties of the experimental beam. The usual value of $\Delta E/E$ at GSI is 0.34 % and 0.16 % for protons and carbon ions, respectively. σ_x and σ_y (FWHM = $\sigma \cdot 2.35$) are 2.13 mm at the GSI system. For the mean excitation potential for water a value of 80.8 eV is used, because this is the recently published value in [Paul et al., 2007]. This value is chosen to best represent measured depth-dose curves in water with SHIELD-HIT and mainly influences the range of the beam.

Within the beam modeling in SHIELD-HIT there are several free parameters, which are named PARLEV(XX), ranging from 01 to 40. PARLEV(39) was briefly discussed in [Geithner, 2006] and is reviewed again in 2.9.1 in this work. PARLEV(39) re-normalizes the cross section of inelastic interactions of ions and influences the attenuation of the projectile and the number of produced fragments. The height of the Bragg peak is decreased with a value of 0.8, which is determined to best represent experimental data. Therefore, the default value of 1.0 is set to 0.8 for the calculations on treatment planning with carbon ion beams.

Two other free parameters are determined to considerably influence the inelastic cross sections. PARLEV(34) relates to the Fermi-Break-up. It determines the phase space available for a break-up channel, and in this way it influences its probability. A decrease of PARLEV(33) increases the Coulomb barriers of the decay channels and suppresses them. The default values of 1.0 for PARLEV(34) and (33) are discussed in 2.9.3 to improve the SHIELD-HIT results toward measurements.

2.2.3 The Monte Carlo code Geant4

The Geant4 MC code (**G**eometry and **T**racking) is a result of a collaboration of many research facilities headed by CERN (European Organization for Nuclear Research) to simulate high energy physics [Geant4, 1999]. It was completely redesigned and rewritten based on the Geant3 calculation package using C++ and the object-oriented paradigm [Brun et al., 1987]. EM and nuclear models, addressing different types of interactions of particles with matter, are chosen through the *PhysicsList*.

The calculations for protons are done with Geant4.8.1 (courtesy in calculations by Harald Paganetti, MGH Boston). The physics settings according to [Jarlskog and Paganetti, 2008a] are: the standard electromagnetic model, the low-energy parametrized elastic model and the binary cascade model for inelastic scattering of protons and heavier ions. The stopping power is calculated with the Bethe-Bloch equation.

Geant4.9.2 is used to simulate dose for carbon ions (courtesy in calculations by Basit Athar, MGH Boston). Geant4.9.2 contains the Monte Carlo model for Therapy (MCHIT) [Pshenichnov et al., 2005]. It considers two kinds of interactions, the elastic scattering of projectile hadrons or nuclei on target nuclei and nuclear inelastic reactions induced by fast hadrons and nuclei.

2.2.4 The Monte Carlo code FLUKA

FLUKA (**FL**Uktuierende **KA**skade) is a MC code developed in a collaboration between the Italian National Institute for Nuclear Physics (INFN) and CERN, in the programming language Fortran77 [Battistoni et al., 2007], and is successfully applied in hadron therapy [Sommerer et al., 2006]. In FLUKA2008.3.b (courtesy in calculations by Rochus Herrmann, Aarhus University) the energy loss is calculated by Bethe-Bloch including density and shell corrections. The elastic scattering is simulated by Molière's theory of

multiple Coulomb scattering. The physical models for nuclear-nuclear interaction modeling as external event generators are 'HADROTHE' and 'DPMJET'. The geometry is very similar to that in SHIELD-HIT and differs only in the structure. The code is not accessible but can be addressed by 'User Routines' connected to the executable file.

2.3 Basics of Dosimetry

To investigate radiation effects and measure deposited energy or dose by directly or indirectly ionizing radiation in a medium at a certain point, the concept of dosimetry was established. A number of units and quantities have been defined to characterize the dose from a particle beam and are introduced in this chapter. The beam characterization is needed in radiation therapy as a measure of the effect of the radiation to the tissue. For standardized determinations, water is used as a reference medium.

2.3.1 The Absorbed Dose

The absorbed dose D is a non-stochastic quantity. It is expressed by the mean energy imparted $\bar{\epsilon}$ by ionizing radiation to mass m in an infinite volume by:

$$D = \frac{d\bar{\epsilon}}{dm} \quad (2.12)$$

The energy imparted is the difference of energy entering the volume of interest (deposited energy) and the energy leaving the volume together with the energy conversion within the volume.

An approximation of the absorbed dose from physical quantities is the product of the mass stopping power (S/ρ) and particle fluence Φ over the whole energy spectrum E , primary and secondary particles i and target medium m . This approximation is valid as long as the primary particle leaves the finite volume and the dose is absorbed locally.

$$D_m = \sum_i \int dE \cdot (S(E)/\rho)_{m,E,i} \cdot \Phi_{m,E,i} \quad (2.13)$$

The absorbed dose is the standard parameter used in radiotherapy and has to be simulated carefully to avoid over- and underestimations in the treatment. An under dosage in the tumor volume can lead to a recurrence of the tumor due to surviving tumor cells. An over dosage in the healthy tissue can damage the cells and cause side effects.

The energy deposition in a medium of mass density ρ is given in MeV/cm³. The unit of absorbed dose is Joule/Kilogram or Gray (Gy). In this work the deposited energy is always given in MeV/cm³, which is equivalent to MeV/g for water, because the density of water is 1 g/cm³ in the equivalent calculations.

$$\frac{1 \text{ MeV}}{\rho \text{ cm}^3} \hat{=} \frac{\text{MeV}}{g} = 1.602 \cdot 10^{-10} \frac{J}{kg} = 1.602 \cdot 10^{-10} \text{ Gy} \quad (2.14)$$

2.3.2 Parameters of a Depth-Dose Curve

The depth-dose curve, or Bragg curve, describes the dose distribution of radiation along the central beam path z . It is subdivided into a plateau, peak and tail region. The parameters which characterize a depth-dose curve are shown in Figure 2.5, where z is the depth. They are used in 3.7 to study the shape of the Bragg curve in various media. They are:

- The Bragg peak position. It is the position of the maximum dose (peak dose) in a medium.
- Full Width at Half Maximum of the Bragg curve, $FWHM_{BC}$. It describes the width of the Bragg peak at the 50 % dose.

$$FWHM_{BC} = z_{max}(D_{50\%}) - z_{min}(D_{50\%}) \quad (2.15)$$

- Distal Edge Width, DEW. It describes the width of the distal edge between the 80 % and 20 % dose value of the dose curve according to:

$$DEW = z(D_{80\%}) - z(D_{20\%}) \quad (2.16)$$

- Peak-Entrance-Dose, PED. This is the ratio of the peak dose to the plateau dose. Here, the plateau dose is obtained as a mean within the first 20 mm of the Bragg curve.

$$PED = \frac{D_{peak}}{D_{entrance}} \quad (2.17)$$

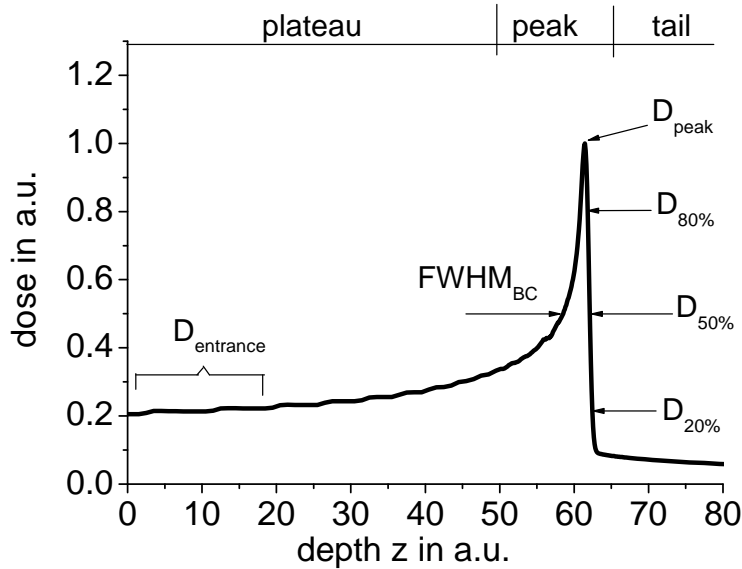


Figure 2.5: Definition of parameters describing any depth-dose curve of a particle beam.

The usual term of FWHM is used to describe the lateral spread of the beam in x and y . Therefore, the FWHM of the Bragg curve is defined as $FWHM_{BC}$. Positions upstream

of the Bragg peak (or closed to the beam entrance) are called proximal and downstream distal of the Bragg peak.

2.3.3 Ionization Chamber Dosimetry

The absorbed dose can be measured with various detectors such as: calorimeters, radiation counters, semiconductor and scintillation detectors, thermoluminescence and chemical detectors, film dosimeters, and ionization chambers. Since only ionization chambers are used in this work, it is focused on their properties.

Ionization chambers are devices to measure charge in a gas filled volume. The basic layout of an ionization chamber is shown in Figure 2.6. The incoming radiation ionizes

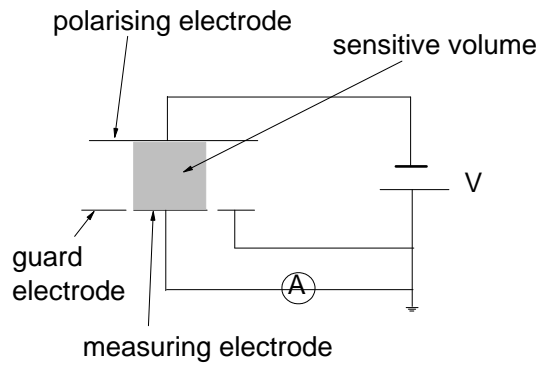


Figure 2.6: Basic layout of an ionization chamber.

the air filled cavity of the chamber shown in grey. Electrodes measure the charge, which is proportional to the absorbed dose from the incoming beam. From the chamber signal M and the mass of the air cavity m , the absorbed dose in water D_w is calculated by:

$$D_w = \frac{M}{m} \left(\frac{W_{air}}{e} \right) S_{w/air} \prod p_i, \quad (2.18)$$

where W_{air}/e is the mean energy required to produce an electron-ion pair in air, $S_{w/air}$ the water-to-air stopping power ratio and p_i are chamber specific correction factors. The $S_{w/air}$ is a conversion factor for absorbed dose measured in air, to dose to water and is studied in 2.3.3. The factor p is a product of various factors correcting for changes in the radiation field when using an air filled ionization chamber in water. These are effects of the chamber wall, the air cavity and the central electrode.

When the ionization chamber is used under conditions different from the calibration conditions, the measured signal M has to be corrected for, e.g. the chamber polarity and saturation effects (k_i). The dose to water in a beam quality Q , different from ^{60}Co , is calculated by:

$$D_w = N_w \cdot M \cdot k_Q \prod k_i, \quad (2.19)$$

where N_w is a chamber specific calibration factor obtained from the standard laboratory. The k_i account for the correction in temperature and pressure ($k_{T,P}$), the polarity (k_{pol}), the saturation (k_S), the displacement for cylindrical chambers (k_r). The factor k_Q transfers dose from an air filled ionization chamber calibrated in ^{60}Co (corresponds to

reference beam quality Q_0) to any radiation field (e.g. carbon) with quality Q according to:

$$k_Q = \frac{\left(S_{\frac{w}{air}}\right)_Q \left(\frac{W_{air}}{e}\right)_Q p_Q}{\left(S_{\frac{w}{air}}\right)_{Q_0} \left(\frac{W_{air}}{e}\right)_{Q_0} p_{Q_0}}, \quad (2.20)$$

where, $\left(\frac{W_{air}}{e}\right)_Q$ is the mean energy required to produce an electron-ion pair in air, p_Q a chamber specific correction factor and $\left(S_{\frac{w}{air}}\right)_Q$ the water-to-air stopping power ratio for beam quality Q .

The Stopping Power Ratio

The water-to-air stopping power ratio, $S_{w/air}$, defines the ratio to convert dose measured within the sensitive air volume of an ionization chamber to dose to water. It is derived by calculating the dose ratio via track-length fluence $\phi_{E,i,w}$ for water w from particle i with energy E and mass stopping power $S_i(E)/\rho$ for water and air by:

$$S_{w/air} = \frac{\sum_i \int_{E_i > \Delta}^{E_{max}} \phi_{E,i,w} (S_i(E)/\rho)_w}{\sum_i \int_{E_i > \Delta}^{E_{max}} \phi_{E,i,w} (S_i(E)/\rho)_{air}} \quad (2.21)$$

In theory Δ is zero, but in SHIELD-HIT the cut-off specific energy is set to 25 keV/u. Due to lacking knowledge of energy dependent stopping power and fluence data, the $S_{w/air}$ is approximated as a constant factor of 1.13 in IAEA TRS-398 [TRS-398, 2000]. Another approximation for the stopping power ratio of a monoenergetic beam is given by the ratio of stopping powers of the primary ion. From equation 2.5, it can be expressed by the ionization potential I_w for water and I_{air} for air, as well as the classical electron rest mass m and the speed of the incoming particle v according to [Paul et al., 2007] by equation:

$$\frac{S(E)/\rho)_w}{S(E)/\rho)_{air}} \approx \frac{0.5551 \ln(2mv^2/I_w)}{0.4999 \ln(2mv^2/I_{air})} \quad (2.22)$$

The Plane-Parallel Ionization Chamber

A plane-parallel ionization chamber is a special type of ionization chamber to measure dose in particle therapy. It consists of two plane walls. One operates as an entry window and polarizing electrode and the other as the back wall and collecting electrode. The collecting electrode and the guard-ring system of the back wall are coated with graphite and are embedded within plastic or another non-conducting material. Figure 2.7, [Podgorsak, 2003], shows the schematic of a plane-parallel ionization chamber with the polarizing electrode (1); the measuring electrode (2); and the guard ring (3). Here, (a) is the height of the air cavity; (d) the diameter of the polarizing electrode; (m) the diameter of the collecting electrode and (g) the width of the guard ring.

That concept of ionization chambers is used in the Bragg Peak-, Roos- and Advanced Roos chamber from PTW (Physikalisch-Technische Werkstätten, Freiburg, Germany). In section 2.5 they are used to measure depth-doses curves downstream of media samples. As no absolute dose is measured in this work, an introduction in correction factors is not necessary.

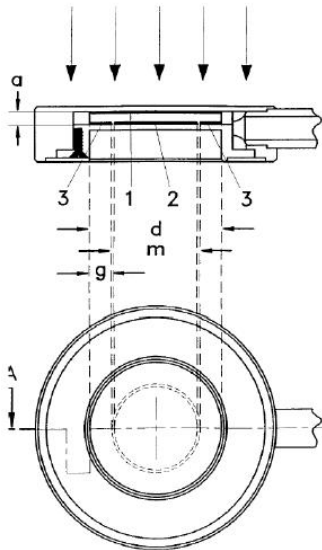


Figure 2.7: Schematic of a plane-parallel ionization chamber which integrates charge over the sensitive volume defined by the size of the measuring electrode.

2.4 Basics of Treatment Planning

The aim in radiation therapy is to deliver a conformal high dose to the tumor while limit the dose in healthy tissue. In the treatment planning system (TPS) dose distributions in the patients are calculated based on CT images. Pencil beam algorithms are commonly used clinically which, however, calculate only in water and therefore approximate the dose distributions.

2.4.1 Treatment Delivery Systems

There are two general methods in hadron therapy to deliver homogeneous dose to a tumor volume, passive scattering and active scanning. For both, Bragg peaks are superimposed to form a Spread Out Bragg Peak (SOBP) shown in Figure 2.8. The maximum and minimum energy are defined by the most distal and most proximal slice to the beam exit window.

In passive scattering a modulation wheel is used to form SOBP's in the tumor volume. The design of wheel segments is based upon the width and position of the target volume (tumor).

A better approach to benefit from the sharp dose deposition from ions in the target is the raster scanning technique (Figure 2.9) [Krämer et al., 2000]. The dose is applied by single pencil beams and is adapted to the shape of the tumor by orthogonal magnets in lateral direction and by the primary beam energy in depth. As shown in Figure 2.8, the SOBP is formed by varying the range of the beam via the primary energy from the synchrotron. Therefore, the tumor is divided into slices of constant depth to be scanned lateral with a constant energy. As reported in [Krämer et al., 2000], the irradiation of an average target of 60 mm diameter (about 110 cm^3) with scanner spots of 2 mm spacing and range steps of 2 mm, requires about 14000 single beam positions.

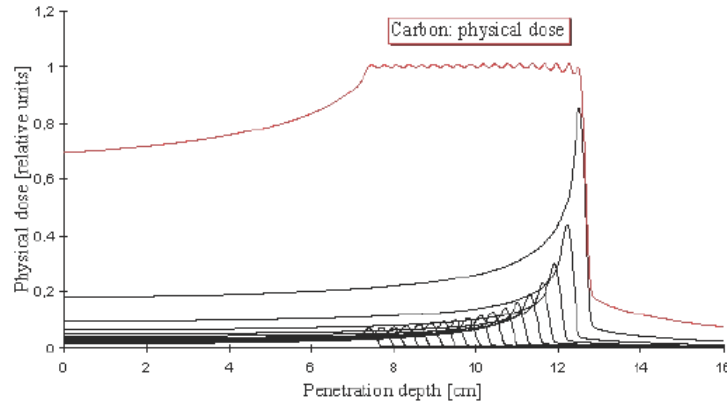


Figure 2.8: The SOBP as a superposition of weighted single Bragg peaks. The modulation width is 60 mm at 70 mm penetration depth.

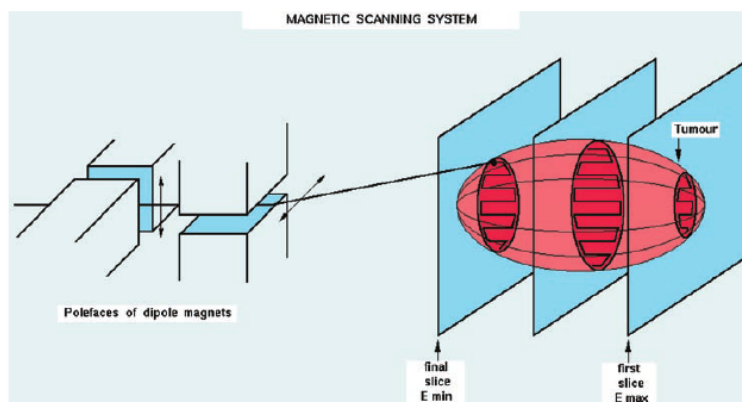


Figure 2.9: Particle beam scanning as used at GSI, Darmstadt and at HIT, Heidelberg.

2.4.2 Heavy Ion Radiotherapy at GSI

The GSI facility combines active scanning and energy variation and provides a fully three dimensional intensity modulated radiation field with high spatial resolution.

The SOBP is calculated from a list of 253 energies from 80 MeV/u to 430 MeV/u corresponding to a range between 20 mm and 330 mm in water. The energy can be switched in about 5 s. The size of the beam spot depends on the size of the target volume and the energy of the primary beam. Typical spot sizes are 5 mm FWHM and are Gaussian shaped. During treatment, the applied dose is monitored with ionization chambers.

To compensate the effect of the very narrow Bragg peak of carbon ions, a ripple filter in front of the beam exit window is used to broaden the single Bragg peaks and flatten the SOBP plateau [Weber and Kraft, 1999].

Requirements for Treatment Planning

The initial procedure for treatment planning with heavy ions is the same as in conventional radiotherapy with photons. First, a digital model of the irradiated region is obtained from computer tomography (CT) images. The CT data are needed for dose calculation and optimization.

The patient contour, the tumor volume and the critical structures are delineated on the CT data within the planning system. According to the knowledge from photon radiotherapy, dose is prescribed to the tumor, whereas the dose for critical structures is restricted to a given maximum dose.

For treatment planning at GSI, the software TRiP (TReatment planning for Particles, current TRiP98) was developed [Krämer et al., 2000] and [Krämer and Scholz, 2001]. TRiP includes Monte Carlo generated data based on projectile fragmentation and particle scattering for carbon ion beams, and accounts for radiobiological effects in the tissue.

TRiP calculates optimized biological dose from the physical dose to the target volume. An overview of individual steps of treatment planning at GSI is shown in Figure 2.10 [Kraft, 2007] and is discussed in more detail in [Krämer and Scholz, 2001] and [Krämer et al., 2000].

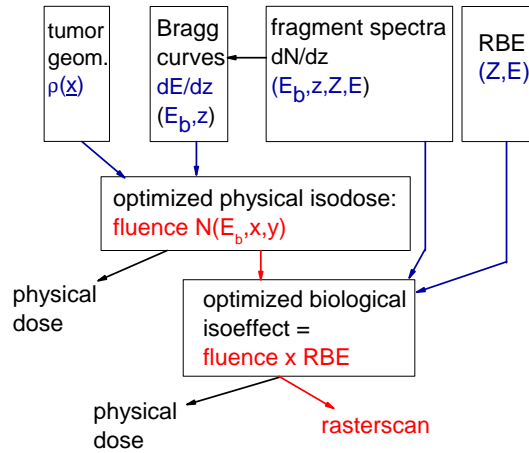


Figure 2.10: Scheme of the treatment planning process at GSI, Darmstadt. It consists of three main parts. First the physical dose is optimized to the target volume, second the RBE is calculated and the biological dose is optimized and finally, the control files for the scanner system are calculated.

The radiobiological effectiveness (RBE) describes the response of the tissue to the radiation and depends on, e.g. particle charge, energy, absorbed dose and cell type. It is defined as the ratio of the dose from photons to dose from ions required to achieve the same endpoint and is a measure for the ionization density of the particle beam. An endpoint is, e.g. same local control rate or cell survival rate. The RBE for carbon ions increases toward the end of the particle range (see Figure 2.11 for an SOBP), whereas for protons the clinical RBE is constant at 1.1 over the whole range.

$$RBE = \frac{D_{\text{photon}}}{D_{\text{ion}}} \Bigg|_{\text{endpoint}} \quad (2.23)$$

In carbon ion therapy, the SOBP is calculated to have a homogeneous biological effective dose in the tumor. Since the RBE for carbon ions increases toward the distal end of the tumor, the physical dose (dose without RBE) shows a decrease toward higher depth as shown in Figure 2.11. To distinguish physical and biological doses, the unit of "Gray Equivalent" GyE is used to quantify the biological dose.

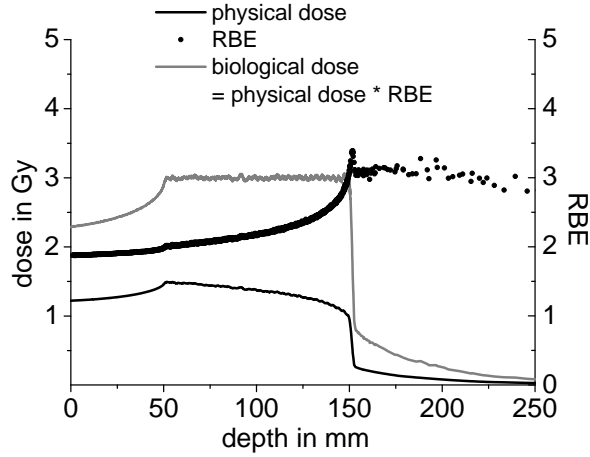


Figure 2.11: TRiP98 calculated physical and biological dose distributions (left y-axes) and RBE (right y-axes) for a carbon ion SOBP at 50 mm and 100 mm modulation width in water. The biological dose is the product of the RBE and the physical dose.

2.4.3 The Beam Model at GSI

The beam model for carbon ions used at GSI in [Krämer and Scholz, 2001] is based on the pencil beam model where the dose is calculated by a superposition of Gaussian functions [Soukup et al., 2005]. The dose generated by a single beam of energy E_{beam} and number of particles N in water, centered at (x_0, y_0) , is described by:

$$D(E_{beam}, \mathbf{x}) = (1.6 \cdot 10^{-8}) d(E_{beam}, z) \frac{N}{2\pi\sigma^2} \exp^{-\frac{r^2}{2\sigma^2}}, \quad (2.24)$$

where r and σ are the distance from the beam center and the width of the Gaussian beam profile, respectively. N is the total number of particles. The energy loss distribution, $d(E_{beam}, z)$, characterizes the energy loss of the heavy ion beam of primary energy E_{beam} in water or water equivalent medium against depth z .

A numerical program which is restricted to a one dimensional description of the primary beam and the secondary particles was developed. Within this model the absorber is divided into small slices depending on the expected Bragg peak position. The energy spectra along depth is obtained from cross sections for the creation of fragments within these slices ([Schümerer et al., 1990] and [Schardt et al., 1996]). Simultaneously, the spectrum is transformed by attenuation from total reaction cross sections, energy loss straggling and energy loss. The final depth-dose distribution is described by:

$$d(E_{beam}, z) = \sum_T \int_E dE \frac{dN}{dE}(E_{beam}, z, T, E) \frac{dE}{\rho dx}(T, E), \quad (2.25)$$

where the dependence on the fragment species T and energy E is described by (T, E) and ρ is the mass density of the medium.

Recently, depth-dose distributions are derived from MC calculations for energies from 50 to 500 MeV/u in steps of 10 MeV/u in water. They are stored together with the local energy spectrum in a data table. Intermediate data are interpolated.

2.4.4 The Water Equivalent Path Length

To convert the range of ion beams in human tissue into the corresponding range in water, the water equivalent path length (WEPL) was introduced [Rietzel et al., 2007]. This is necessary, because a scaling by the electron density of the medium from CT-number is not sufficient.

The main idea is that the mass stopping powers of different media are very similar to each other. The WEPL scales the range r (in mm) of a particle beam traveling through a medium, m , of slab thickness d (in mm), into the equivalent range in water, w , according to:

$$\text{WEPL} = \frac{r_w - r_m}{d} + 1 \quad (2.26)$$

The range of the particle beam is obtained at the position of 80 % dose in the distal fall-off being least dependent on initial beam parameters [Bichsel et al., 2000]. In Figure 2.12 the WEPL is shown as the shift of two Bragg curves. Here, the Bragg curve in water (blue) is shifted toward shallower depth with some denser medium of thickness d in the beam path (black).

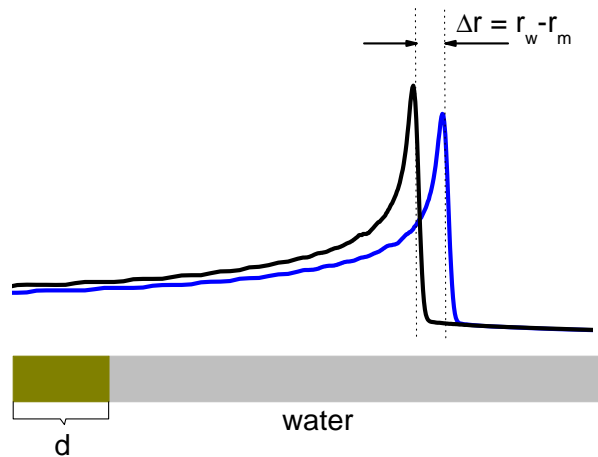


Figure 2.12: The concept of WEPL for Bragg curves of the same energy. The curve obtained in water (blue) and a more dense medium with dimension d (black) are shifted by the amount of the WEPL.

The water equivalent range, $\text{WEPL} \cdot R_m$, of particles crossing the slab is described by the ratio of stopping power S in a medium to that in water, since S is almost constant within the slab. The range in a medium R_m is calculated corresponding to:

$$R_m = \int S_m^{-1} dE = \int (\text{WEPL})^{-1} \cdot S_w^{-1} dE \quad (2.27)$$

The WEPL of various media together with the according CT-numbers are used in the TPS in a look up table. The CT-number from a CT scan and the WEPL from range measurements for same media are obtained and tabulated for a certain set of energies and media. The correlation of CT-number and the WEPL is shown in Figure

2.13 [Krämer et al., 2000]. The Hounsfield Unit of a CT voxel is related to a WEPL. Applying the WEPL on the voxel dimensions they are replaced by their corresponding water equivalent dimensions and the dose is re-normalized to the new voxel size.

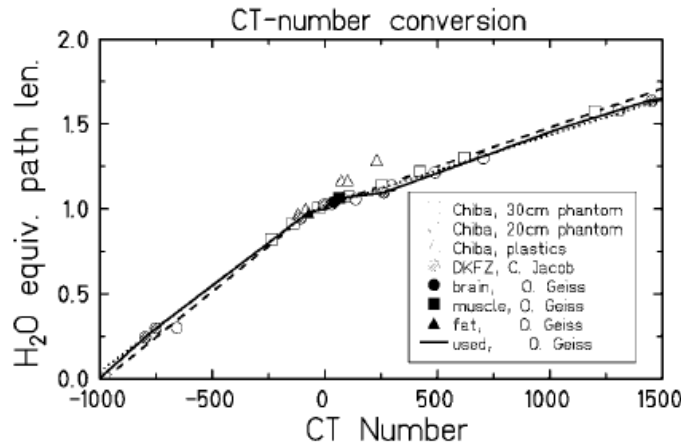


Figure 2.13: Correlation between CT Hounsfield units and the WEPL.

2.5 Performed Measurements

In order to obtain data to benchmark the MC due to the accuracy of calculating depth-dose curves, measurements at GSI were performed. During these experiments, depth-dose curves downstream of adipose, cortical bone tissue substitutes and a titanium sample, shown in Figure 2.15 (a) are obtained in water.

From measurements with and without a media sample, the accuracy of the I-value given in ICRU37 for the substitutes and ICRU49 for titanium is determined. The influence of the dimension of the substitutes on the WEPL is studied in a comparison to similar measurements with a 'PeakFinder' (PTW) at HIT Heidelberg with samples of 20 mm length by [Ackermann et al., 2008].

The 'PeakFinder' is a water column which was developed for particle beams to determine the Bragg peak position in water with a resolution of 0.01 mm. In contrast to the measurements at GSI where the samples are placed in the water phantom, the samples are placed in front of the water column at HIT, because it is enclosed.

The measurement setup at GSI is shown in Figure 2.14. The adipose and cortical bone media samples are taken from the Gammex 467 phantom (Gammex 467, GAMMEX rmi, Middleton, WI, USA). The tissue equivalent inserts in this phantom are known to best reflect the tissue composition in the human body.

Adipose is chosen having a lower density than water. Cortical bone and titanium (block from the laboratory) are used, since their density is much larger than for water and considerable changes in the depth-dose curves are expected. Furthermore, titanium is often used for implants.

Used software and measurement devices from PTW are: the software MEPHYSTOMc², the MP3 water phantom with Tandem and Control Unit, the Bragg peak chamber T34070, Figure 2.15 (b), the Advanced Roos chamber TM34073 and the Roos chamber M34001. All chambers are plane-parallel ionization chambers and differ mainly in size, see Table 2.3. Since they integrate over the sensitive volume, measurements with

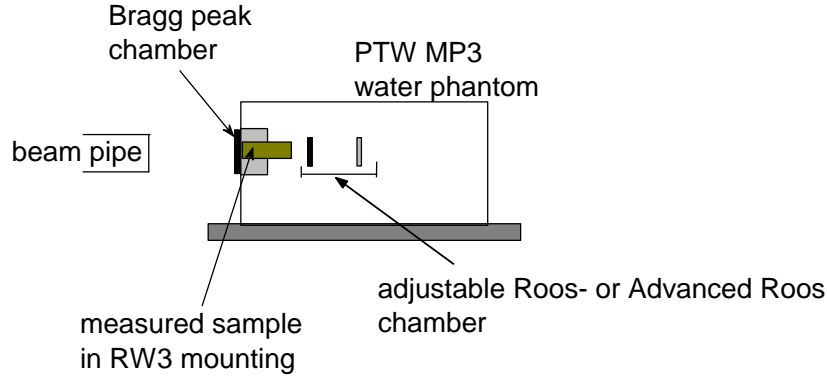


Figure 2.14: Setup for ionization chamber based depth-dose curve measurements. The beam comes through the beam exit window, passes the Bragg peak chamber, the MP3 wall, 10 mm of water, the substitute and the Roos- or Advanced Roos chamber which measure the dose.

different chamber diameters give an estimation on the influence of lateral scattering on the Bragg curve.

Table 2.3: Main characteristics of the ionization chambers which are used for the measurements.

chamber type	sensitive volume in cm^3	sensitive electrode diameter in mm	water equivalent window thickness in mm
Bragg Peak	10.46	81.6	4.0
Advanced Roos	2.48	39.6	1.3
Roos	0.35	15.0	1.3

The measurement was arranged as follows. To ensure that the beam is covered by the chambers, the primary carbon ion beam is adjusted to the isocenter and the MP3 water phantom along the laser system. The Bragg peak chamber was fixed at the entrance window of the water phantom and was used as a reference chamber. The Gammex phantom substitutes were mounted in an RW3-disk with a radius of 80 mm and a thickness of 20 mm and in the water phantom. For measurements with titanium, the plate was fixed in front of that disk. Depth-dose curves for 299.9 MeV/u carbon ion beams with a FWHM of 4.3 mm were measured for the following four setups with the Advanced Roos- and the Roos chamber:

1. depth-dose curve in water (without sample, but sample mount is present)
2. depth-dose curve in water downstream of a cylindrical adipose tissue substitute from the Gammex 467 phantom with dimensions $r=14.3$ mm and $h=56.2$ mm
3. depth-dose curve in water downstream of a cylindrical cortical bone tissue substitute from the Gammex 467 phantom with dimensions $r=14.3$ mm and $h=56.2$ mm

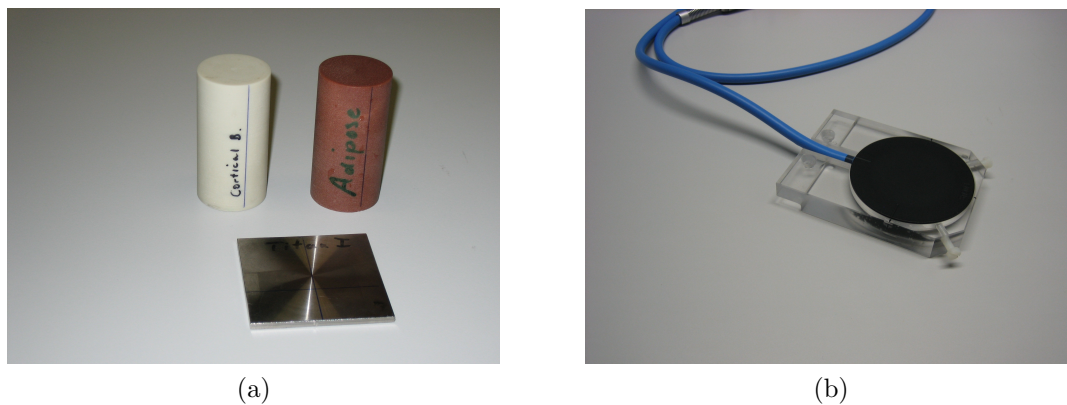


Figure 2.15: The used medium samples (a) and the Bragg Peak chamber within a holder to fix it in front of the water phantom in (b). The Roos- and Advanced Roos chamber look very similar to the Bragg peak chamber and differ only in their size.

4. depth-dose curve in water downstream of a titanium plate of 50.3 mm x 50.0 mm x 2.83 mm

Measurements "without sample" means, that nothing was mounted in front nor in the disk.

The Advanced Roos- and the Roos chamber were controlled via tbaScan from the MEPHYSTOMc² software in spill mode. Spill mode synchronizes the measurement time with the spill time of the beam, which reduces the noise signal during the measurement. The resolution in the Bragg peak region was 0.1 mm. The precision of the position from the PTW MP3 system is ± 0.01 mm (manufacturer specification).

2.6 Monte Carlo Simulations for Dosimetry

In this section the default value of 1.0 is used for PARLEV(39), because at the time of the analysis the impact of this value was not sufficiently analyzed. However, an influence on the depth-dose curve is only observed in the peak height and does not considerably influence the results shown here.

2.6.1 Determination of the I-value for Water

Due to the controversy of I-values for water discussed in 2.1.2 and [Henkner et al., 2009a] (appendix G on page XXV), the calculations in [Geithner et al., 2006] are revised. Furthermore, simulated depth-dose curves are compared to new, not yet fully published, experimental data available from [Schardt et al., 2008] on the absolute Bragg peak positions for lithium, carbon and oxygen ion beams of several energies in water. Depth-dose distributions calculated with SHIELD-HIT are used to derive I-values from this data.

Therefore, depth-dose distributions with I-values from 77 eV up to 86 eV are simulated with SHIELD-HIT for bins of 1 mm. From these curves, the simulated Bragg peak positions ($BP_{\text{simulated}}$) are obtained with a polynomial fit in the peak region for each Bragg curve. Afterwards, the deviation from the experimental position (BP_{measured}) is derived. The I-value which best represents the measured peak position ($BP_{\text{measured}} - BP_{\text{simulated}} = 0$) is determined by interpolation.

The mean I-value for a compound is calculated from the elemental I-values with the Bragg rule (eq. 2.9) in SHIELD-HIT. It is determined by varying the elemental I-values taken from Table 2.1 in ICRU49 (appendix F on page XI). SHIELD-HIT uses the mean I-value for stopping power and depth-dose curve calculations.

2.6.2 The I-Value for Compounds

The mean I-value for compounds together with their compositions are tabulated in [ICRU37, 1984]. ICRU37 also provides the uncertainty ΔI of the I-values, which can be up to $\pm 15\%$ shown for selected media in Table 2.4. The mean I and ΔI for elements, like titanium, are given in ICRU49. For these media the resulting uncertainty in the range of a 270 MeV/u carbon ion beam is investigated.

Table 2.4: Maximum uncertainty of the mean I-value as given in ICRU49 and 37.

medium	mean I	ΔI in eV acc. to ICRU49	ΔI in % acc. to ICRU37
water	75 eV	3	
titanium	233 eV	5	
adipose	63.2 eV		10
cortical bone	106.4 eV		10
compact bone	91.9 eV		10
muscle striated	74.7 eV		5
muscle skeletal	75.3 eV		5

2.6.3 The Water-to-Air Stopping Power Ratio

As described in [Henkner et al., 2009a] (appendix G on page XXV), the I-value has an effect on the water-to-air stopping power ratio, $S_{w/air}$, for primary carbon ion beams. Hence, the effect of I on the $S_{w/air}$ is determined for proton beams as well.

The water-to-air stopping power ratio for protons is simulated in three steps. First, the stopping power for hydrogen particles from incident proton beams in water and air is simulated. Second, the dose is simulated via the track-length fluence in water. Afterwards, the water-to-air stopping power ratio is determined according to eq. 2.21. Table 2.5 shows four sets of I-values which were used for stopping power ratio calculations of monoenergetic proton pencil beams. In contrast to [Henkner et al., 2009a] (appendix G on page XXV), the value from ICRU73 is not used, because this report is valid only for ions of $Z > 2$.

2.6.4 Required Size of a Water Tank for Dosimetry

The quality assurance (QA) plays a major role in radiation therapy. This ensures that the treatment system applies the calculated dose to the patient. Therefore, weekly tests are performed to measure the absolute value of the dose. This is usually done with an ionization chamber in a water phantom. In IAEA TRS-398 a reference field of $100 \times 100 \text{ mm}^2$ and a water phantom of at least 50 mm larger than the field size is

Table 2.5: An overview of the combination of I-values for water and air, which are used for stopping power ratio calculations. The set numbers are taken from Table II on page 1232 in [Henkner et al., 2009a] for comparison.

set	I_{air}	I_w	Source for I_{air}	Source for I_w
3	tabulated data	tabulated data	ICRU49	ICRU49
4	85.7 eV	75 eV	ICRU49	ICRU49
5	85.7 eV	80.8 eV	ICRU49	Paul et al.
6	88.8 eV	80.8 eV	Paul et al.	Paul et al.

recommended for photon beam QA. Usually a water tank side length of 300 mm is used. The field size and size of the water tank ensures secondary particle equilibrium during measurements with photons.

Since there are no recommendations for particles and the lateral spread is smaller than for photons, the required lateral dimension of a water tank in particle therapy is estimated with SHIELD-HIT. The dose for a 100 x 100 mm² particle field of 180 MeV and 250 MeV protons, and 350 MeV/u and 450 MeV/u carbon ions is simulated at 100, 200 and 300 mm depths for volumes of 10 x 10 x 10 mm³. These volumes should represent ionization chambers which are used in the QA process within a water tank.

The lateral length of the water tank varies between 120 and 500 mm while the depth is fixed at 500 mm. The position of the 10 x 10 x 10 mm³ scoring volumes relative to the depth-dose curves related to 180 MeV and 250 MeV protons and 350 MeV/u and 450 MeV/u carbon ions are shown in Figure 2.16.

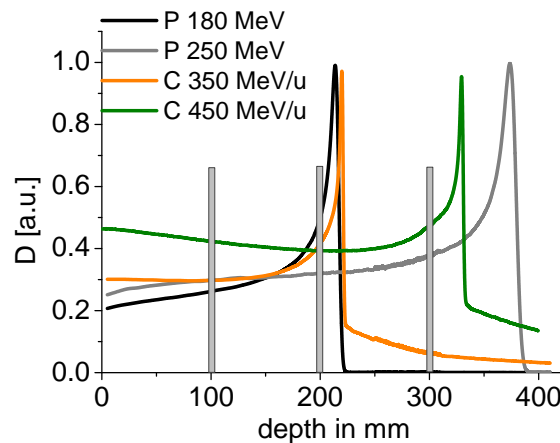


Figure 2.16: Relative depth-dose curves of 180 MeV and 250 MeV protons and 350 MeV/u and 450 MeV/u carbon ions. The positions of the dose scoring volumes are shown by the grey rectangles.

2.7 Monte Carlo Simulations for Treatment Planning

2.7.1 Benchmark on the Measurements at GSI

The measurements at GSI described in 2.5 are used to benchmark the prediction of the MC and to estimate the accuracy of the I-values given in ICRU49. Therefore, the measurement setup is implemented in SHIELD-HIT. The Bragg Peak chamber and the entrance window of the water phantom are simulated by water of equivalent thickness of 16.2 mm. The depth adjustable chambers are simulated by cylindrical slices of 0.1 mm water thickness and a radius of 19.8 mm for the Advanced Roos chamber and 7.5 mm for the Roos chamber.

The elemental compositions of the tissue substitutes are taken from the Gammex phantom description (see Table E.1 on page IX) and the I-values from ICRU49.

SHIELD-HIT input parameters are adjusted to the measured peak width and height in water by adapting the Bragg peak width by an initial energy spread of 0.25 MeV/u. The peak height, is adjusted by PARLEV(39), which is 0.83 for the Roos chamber and 0.71 for the Advanced Roos chamber. The primary carbon ion beam is 299.9 MeV/u and the spot size (FWHM) 5 mm.

The calculated depth-dose curves without a sample are adjusted in range and entrance dose to the measurements. These offsets are afterward applied on the depth-dose curves with media samples. From range differences obtained from a measurement and experiment with sample, an estimation on the accuracy of the I-value of the sample is made.

2.7.2 Simulations on the Water Equivalent Path Length

The WEPL measured in [Ackermann et al., 2008] is assumed to be constant in energy and media thickness. To estimate the accuracy of the WEPL for different energies and tissue equivalent media thicknesses, their influence is studied with SHIELD-HIT.

Therefore, depth-dose curves for carbon ion beam energies of 200, 300 and 400 MeV/u are calculated within a cylindrical water target of radius $r=100$ mm and slices of 0.1 mm. Media of varying thickness are placed at the beam entrance. The calculated thicknesses, d , of adipose, muscle, inner bone, cortical bone, brain, liver and bone mineral are 20 mm, 40 mm and 60 mm. For titanium thicknesses of 1 mm, 3 mm and 5 mm an additional energy of 100 MeV/u is used. These media thicknesses are comparable to media samples used in the measurements by [Ackermann et al., 2008] at HIT with the 'PeakFinder' and GSI in 2.5. The I-values for the compound elements are taken from ICRU49 in Table F.1 on page XI.

2.7.3 A Scaling Method for Carbon Ion Depth-Dose Curves

The accuracy of depth-dose curve parameters (section 2.3.2) with pencil beam algorithms is studied with SHIELD-HIT and a scaling method to obtain water equivalent parameters is introduced and applied as a correction of pencil beam calculations.

In a first step the influence of the primary beam energy and media on depth-dose curve parameters is simulated. Therefore the FWHM_{BC} , DEW and PED are determined according to section 2.3.2 in different homogeneous media for initial carbon beam energies ranging from 100 to 400 MeV/u in steps of 50 MeV/u. The simulated tissue equivalent

media are water, adipose, cortical bone, muscle striated, muscle skeletal and inflated lung. The compositions and I-values of the media are taken from ICRU37 and 44 from Table D.1 and D.2 in the appendix D on page VII. Furthermore, the influence of titanium on the parameters is studied. The I-value and mass density for titanium is taken from ICRU49.

The behavior of depth-dose parameters with energy for one medium is scaled following the reduced relative velocity approach of the projectile in 2.1.1 [Hubert et al., 1989]. Together with the idea to invert the problem, keeping the projectile as fixed and moving the medium in [Fry et al., 2005] for protons, the reduced relative velocity is used to obtain media independent parameters from carbon ion depth-dose curves in a second step. For a fixed projectile and a moving target, the reduced velocity η of the projectile in eq. 2.6 becomes the reduced velocity of the medium η^* :

$$\eta^* = \frac{v_p}{v_0} Z_m^{-\gamma} = \frac{E^{0.5}}{m \cdot v_0} (Z_m)^{-\gamma}, \quad (2.28)$$

where γ is an empirical factor, E the initial beam energy, v_0 the Bohr velocity, m the projectile mass and Z_m the effective atomic charge of the medium, used to adjust parameters obtained in media different of water to their water equivalent parameters. The relative reduced velocity η^* describes the relative reduction of the ion velocity depending on the target medium and is used here as a scaling parameter. The effective atomic charge Z_m of the medium is calculated according to [Murty, 1965]:

$$(Z_m) = \left(\sum_i \lambda_i Z_i^{2.94} \right)^{\frac{1}{2.94}}, \quad (2.29)$$

where λ_i is a weighting factor defined by the atomic mass A_i , charge Z_i , fraction by weight w_i of an atom i with number of elements N and the Avogadro constant N_{av} by:

$$\lambda_i = \left(\frac{N_{av} Z_i w_i}{A_i} \right) / \sum_{i=1}^N \frac{N_{av} Z_i w_i}{A_i}. \quad (2.30)$$

The value of 2.94 in eq. 2.29 is described by a weighted mean over charge dependent scattering processes in the medium based on the CT energy used for CT scans. The value can vary between one and five, depending on the dominant scattering process. However, this value has no influence on the scaling method.

The η^* is further simplified, because the variables m and v_0 in eq. 2.28 are constant for all media and are summarized in a new free parameter C . The behavior of depth-dose curve parameters against primary carbon beam energy E for each medium of an effective atomic charge Z_m are scaled via x , by:

$$x = C E^{1/2} Z_m^{-\gamma}, \quad (2.31)$$

where γ is varied to align the distributions of parameter against x in any media to the distribution observed in water.

2.8 A Dose Comparison of SHIELD-HIT to Geant4 and FLUKA

Depth-dose curves and lateral profiles for 100 and 200 MeV protons and 200 and 400 MeV/u carbon ion beams are compared for SHIELD-HIT07, Geant4.8.1 and FLUKA2008.3.b based on the investigations in [Henkner et al., 2009b] in appendix G on page XV.

The geometry shown in 2.17 is implemented in all three codes: The initial particle field of 10 million particles enters a 20 mm air gap, is afterward shaped to a 100 mm x 100 mm rectangular field by a brass aperture, passes 100 mm air and enters a 500 mm x 500 mm x 500 m water tank. Within the water tank the dose is simulated by cylinders of 100 mm radius. The beam profiles are scored at 50 and 100 mm depth. The resolution is always 1 mm.

Three different brass aperture geometries are simulated including two lateral inhomogeneities. As shown in Figure 2.17 the aperture can be filled with air, half filled with bone and air, or half filled with lung and air.

The media are simulated according to Table I in [Henkner et al., 2009b] in appendix G on page XV. It should be mentioned, that the mean I-values in Table I are not exactly the same. This is because SHIELD-HIT calculates the mean I-value via the Bragg additivity rule, whereas it is directly given in FLUKA and Geant4. The I-values given for Geant4 in Table I in appendix G on page XV are used in FLUKA as well.

From the comparison of MC codes an estimation on the accuracy of dose calculations can be made. Furthermore, the reproducibility of Bragg peaks simulated downstream of air can be made, because the medium air is present in all three aperture setups.

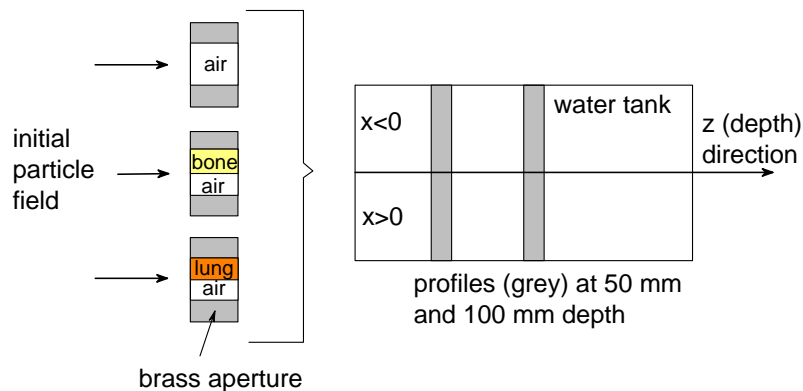


Figure 2.17: Geometry implemented in SHIELD-HIT. Geant4 and FLUKA. Within the apertures of brass, three different structures are simulated. Depth-dose curves are scored along z and beam profiles along the abscissa.

2.9 Benchmark of SHIELD-HIT08

The nuclear interaction model predicts particle interactions and the number of secondary particles. Fragments have a big influence on the shape of the Bragg curve and the RBE. Hence, the numbers and types of interactions have to be simulated accurately. Integral numbers of fragments for SHIELD-HIT are successfully benchmarked in [Gudowska et al., 2004] and [Geithner et al., 2006].

In this work SHIELD-HIT is benchmarked against total numbers of primary and secondary particles from initial proton or carbon ion beams. For protons, the model predictions are compared to measurements from a Multi Layer Faraday Cup (MLFC). For carbon ions, differential cross sections and depth distributions of primary and secondary particles are compared to measurements. Furthermore, the influence of PARLEV(39), (34) and (33) on the calculations is studied.

2.9.1 The Influence of PARLEV(39) on the Fragmentation Process

As already mentioned, PARLEV(39) re-normalizes the cross section of inelastic interactions of ions and influences the attenuation of the projectile and the number of produced fragments. The influence of PARLEV(39) on depth-dose curves and differential cross sections of carbon ions is studied for PARLEV(39)=1.0 and 0.8.

2.9.2 Test of the Total Inelastic Cross Section with a Multi Layer Faraday Cup

The nuclear interaction model in SHIELD-HIT is tested in a comparison to measurements for 160 MeV protons with an MLFC in [Gottschalk et al., 1999] and calculations for Geant4 in [Paganetti and Gottschalk, 2003]. The MLFC is shown in Figure 2.18. It is

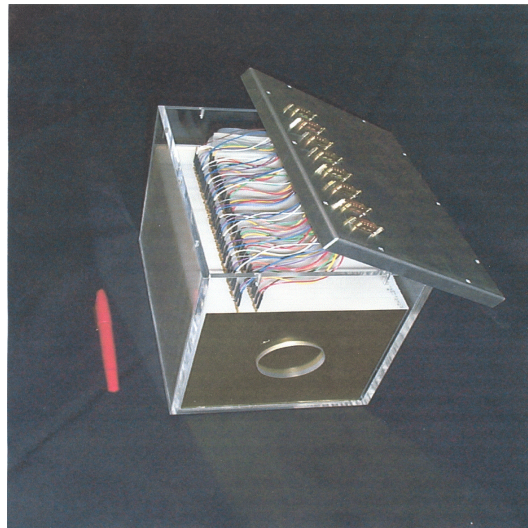


Figure 2.18: Picture of the MLFC as used for the experiment with 160 MeV protons.

made of alternating polyethylene and brass slabs. It measures charge from the potential difference between the center of two polyethylene sheets. The MLFC is able to distinguish between EM and nuclear interactions. The signal in the build up region is entirely

from nuclear interactions whereas the signal in the peak is from EM interactions. This is because the MLFC is only sensitive to a change in the net charge, i.e. the production of a charged fragment or the stopping of a particle.

The concept of the MLFC is shown in Figure 2.19. When a particle undergoes nuclear reactions in A, the measured signal is proportional to the charge difference from incoming and outgoing particles. Whereas the incoming particles add charge, the secondary particles remove charge from the point of interaction. In B an electron is knocked out from brass to CH₂. The electron and the captive ion it left behind will "bind" each other and no net charge is detected. When the particle stops in brass in C, it is directly measured, because it attracts an electron from the ground state which flows through the integrating brass slab. If the particle stops in CH₂, it attracts an electron from the neighboring conducting plates, which fly through the integrator as well. A more detailed description of the properties and the design of the MLFC, the electronics and the implementation in Geant4 can be found in [Gottschalk et al., 1999] and [Paganetti and Gottschalk, 2003].

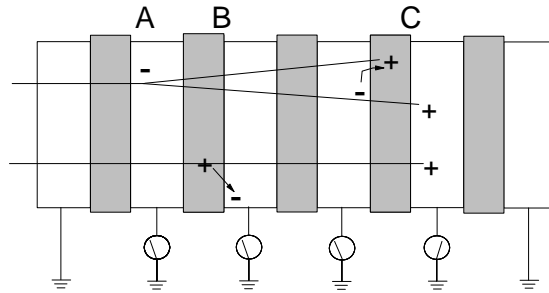


Figure 2.19: The concept of the MLFC and possible events are shown in A, B and C.

The MLFC geometry and initial beam parameters in SHIELD-HIT are taken from the description of the measurement device in [Paganetti and Gottschalk, 2003]. The brass sheets have dimension of 150 mm x 150 mm x 0.0254 mm and a mass density of 8.489 g/cm³. The thickness of the 150 mm x 150 mm polyethylene sheets linearly increases from 3.134 to 3.202 mm and their mean thickness is 3.17 mm. The incident proton beam properties are $E = 159.7$ MeV and $\Delta E = 0.5$ MeV. 20 million protons are used for the calculation.

In SHIELD-HIT the charge at a point of interaction is accumulated due to two processes: First, inelastic nuclear interactions (or nuclear reactions) where a positive charge from the incident particle and a negative charge from all secondaries contribute to the net charge. Second, the absorption of charged particles or fragments with a positive charge. The net charge is determined through the subtraction of the charge from the final state to that of the initial state. E.g., for a (p, p') reaction the net charge at the point of interaction is 0, because the incoming proton adds a charge of +1 and the scattered proton a charge of -1. At the point of absorption of p' , the net charge is +1.

For carbon ions the process is more complicated, because there are several light fragments contributing to the charge as well. The basic idea and also the scoring procedure

within SHIELD-HIT is the same as for protons, because the fragments are simulated regardless. From the calculations with the MLFC geometry for carbon ions, the sensitivity of the MLFC toward fragmentation is studied.

Here, the charge is separated on the generation of the particles. The "generation number" is determined from the number of interactions the particle underwent. Generation 0 are primary particles, generation 1 particles with 1 nuclear interaction, generation 2 with 2 interactions, and so on. If the fragments have a low impact on the total charge in the MLFC, it would not be sensitive enough to test the total inelastic cross section of MC codes.

2.9.3 Benchmark of Differential Cross Sections of Fragments

In [Haettner et al., 2006] and [Haettner, 2006] differential cross sections of primary and secondary particles from a 400 MeV/u carbon ion beam at GSI, Darmstadt were measured in 2005. The number of carbon, boron, beryllium, lithium, helium and hydrogen particles against the lateral angle were obtained downstream of water tanks of 59, 159, 258, 279, 288, 312 and 347 mm width by time of flight measurements. Figure 2.20 shows the experimental setup taken from [Haettner, 2006], which is implemented in a simplified version into SHIELD-HIT.

In the SHIELD-HIT calculations the number of fragments are stored during an internal procedure within default angles after 2.94 m of air as reported in [Haettner, 2006]. The measured FWHM of the beam is given there by 5 mm and the spread of the primary energy spectrum $\Delta E/E$ by a not measured assumption of about 0.5 % .

From calculations with the default SHIELD-HIT setup for PARLEV(values), another setup is studied to predict the differential cross sections superior than with the default values. Therefore, the values of PARLEV(39), (34) and (33) are varied from the values of 1.0.

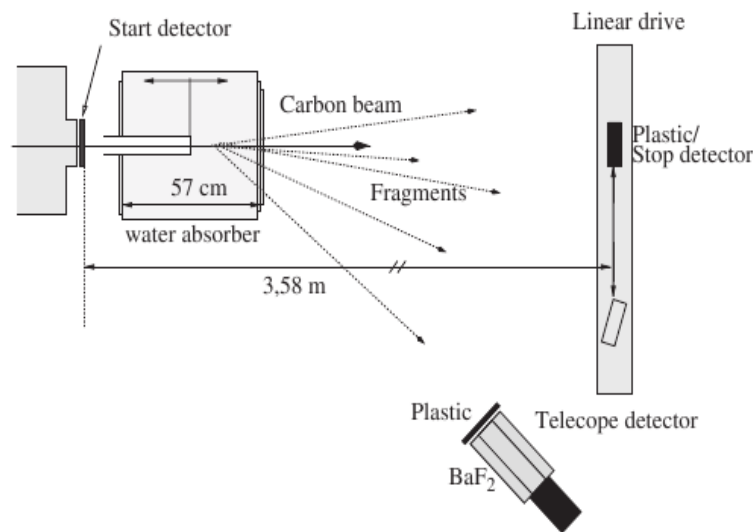


Figure 2.20: Measurement setup used at GSI to obtain angular distributions from secondary particles of a 400 MeV/u carbon ion beam, which are not yet published.

2.10 Neutron Equivalent Dose from Carbon Ion Treatment

A directly clinically relevant application of MC codes is shown in this section and was started within a research stay at the “Physics Research Group” at the Massachusetts General Hospital (MGH) in Boston, USA. The MC code Geant4 is used here, as for MC based treatment planning on CT data a voxelized geometry of the patient is needed, which can not be calculated with SHIELD-HIT.

The study on neutron equivalent doses, which are a measure of the secondary cancer risk, from carbon ion treatments is based on the investigations for scattered protons in [Jarlskog and Paganetti, 2008b] with Geant4. The equivalent dose in various organs due to neutrons was derived as a function of distance to the target, patient age dependent body volume, function of field parameters and the patients body tissues. These distributions are recalculated for the same treatment plans from the currently used carbon ion treatment planning system TRiP98 and first results are presented in this thesis.

Six different treatment plans are calculated for cylindrical target volumes in water of total length of 50 mm and 100 mm and diameters of 30, 60 and 90 mm with TRiP98. From these treatment plans the phase space is determined, which describes the initial particle field. This phase space is used for the calculations with Geant4.9.2.

To simulate patient geometries, a series of tomographic computational phantoms of patients for use in medical dosimetry have been developed at University of Florida in [Lee et al., 2006] and are implemented in Geant4. To simulate the anatomy of an adult patient the VIP-Man computational phantom is used [Xu et al., 2000].

The phantoms were placed in the reference frame of the simulation in Geant4, so that one of the six fields is centered to the median projection of the brain. Geant4 simulates absorbed doses $D_{R,T}$ from the phase space derived with TRiP98 in the phantoms. The organ equivalent dose $H_{R,T}$ in an organ T due to energy deposited by particles of type R is calculated by:

$$H_{R,T} = w_R \cdot D_{R,T}, \quad (2.32)$$

where $D_{R,T}$ is the absorbed dose deposited in an organ T by particles of type R and energy E , and w_R is the radiation weighting factor for neutrons [ICRP, 2003] by:

$$w_R = \begin{cases} 5 & E/MeV < 0.5 \\ 2.5 & 0.5 < E/MeV < 1 \\ 1.1 & E/MeV > 1 \end{cases} \quad (2.33)$$

3 Results

3.1 Determination of the mean I-Value for Water

Figure 3.1 shows simulated I-values for water, resulting from the fit to the measured peak positions available from [Schardt et al., 2008], against primary lithium, carbon and oxygen energies ranging from 100 to 400 MeV/u. The obtained mean I-value of 80.7 ± 2.3 eV is close to the aforementioned value of 80.8 eV recently published in [Paul et al., 2007]. The uncertainty of 2.3 eV is the standard deviation of the mean I-value from all particles and primary energies.

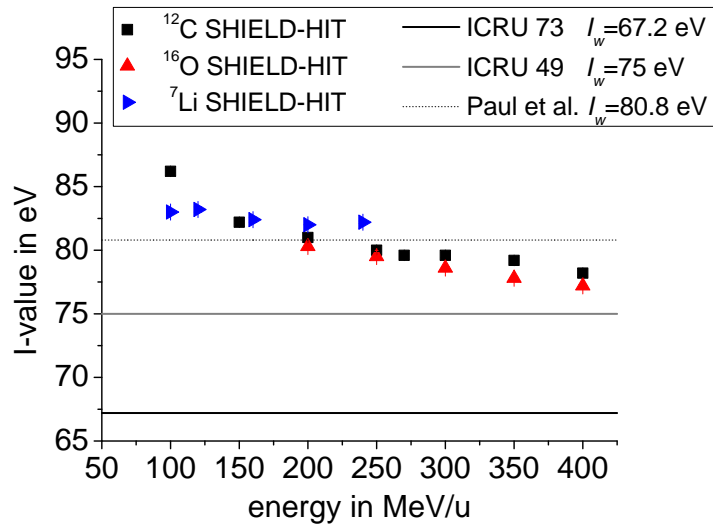


Figure 3.1: I-value for water against primary beam energy, determined from experimental Bragg peak positions.

Table 3.1 shows the difference between measured and SHIELD-HIT calculated Bragg peak positions in water and the I-values required in SHIELD-HIT to achieve the measured peak positions. For the calculations in the third column I_w is set to 67.2 eV as recommended in ICRU73 for $Z > 2$ particles. The difference between measured and calculated Bragg peak position increases with increasing beam energy.

Table 3.1: Measured minus calculated ($I_w=67.2$ eV) Bragg peak positions and the I-values required in SHIELD-HIT to achieve the measured positions. Values in brackets are errors from the fit in 2.6.1.

particle type	particle energy in MeV/u	measured minus calculated Bragg peak positions in mm	estimated I-value in eV
${}^7\text{Li}$	100	1.7	83.0 (1)
	120	2.4	83.2 (2)
	160	3.6	82.4 (2)
	200	5.1	82.0
	240	6.9	82.2 (1)
${}^{12}\text{C}$	100	0.3	86.2 (1)
	150	1.4	82.2 (1)
	200	2.1	81.0
	250	2.7	80.0 (1)
	270	3.1	79.6 (1)
	300	3.5	79.6 (1)
	350	4.4	79.2 (2)
${}^{16}\text{O}$	400	4.7	78.2 (3)
	200	1.5	80.3
	250	2.0	79.5 (1)
	300	2.4	78.6 (1)
	350	2.8	77.8 (1)
	400	3.3	77.2 (1)

3.2 The Accuracy of the mean I-Value for Compounds

The effect of the uncertainty of the mean I-value of compounds given in ICRU49 and 37 on the range is shown in Table 3.2 for a 270 MeV/u carbon ion beam with SHIELD-HIT. The Δr is the shift of the overall range of the carbon beam toward lower and higher depth according to the uncertainty of mean I-values ΔI .

The overall range of 151.6 mm in adipose is shifted by ± 1.8 mm. The range of 139.2 mm in muscle is influenced by ± 0.9 mm with a given ΔI of 5 %. The mean I-value for titanium and water is given by ± 5 eV and ± 3 eV. From this values, the overall ranges of 44.4 mm and 143.4 mm can be simulated with an accuracy of ± 0.5 mm and ± 0.7 mm for titanium and water, respectively.

3.3 The Water-to-Air Stopping Power Ratio

The effect of varying the I-value (taken from Table 2.5) on the stopping power ratio for a 140 MeV proton beam is demonstrated in Figure 3.2. The derived stopping power ratio from ICRU tabulated stopping power data, set 3 (red line), shows a local maximum at about 120 mm depth and has a 1.3 % lower peak than compared to the ratio calculated with the Bethe-Bloch formula and an I-value of 75 eV, set 4 (ocher line). Furthermore, the $S_{w/air}$ obtained with ICRU data is 0.2 % higher than with Bethe-Bloch and $I_w = 75$ eV. The calculated $S_{w/air}$ in set 4 is about 0.3 % higher than the value of 1.13

Table 3.2: Shift of simulated 270 MeV/u carbon ion beams in a medium according to the uncertainty in the I-value of ICRU.

medium	ΔI	Δr in mm	Δr %
adipose	10 %	± 1.8	1.20
cortical bone	10 %	± 1.1	1.29
inner bone	10 %	± 1.2	1.29
muscle	5 %	± 0.9	0.70
titanium	± 5 eV	± 0.5	1.13
water	± 3 eV	± 0.7	0.50

recommended by IAEA. An increase to $I_w = 80.8$ eV, to better reproduce measured ranges with SHIELD-HIT, reduces the stopping power ratio to 1.119. Shown in violet is the $S_{w/air}$ as a result of eq. 2.22 for I-values from set 5. It differs about 0.2 % from the SHIELD-HIT calculations in grey.

Set 6 in orange shows the influence of I_{air} on the $S_{w/air}$, here $I_w = 80.8$ eV and $I_{air} = 88.8$ eV as suggested in [Paul et al., 2007]. Compared to the IAEA constant, the $S_{w/air}$ is decreased by 0.42 %.

The $S_{w/air}$ is not constant as assumed in IAEA TRS-398. An increase from 1.119 to 1.12 toward 135 mm depth is observed in set 5.

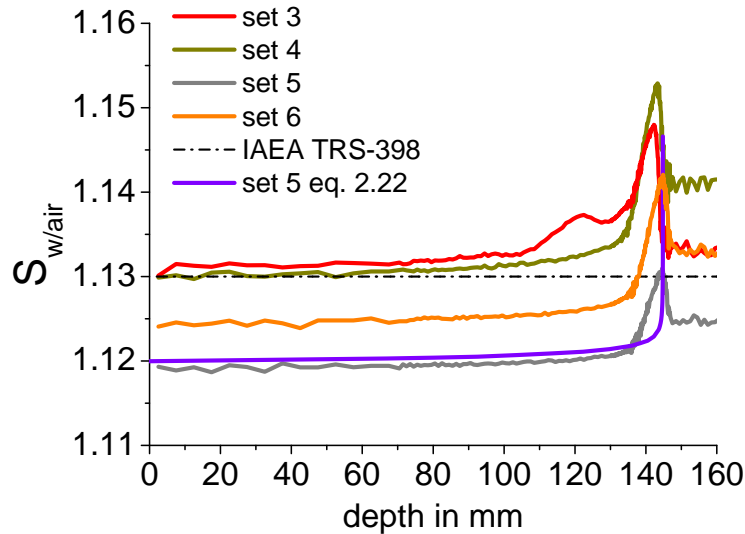


Figure 3.2: The water-to-air stopping power ratio for a 140 MeV proton beam with I-values according to the sets in Table 2.5.

ICRU tabulated (set 3) and SHIELD-HIT calculated (set 5) stopping power ratios for proton energies from 50 to 170 MeV are shown in Figure 3.3. A local maximum right before the $S_{w/air}$ peak is observed for all proton beam energies. The $S_{w/air}$ peak gets smaller and broader with increasing primary beam energy due to energy straggling.

Figure 3.4 shows the stopping power ratios for various proton and carbon ion beam energies versus residual range. By definition the residual range is 0 mm at the Bragg peak, increases toward the entrance region, and has a negative value in the distal fall-off

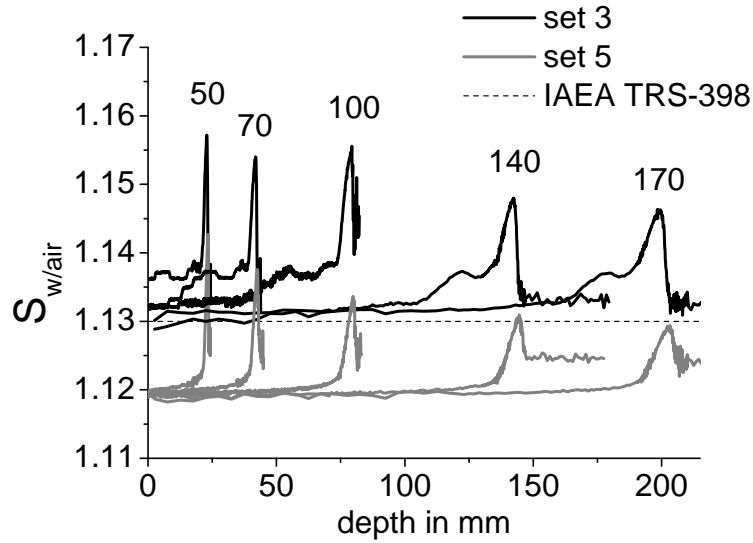


Figure 3.3: Water-to-air stopping power ratio for protons of different energies in MeV simulated with set 3 and 5.

region, downstream of the Bragg peak. The data are shown up to the maximum water-to-air stopping power ratio, $S_{w/air,max}$. Proton data are taken from set 5 while carbon ion data are taken from Figure 4 on page 1233 in [Henkner et al., 2009a] (appendix G on page XXV).

The $S_{w/air}$ is roughly constant at 1.12 and sharply increases toward the distal fall-off region. For 50 MeV protons, the increase in $S_{w/air,max}$ in the fall-off region is less than 2.5 %, while for carbon ions it is greater than 6 %. Furthermore, the $S_{w/air,max}$ and the distance past the Bragg peak at which this maximum occurs are smaller for protons than for carbon ions and decrease with energy. This is due to the higher energy straggling observed for protons which broadens the Bragg peak and increases with increasing energy.

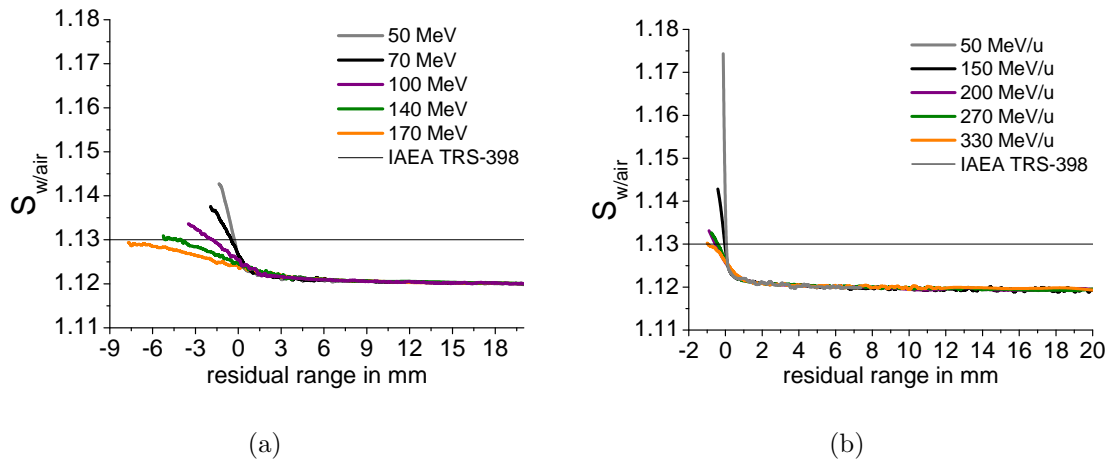


Figure 3.4: The stopping power ratio according to the residual range of proton beams (a) and carbon beams (b) of different energies in MeV/u for set 5. Figure 3.4 (b) is taken from [Henkner et al., 2009a] in appendix G.

3.4 Required Size of a Water Tank for Dosimetry

Dose calculation results for various water tank lengths for 180 and 250 MeV protons and 350 and 450 MeV/u carbon ions are shown in Figure 3.5 and 3.6, respectively. There is no observed systematic influence from the lateral dimensions of a water phantom on the dose beyond the uncertainties of the calculations. Even if the phantom width is 120 mm, which is only slightly larger than the incoming $100 \times 100 \text{ cm}^2$ particle field. However, in Figure 3.6 (b) a deviation of about 2 % of the dose calculated with 300 mm side length compared to 500 mm is observed.

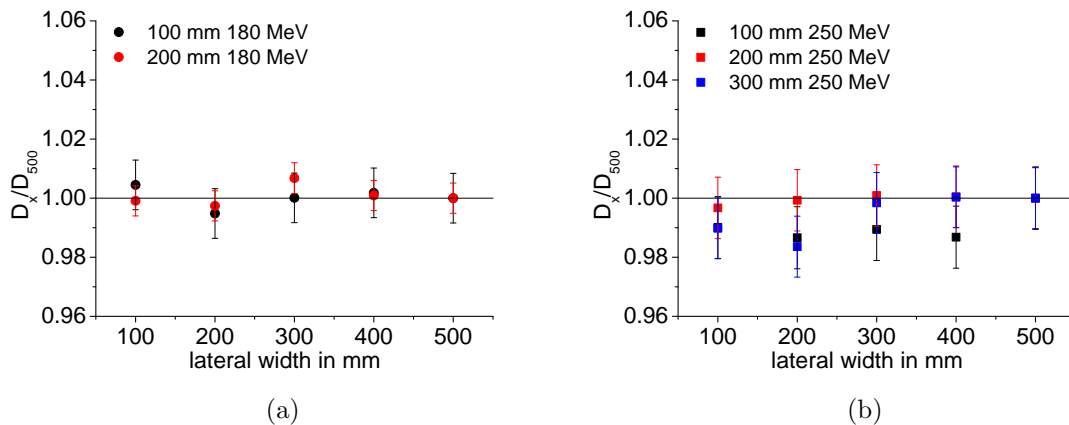


Figure 3.5: Simulated proton dose relative to the dose for a $500 \times 500 \times 500 \text{ mm}^3$ water tank. The initial beam energy is 180 MeV in (a) and 250 MeV in (b). The abscissa shows the lateral dimension of the water tank while the depth is constant at 500 mm. The symbols in the legend belong to the position of the center of the $10 \times 10 \times 10 \text{ mm}^3$ volumes on the central beam axis at 100, 200 and 300 mm depth.

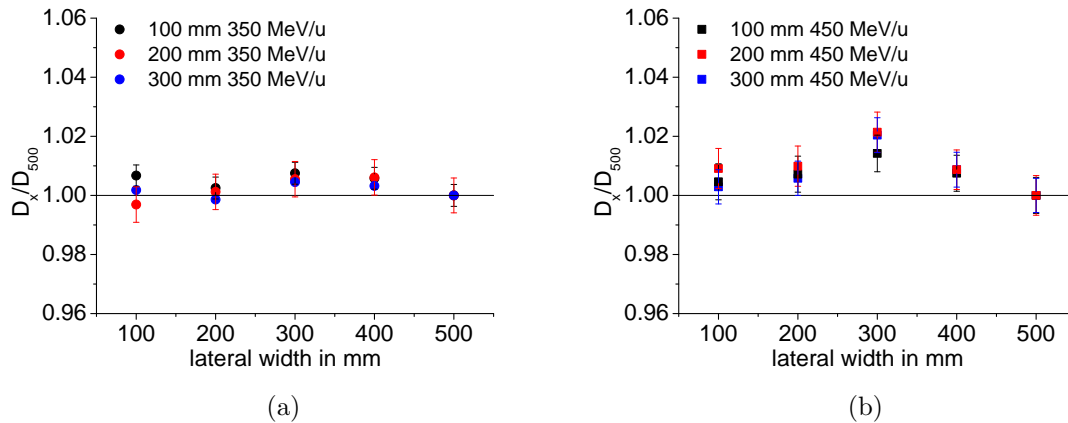


Figure 3.6: Simulated carbon dose relative to the dose for a 500 x 500 x 500 mm³ water tank. The initial beam energy is 350 MeV/u in (a) and 450 MeV/u in (b). The abscissa shows the lateral dimension of the water tank while the depth is constant at 500 mm. The symbols in the legend belong to the position of the center of the 10x10x10 mm³ volumes on the central beam axis at 100, 200 and 300 mm depth.

3.5 Depth-Dose Distributions Measured at GSI

To study the agreement of measured and calculated depth-dose distributions in water downstream of adipose, cortical bone and titanium, the SHIELD-HIT results in water without samples are fully adjusted to the measurements. A first analysis showed, that SHIELD-HIT ranges with samples calculated with media I-values from ICRU, deviate up to 1.75 mm to the measured ranges. Since the calculated range in water is adjusted to measurements, this disagreement should come from range calculations in the media.

For correct range calculations the mean I-values of the media are changed. These adjusted I-values together with ICRU37 and 49 values are summarized in Table 3.3. Whereas the required I-value for adipose and bone is within the accuracy given in ICRU49, the value for titanium is increased by 23.4 %.

Table 3.3: I-values obtained from the comparison of measured and simulated depth-dose curves downstream of different media in water.

sample medium	mean I in eV from calculations	mean $I \pm \Delta I$ in eV from ICRU37 and 49
adipose	63.74	63.2 ± 6.32
cortical bone	104.54	106.4 ± 10.64
titanium	304.00	233.0 ± 5

Figure 3.7 shows the measured and SHIELD-HIT calculated depth-dose distributions with a Roos- and an Advanced Roos chamber in water and downstream of adipose, cortical bone and titanium samples in water. The simulated distributions shown here are already corrected for the I-value and only the region of interest is shown. The full curves are shown in the appendix B in Figure B.1. The distributions obtained only in water (without samples) are identical in (a) to (c). Figure 3.7 (a) show depth-dose curves

obtained in water downstream of a 56.2 mm adipose tissue sample (black and grey) and without sample (blue and orange). The simulated Bragg peak height downstream of adipose deviates about 17 % and 15 % from the measurements for the Roos- and Advanced Roos chamber, respectively. Furthermore, a disagreement in the FWHM_{BC} of the Bragg curve is observed. In the measurements, the mean FWHM_{BC} is up to 35 % higher than in the calculations.

The results downstream of a 56.2 mm cortical bone sample is shown in (b). Here, the water curves are not shown due to the depth scale chosen to focus on the bone distributions. The simulated dose with the Roos chamber is about 3 % higher in the peak than compared to the measurements. For the Advanced Roos chamber a deviation of about 4 % is obtained. The FWHM_{BC} deviates about 13 % and is larger for the measurements.

A very good agreement between measured and calculated depth-dose curves is obtained with the 2.83 mm thick titanium plate in Figure 3.7 (c), where the agreement of the measurements and calculations is within 2 %.

The peak height obtained with the Roos chamber is higher than with the Advanced Roos chamber. This is due to the different sensitive electrode diameter. Whereas the Advanced Roos chamber integrates over a diameter of 39.6 mm, the Roos chamber integrates only over 15 mm.

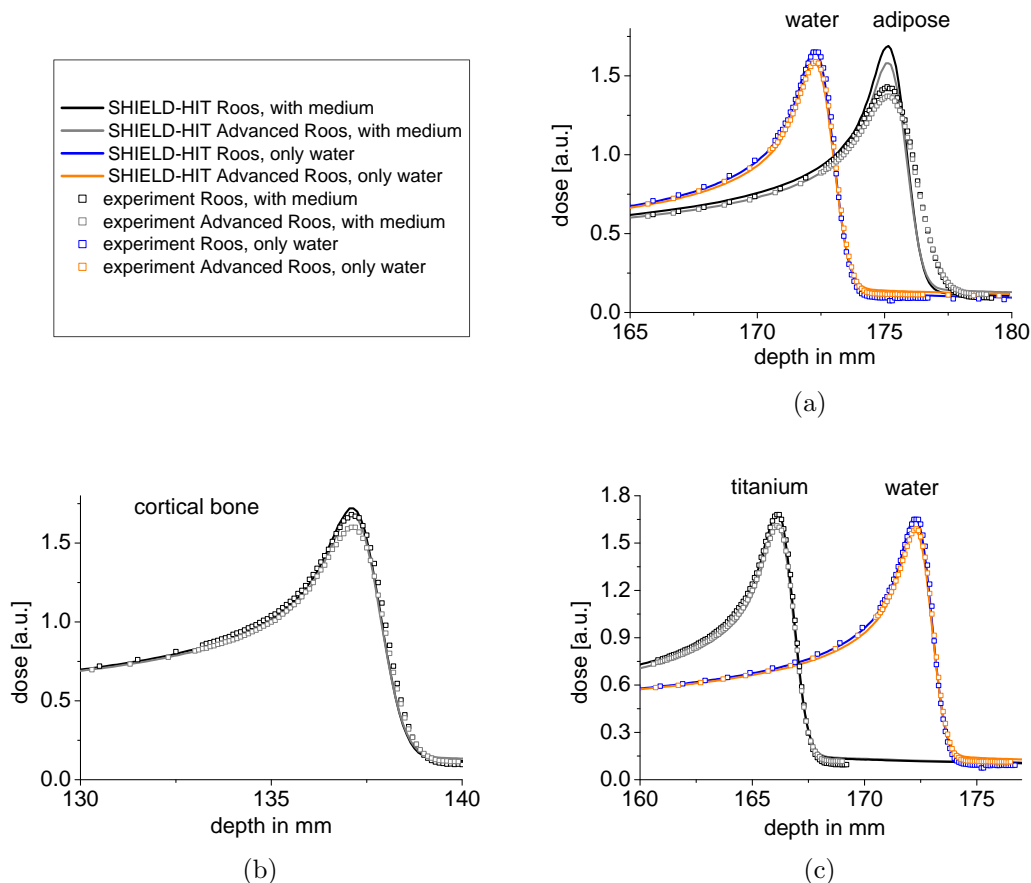


Figure 3.7: Measurements (squares) and SHIELD-HIT calculations (line) on the GSI experiment with samples from the Gammex phantom. Curves obtained in “water” means without samples and in “adipose”, or “cortical bone”, or “titanium” means with either of this media samples in the beam path.

3.6 The Water Equivalent Path Length

The WEPL from measurements and simulations with different media thickness and energy is shown in Table 3.4. The value given for SHIELD-HIT is the mean average over the results in Figures 3.8 and 3.9. The measured WEPL at GSI (56.2 mm sample thickness) and HIT [Ackermann et al., 2008] (20 mm sample thickness) are in good agreement, although the samples at GSI were placed in water and at HIT they were in front of the phantom. The simulated WEPL differs only by 1 % for tissue equivalent samples from the Gammex phantom.

With SHIELD-HIT the WEPL for titanium is 3 % higher than measured. The difference between the WEPL and the mass density of the medium increases with increasing mass density.

The standard deviation of the mean WEPL derived from simulations of different energies and media thicknesses is less than 0.5 % for tissue equivalent media and 1 % for titanium. Hence a dependence of the WEPL on energy or medium thickness is not observed.

Table 3.4: Density and WEPL for various media obtained from measurements at GSI and HIT and SHIELD-HIT simulations. The WEPL for SHIELD-HIT is the arithmetic mean and the standard deviation in brackets. The last column shows the difference between the mean WEPL with SHIELD-HIT and the mean WEPL from the experiments.

medium	mass density in g/cm ³	measured WEPL (GSI)	measured WEPL (HIT)	simulated mean WEPL (SHIELD-HIT)	difference WEPL(MC) - WEPL(exp)
adipose	0.942	0.946	0.954	0.938 (0.002)	-0.012
muscle	1.050		1.031	1.029 (0.001)	-0.002
brain	1.052			1.069 (0.001)	
liver	1.089			1.067 (0.004)	
inner bone	1.147		1.101	1.092 (0.003)	-0.009
bone mineral	1.153			1.097 (0.003)	
cortical bone	1.823	1.627	1.618	1.634 (0.007)	+0.0115
titanium	4.540	3.180	3.160	3.291 (0.046)	-0.1210

The simulated and measured WEPL against beam energy for the first six media in Table 3.4 are shown in Figure 3.8. The WEPL for cortical bone and titanium are shown in Figure 3.9. The symbols in the legend belong to the thickness of media in mm used in the simulations with SHIELD-HIT (MC) and the measurements at GSI and HIT.

The error bar of the WEPL is obtained from an error propagation of the range uncertainties. For the control system of the MP3 water phantom and the 'PeakFinder' these are 0.01 mm. The uncertainty in the SHIELD-HIT simulations is 0.05 mm, derived from 0.1 mm bins.

The maximum uncertainty in the WEPL calculations for ICRU37 media is less than 0.4 % . If the uncertainty of the I-value in Table 2.4 is taken into account, the WEPL differs up to 1.4 % around its mean value. For titanium the mean uncertainty in the WEPL is 1.4 % while the uncertainty including ΔI is 1.8 %. However, the error bars depend on the thickness of the media and are therefore large for titanium.

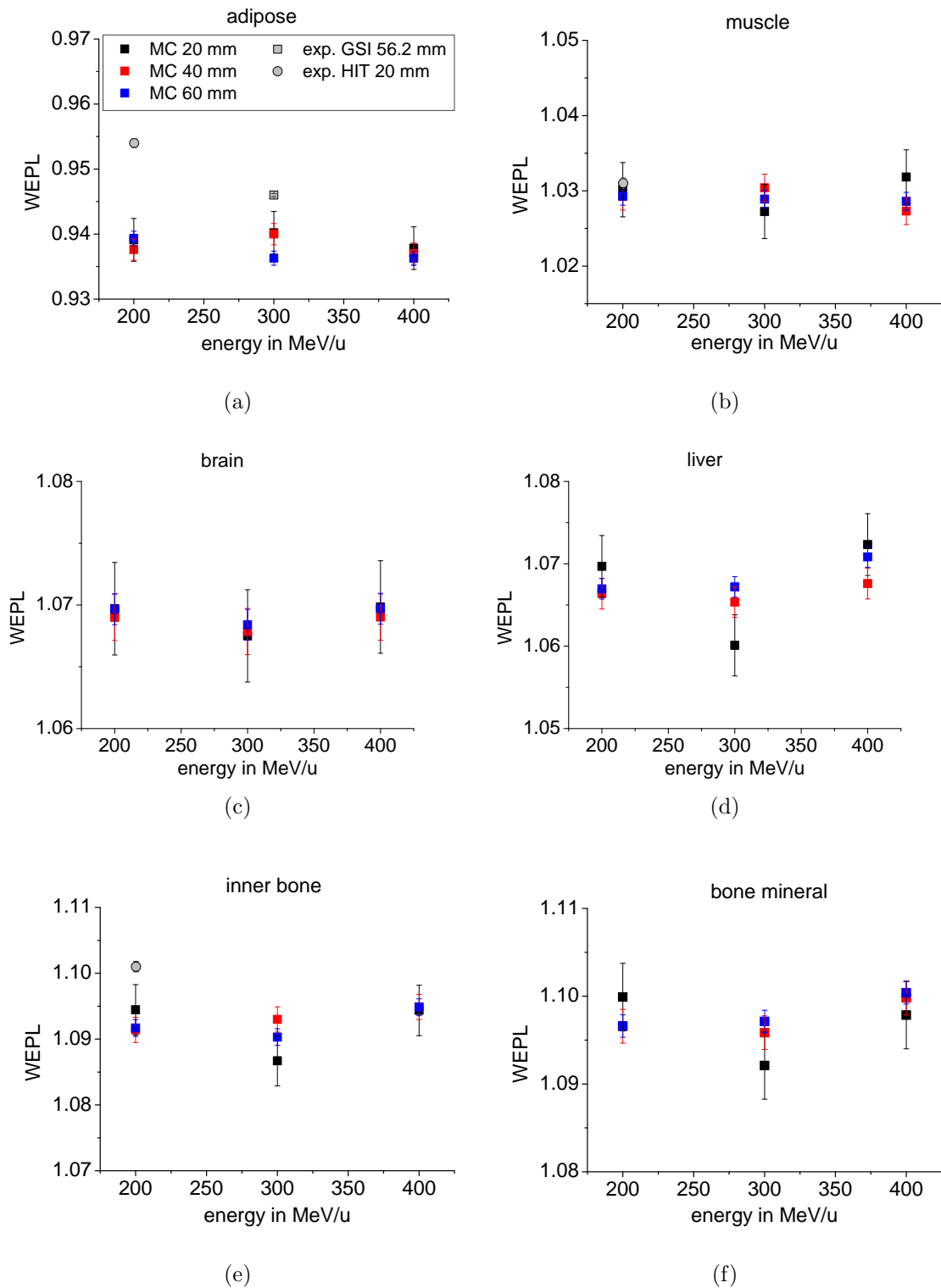


Figure 3.8: SHIELD-HIT simulated and experimentally obtained WEPL for the first six media in Table 3.4. The thickness of the Gammex samples during measurements at GSI are 56.2 mm, and 20 mm at HIT. The thicknesses were 20, 40 and 60 mm for SHIELD-HIT simulations.

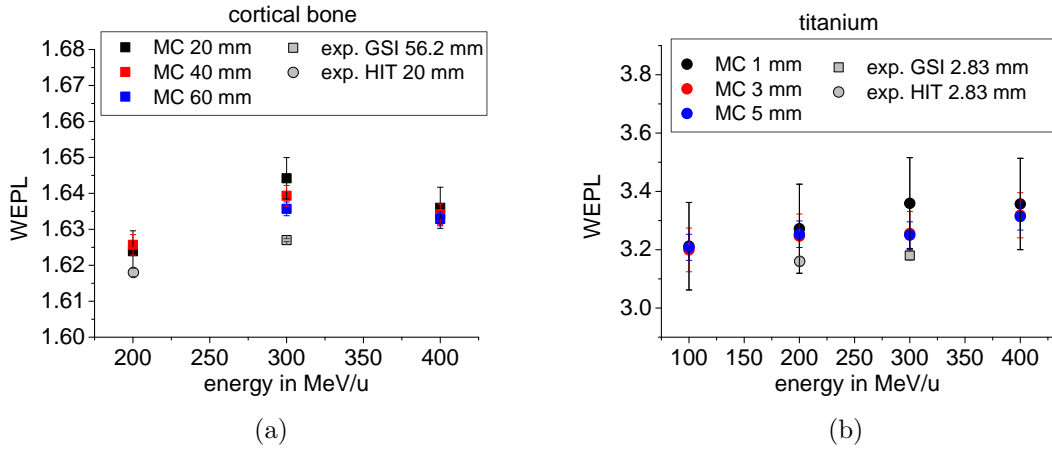


Figure 3.9: Measured and SHIELD-HIT simulated WEPL for cortical bone and titanium. The dimensions for cortical bone samples are the same as in Figure 3.8. The titanium sample is 2.83 mm thick in the measurements and 1, 3 and 5 mm in the simulations.

3.7 Scaling Method for Carbon Ion Depth-Dose Curves

The calculated parameters of a depth-dose curve; Full Width at Half Maximum of the Bragg peak (FWHM_{BC}), Distal Edge Width (DEW) and Peak-Entrance-Dose (PED) are shown in Figures 3.10, 3.11 and 3.12. The behavior of the three parameters in various homogeneous target media against the primary carbon beam energy is shown in (a). The FWHM_{BC} and DEW increase with increasing energy and decreasing target media density. The PED decreases with increasing energy and decreasing target density. The largest influence on the parameters is observed in inflated lung and titanium.

The calculated effective atomic charges Z_m of the simulated media according to eq. 2.29 are shown in Table 3.5. For titanium $Z_m = 22$.

Table 3.5: Calculated effective atomic charge Z_m for the studied media.

medium	adipose	water	muscle striated	muscle skeletal	inflated lung	cortical bone
Z_m	6.23	7.42	7.46	7.48	7.49	12.97

To express the parameters target media independent, the abscissa is scaled according to eq. 2.31. The free parameters γ and C are derived from the maximum alignment of a parameter distribution against x for all media.

In a first step, γ is varied until the parameter distributions of ICRU37 media are aligned to the parameters in water. Titanium (black triangles) and inflated lung (red stars) are excluded, because the influence of those target media on the parameters are much stronger than for ICRU37 media. Values of $\gamma=0.26$, for the FWHM_{BC} and DEW

and $\gamma=0.1$ for the PED are found to best align the distributions.

In a second step the results in titanium and inflated lung are aligned with the already obtained γ by varying the value C in x in eq. 2.31. For titanium a C of 0.93 shows the best alignment in all parameters. For inflated lung, C is 1.4 for the $FWHM_{BC}$, 1.46 for the DEW and chosen to be 1.0 for the PED.

It turned out that this scaling approach is not feasible for inflated lung, since the behavior of the parameters in energy is stronger than compared to the other media. Only for the DEW the scaling aligns the results for inflated lung to that in water. However, depth-dose curves are only simulated up to 200 MeV/u for inflated lung since the range of the particles is very large for high energies and the geometry has to be extended and cannot be simulated in a reasonable time.

Except for inflated lung, the scaling affects an alignment of all distributions as shown in (b) in Figures 3.10, 3.11 and 3.12. Hence the $FWHM_{BC}$, DEW and PED of the media against energy correlate with the parameters in water by a simple mathematical expression. This expression is obtained from a fit procedure. The results are exponential functions for the $FWHM_{BC}$ and DEW:

$$FWHM_{BC} = (0.03 \pm 0.15) * \exp\left[\frac{x}{(2.17 \pm 0.08)}\right] + (0.05 \pm 0.01) \quad (3.1)$$

and

$$DEW = (0.026 \pm 0.003) * \exp\left[\frac{x}{(2.762 \pm 0.084)}\right] - (0.056 \pm 0.024) \quad (3.2)$$

and a polynomial function for the PED:

$$PED = (9.76 \pm 0.40) - (0.04 \pm 0.05)x - (0.02 \pm 0.002)x^2 \quad (3.3)$$

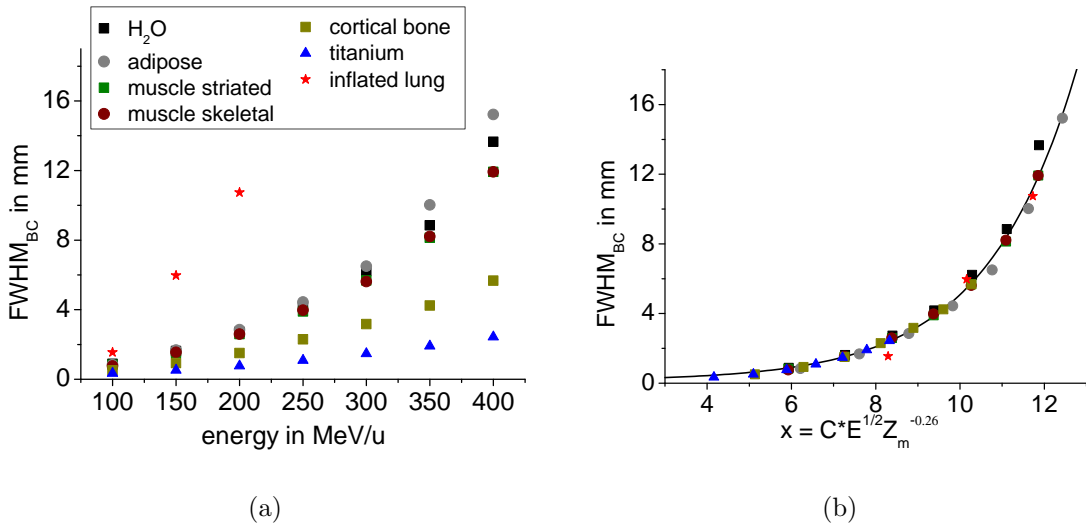
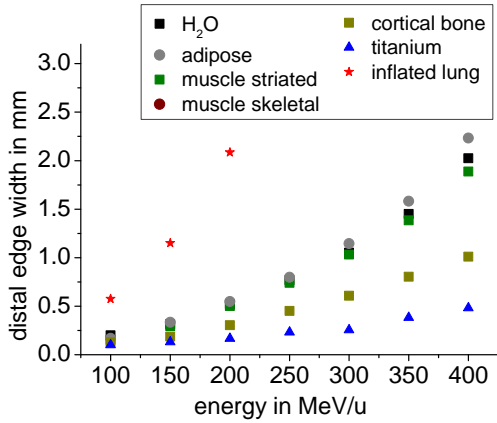
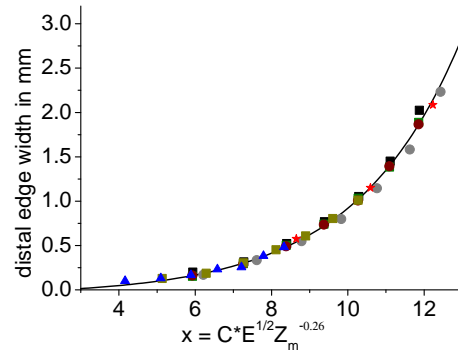


Figure 3.10: $FWHM_{BC}$ against carbon ion energy in MeV/u (a) and with applied scaling (b). The γ in eq. 2.31 is 0.26 and C is 0.93 for titanium, 1.4 for inflated lung and 1.0 for all other media. The black line in (b) is within eq. 3.1.

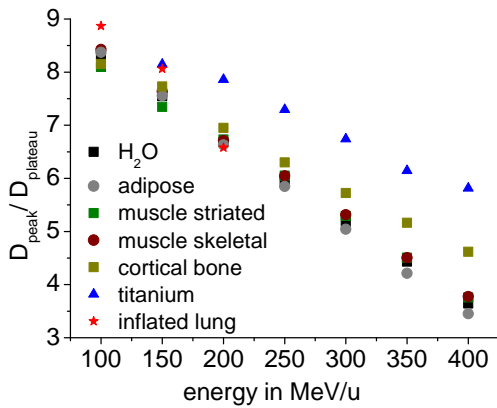


(a)

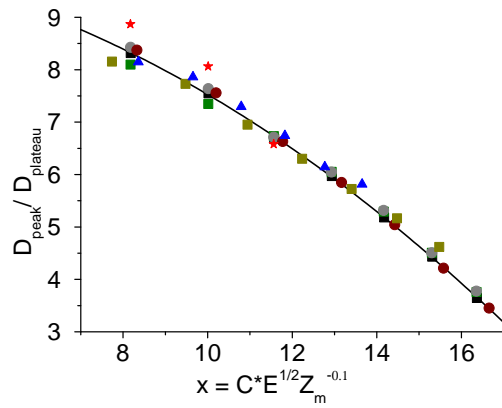


(b)

Figure 3.11: The DEW before (a) and after the scaling (b). The γ in eq. 2.31 is 0.26 and C is 0.93 for titanium, 1.46 for inflated lung and 1.0 for all other media. The black line in (b) is within eq. 3.2.



(a)



(b)

Figure 3.12: The PED $D_{peak}/D_{plateau}$ against the initial carbon ion energy (a) and the abscissa after the scaling (b). The γ in eq. 2.31 is 0.1 and C is 0.93 for titanium and 1.0 or all other media. The black line in (b) is within eq. 3.3.

3.8 Comparison of SHIELD-HIT to Geant4 and FLUKA

The calculations for SHIELD-HIT are performed with $\text{PARLEV}(39)=0.8$.

3.8.1 Depth Distributions for Protons and Carbon Ions

The simulated water depth-dose distributions for the three Monte Carlo codes are shown downstream of air in Figure 3.13, the lateral inhomogeneity of lung/air in Figure 3.14 and bone/air in Figure 3.15. The distributions for 100 and 200 MeV protons are shown on the left and for 200 and 400 MeV/u carbon ions on the right side. Simulations with SHIELD-HIT are in black, Geant4 in blue and FLUKA in orange. A shift of the Bragg peak with SHIELD-HIT toward lower depth than compared to Geant4 and FLUKA is observed in these Figures.

In the very beginning of the plateau SHIELD-HIT and FLUKA agree very well, whereas Geant4 underestimates the other codes by up to 38 % for 200 MeV protons downstream of lung/air in Figure 3.14 (d).

In the fragment tail SHIELD-HIT overestimates the dose derived with FLUKA up to 18 % and Geant4 up to 29 % for 400 MeV/u downstream of lung/air in Figure 3.14 (d).

For depth-dose curves downstream of the lateral inhomogeneities lung/air and bone/air, more than one Bragg peak may be observed per curve. Particles passing through air exhibit Bragg peaks at the positions in Figure 3.13. Particles passing through lung or bone exhibit a second Bragg peak at shallower depth in Figure 3.14 and Figure 3.15 (c) and (d). This is because the particles stop earlier since the mass density for bone and lung is larger than for air and the energy loss in the aperture is larger. Note that 100 MeV protons and 200 MeV/u carbon ions show only a single Bragg peak downstream of the bone/air lateral inhomogeneity, because the particles traveling through bone already stop within the aperture. For lung/air in Figure 3.14, the peaks are much closer together than for bone/air since the mass density of lung is closer to that of water than the mass density of bone is.

Since the bins were only 1 mm the range of the ion beam could not be determined by definition at the 80 % dose in the fall-off. Instead, an extrapolation in the fall-off region to the root position at the abscissa, where the deposited energy is zero, is used to quantify the deviations in Bragg peak position.

The differences in the root position of the Bragg peak between the three MC codes in Table 3.6 are separated in energy and the traversing media in the aperture. The Bragg peak is either from particles traveling through air, lung or bone. The accuracy is within ± 0.08 mm. For carbon ions only the results for 400 MeV/u are shown, because the fall-off region of the Bragg peak from 200 MeV/u is too sharp to sufficiently extrapolate (see Figure 3.13 (b)).

Table 3.6: Mean shift of Bragg peaks from protons and carbon beams downstream of different media from Figure 2.17. The shift is determined at the root position of the lateral fall-off with SHIELD-HIT (S) minus Geant4 (G) or FLUKA (F).

medium	Proton energy in MeV	S - G in mm	S - F in mm
air	100	-0.10	-0.05
	200	-0.30	-0.15
lung	100	-0.86	-0.93
	200	-0.68	-1.51
bone	200	-0.35	-0.17

medium	Carbon energy in MeV/u	S - G in mm	S - F in mm
air	400	-0.08	-0.81
lung	400	-1.31	-1.59
bone	400	-0.84	-0.71

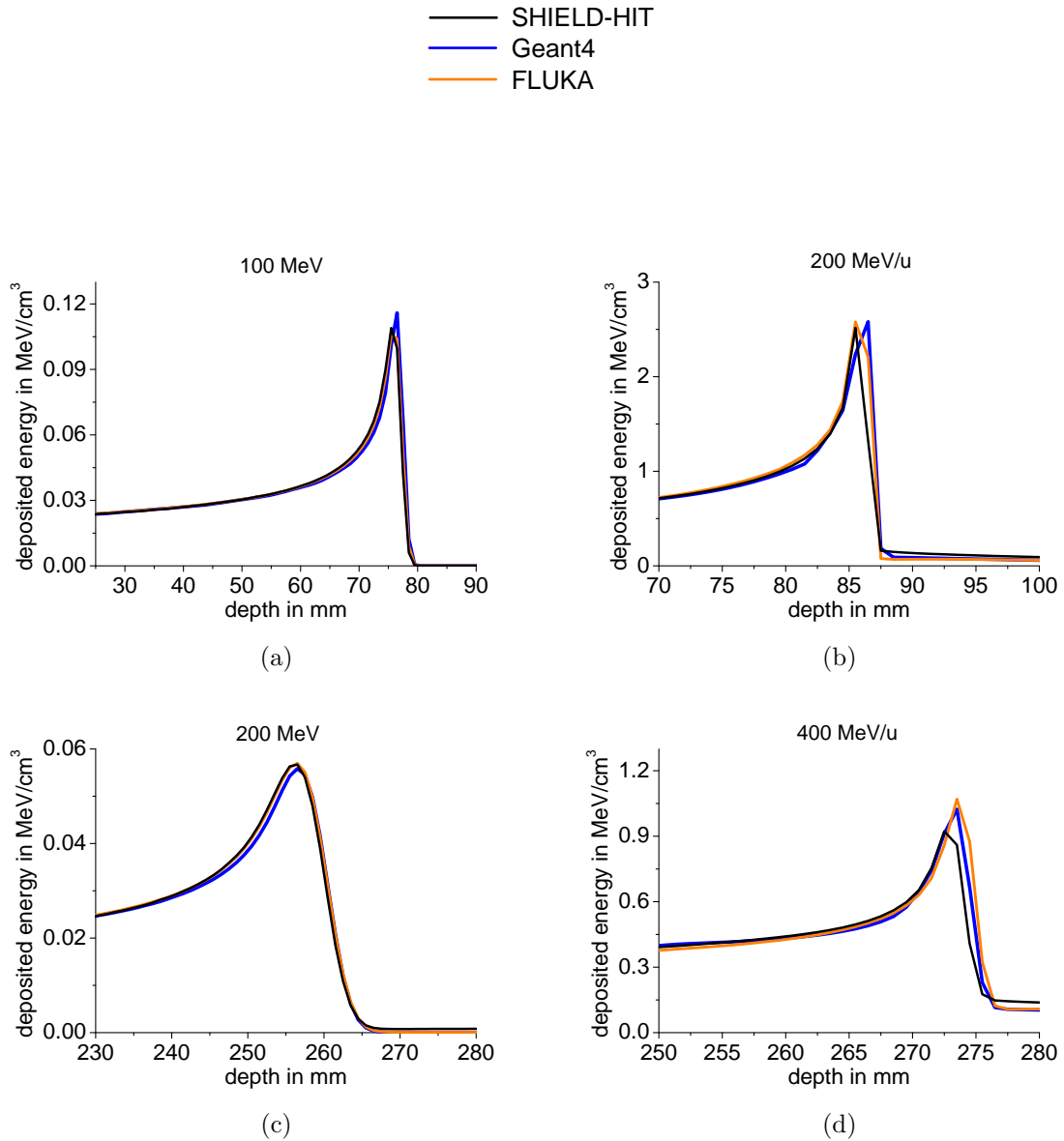


Figure 3.13: Energy distributions in water downstream of air for 100 and 200 MeV protons (left) and 200 and 400 MeV/u carbon ions (right). The whole water depth is shown in appendix A on page I.

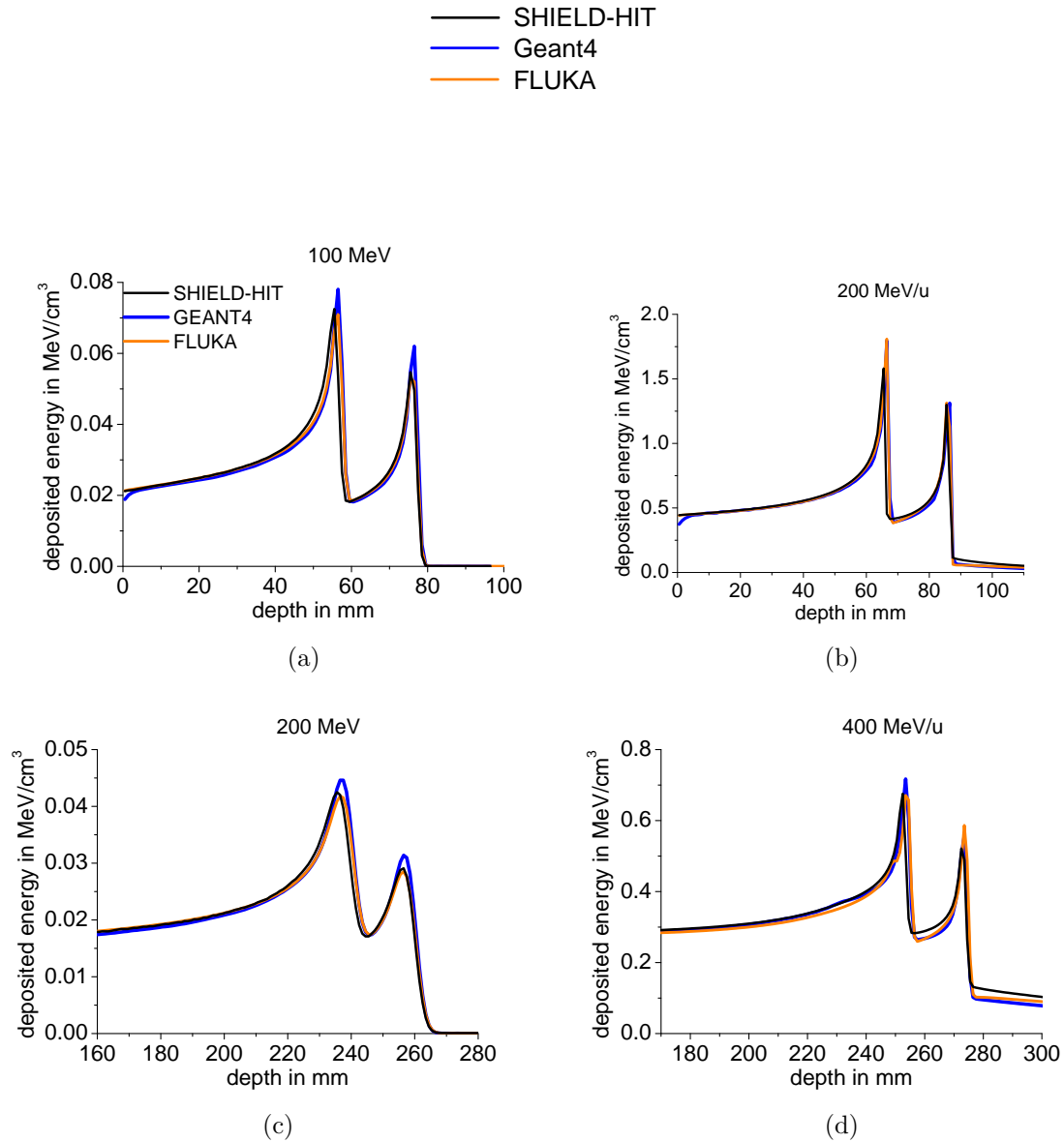


Figure 3.14: Energy distributions in water downstream of lung/air for 100 and 200 MeV protons (left) and 200 and 400 MeV/u carbon ions (right). The whole water depth for (c) and (d) is shown in appendix A on page I.

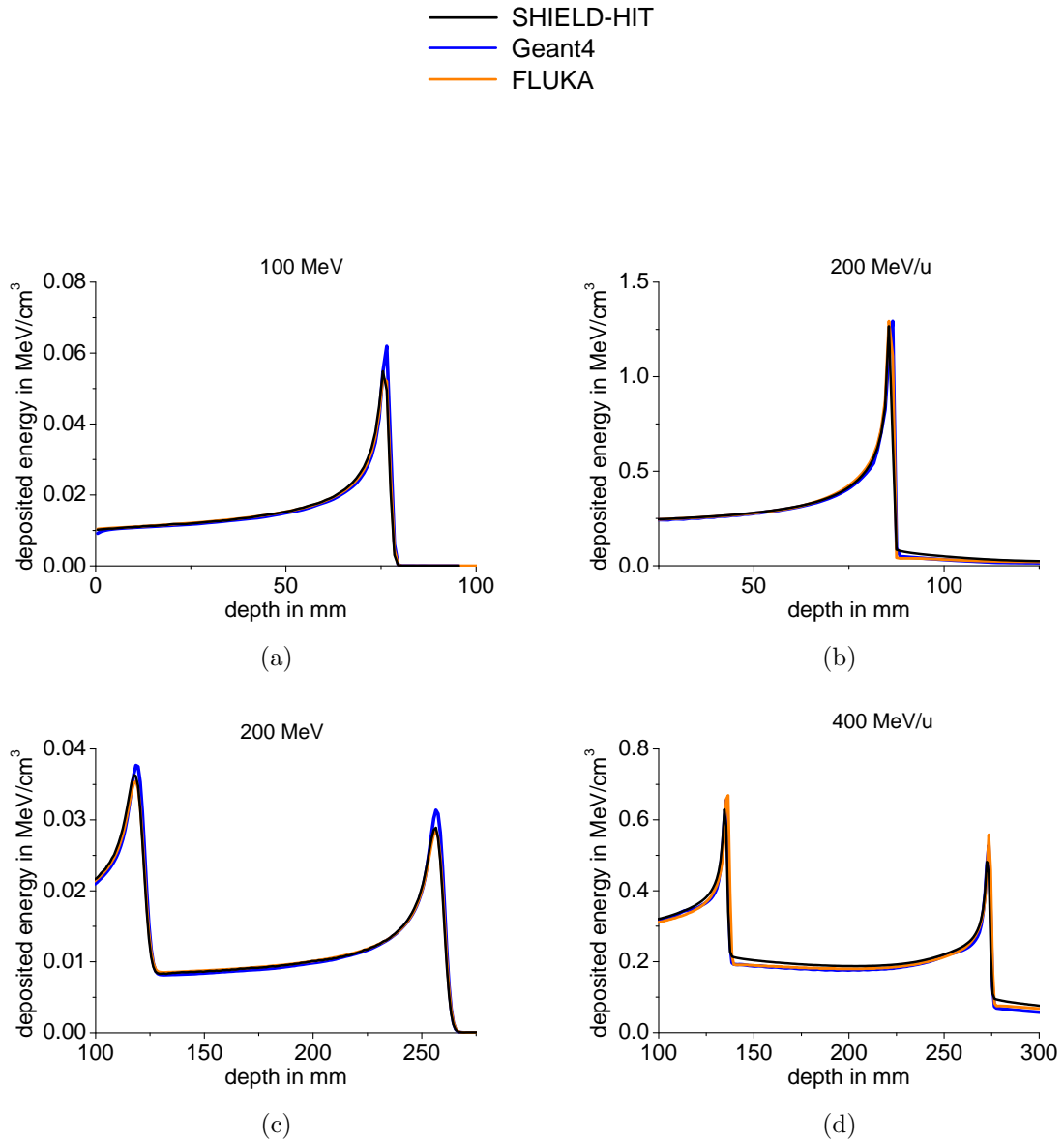


Figure 3.15: Energy distributions in water downstream of bone/air for 100 and 200 MeV protons and 200 and 400 MeV/u carbon ions. The whole water depth for (c) and (d) is shown in appendix A on page I.

3.8.2 Beam Profiles for Protons and Carbon Ions

The beam profiles for SHIELD-HIT, Geant4 and FLUKA are shown in Figures 3.16 to 3.18. The results for protons are shown on the left and carbon ions on the right side. The first row shows the results downstream of air, the second of lung/air and the last row of bone/air. Figure 3.16 shows the profiles for 100 MeV protons and 200 MeV/u carbons at 50 mm depth. Figure 3.17 shows the profiles for 200 MeV protons and 400 MeV/u carbons at 50 mm depth, and Figure 3.18 the profiles for 200 MeV protons and 400 MeV/u carbons at 100 mm depth. For $x > 0$ the beam traveled always through air. For $x < 0$ the beam passes through air or bone or lung (see Figure 2.17).

The deviations between SHIELD-HIT, Geant4 and FLUKA are summarized in Table 3.7. Shown are the maximum obtained differences within $-50 \text{ mm} < x < 50 \text{ mm}$. Differences less than the statistic uncertainty of about 1.5 % are labeled with 's'. SHIELD-HIT differs at maximum 7 % to Geant4 which is observed for 100 MeV protons at 50 mm downstream of lung/air. The disagreement of SHIELD-HIT and FLUKA is at maximum 5 % for 400 MeV/u carbon ions downstream of bone/air at 100 mm depth.

Furthermore, differences in the penumbra are observed. The penumbra is defined in the lateral fall-off region as the distance over which the deposited energy falls from 80 % to 20 % of the plateau value. It is only determined for the lateral fall-off for bone and lung ($x < 0$ in (c), (d), (e) and (f)), because the bins used in the MC codes are only 1 mm. The penumbra for 100 MeV/u carbon beams and any beam for $x > 0$ is not determined.

The differences in the penumbra with SHIELD-HIT and Geant4 or FLUKA are shown in Table 3.8. For protons, the penumbra with SHIELD-HIT is up to 17 % smaller than with the two other codes. For carbon ions, the penumbra of Geant4 is about 15 % larger, whereas for FLUKA it is comparable to SHIELD-HIT. However, there are not enough evaluated points to observe a sufficient conclusion. For proton beams passing through lung, the penumbra decreases with energy and increases with depth. Furthermore, the penumbra for carbon ion beams is smaller than for proton beams, as expected from theory.

Table 3.7: Maximum difference in the profiles in % for Geant4 and FLUKA compared to SHIELD-HIT. The 's' means within statistical uncertainties of 1.5 % and the direction '+' and '-' over- and underestimation of the SHIELD-HIT results.

medium	Proton energy in MeV	profile depth in mm	G/S in %	F/S in %
air	100	50	s	s
	200	50	+3.5	+2.5
	200	100	s	s
lung/air	100	50	+4.0	+4.0
	200	50	-7.0	-3.7
	200	100	+2.0	+2.0
bone/air	100	50	-3.0	s
	200	50	-3.5	s
	200	100	-3.5	s

medium	Carbon energy in MeV/u	profile depth in mm	G/S in %	F/S in %
air	200	50	-1.7	-1.7
	400	50	+1.7	-1.7
	400	100	s	-2.0
lung/air	200	50	s	s
	400	50	+1.7	s
	400	100	s	-2.0
bone/air	200	50	s	s
	400	50	-2.4	-4.0
	400	100	-2.6	-5.0

Table 3.8: Difference in the penumbra determined at the 80% and 20% position of deposited energy for SHIELD-HIT (S) to Geant4 (G) and FLUKA (F). For positive values the penumbra of Geant4 or FLUKA is smaller than with SHIELD-HIT and vice versa.

medium	Proton energy in MeV	profile depth in mm	S-G in mm	S-F in mm
lung	100	50	-3.09	-2.76
	200	50	-0.59	-0.41
	200	100	-0.62	-0.53
bone	200	50	-1.84	-1.47
	200	100	-1.73	-0.82

medium	Carbon energy in MeV/u	profile depth in mm	S-G in mm	S-F in mm
lung	400	50	0.23	-0.05
	400	100	0.23	0
bone	400	50	0.28	-0.08
	400	100	0.18	-0.09

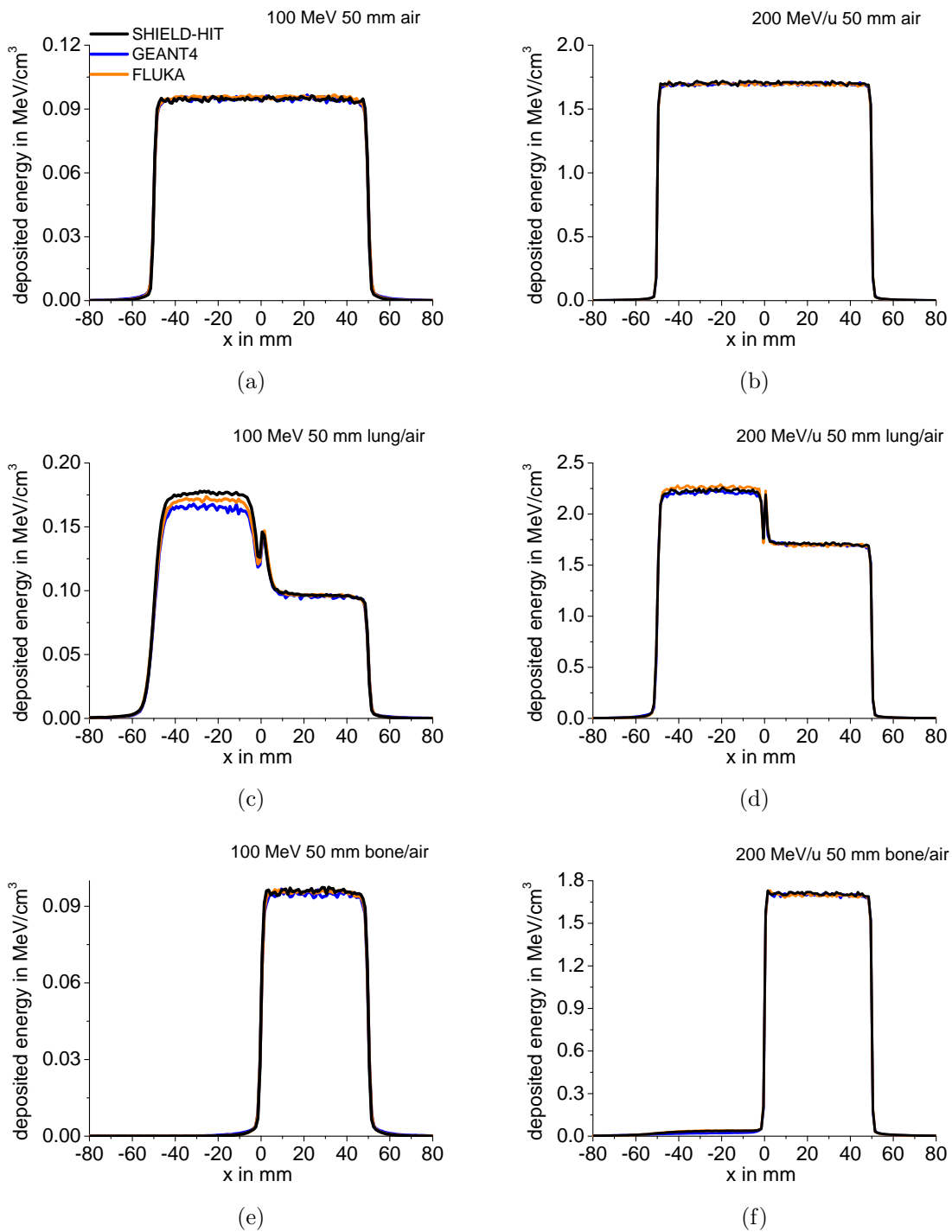


Figure 3.16: Beam profiles at 50 mm depth with SHIELD-HIT (black), Geant4 (blue) and FLUKA (orange) downstream of interfaces from Figure 2.17. On the left for 100 MeV protons and on the right for 200 MeV/u carbon ion beams.

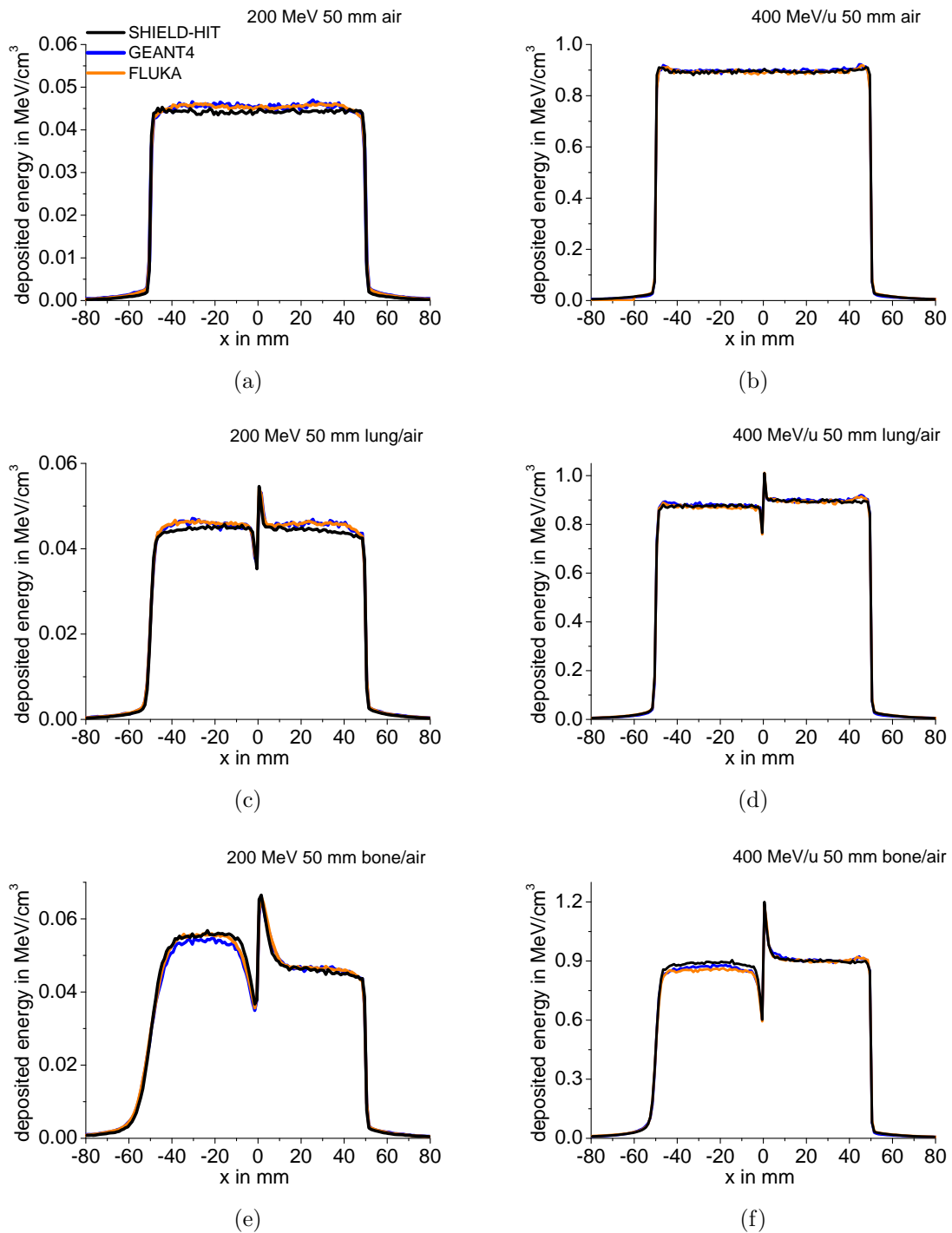


Figure 3.17: Beam profiles at 50 mm depth with SHIELD-HIT (black), Geant4 (blue) and FLUKA (orange) downstream of interfaces from Figure 2.17. On the left for 200 MeV protons and on the right for 400 MeV/u carbon ion beams.

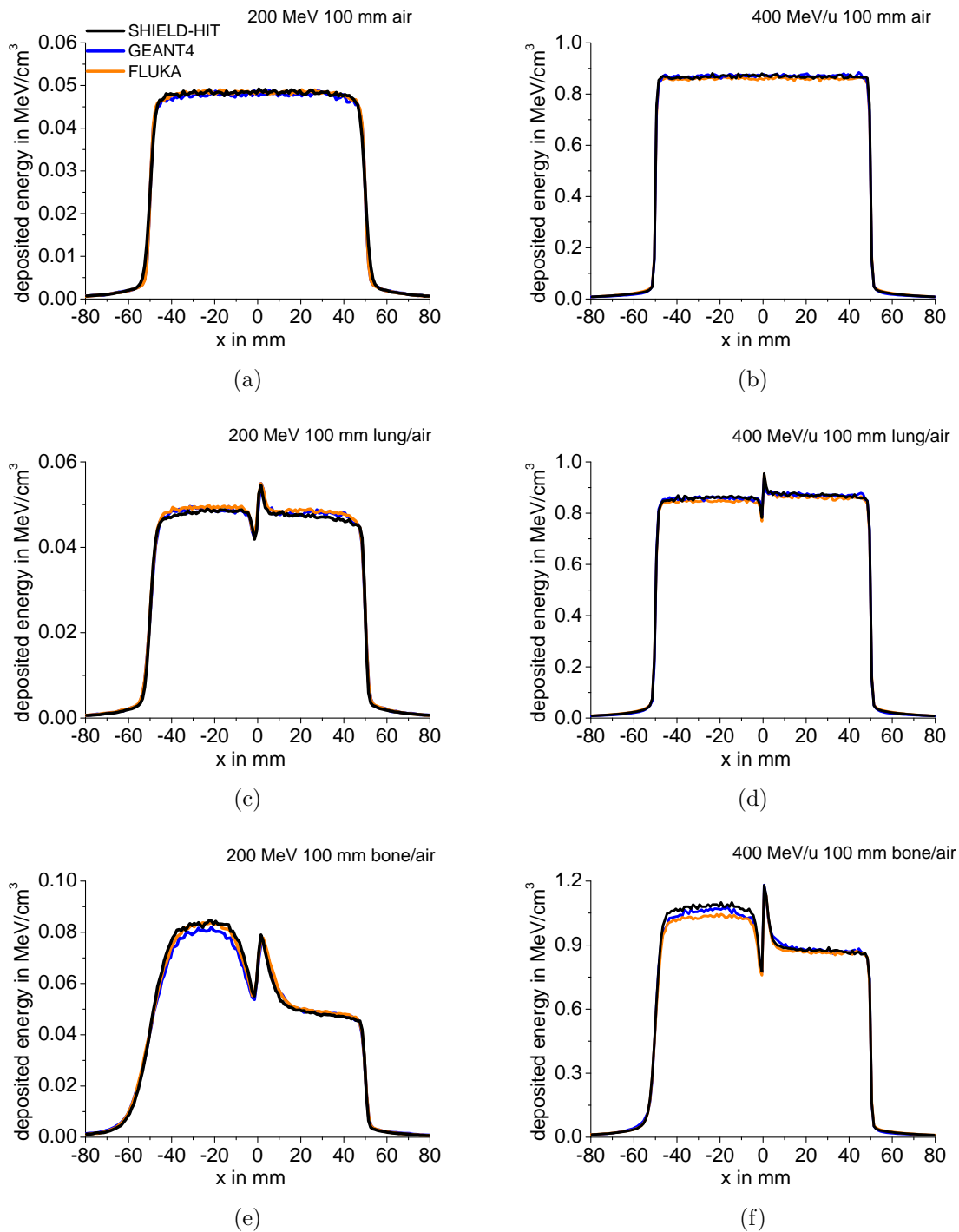


Figure 3.18: Beam profiles at 100 mm depth with SHIELD-HIT (black), Geant4 (blue) and FLUKA (orange) downstream of interfaces from Figure 2.17. On the left for 200 MeV protons and on the right for 400 MeV/u carbon ion beams.

3.9 The Influence of PARLEV(39) on the Fragmentation Process

A variation of the SHIELD-HIT value PARLEV(39) between 1.0 and 0.8 does not influence proton depth-dose curves.

The results for a 270 MeV/u carbon ion beam are shown in Figure 3.19 (a) and (b). In (a) Bragg curves for PARLEV(39)=0.8 and PARLEV(39)=1.0 are shown in red and blue, respectively. PARLEV(39) influences only the height of the Bragg peak and the integral of the dose. The range and depth-dose curves parameters are not influenced.

In (b) the ratio $D_{0.8}/D_{1.0}$ is shown for different generations of particles. The horizontal dash-dotted black line indicates the Bragg peak position at about 144.8 mm. Around the Bragg peak the values from generations >1 show some variations due to the 0.1 mm bins. The ratio $D_{0.8}/D_{1.0}$ for all particles is shown in black.

A reduction of PARLEV(39) to 0.8 decreases the number of inelastic cross sections for carbon. Hence, the ratio $D_{0.8}/D_{1.0}$ in Figure 3.19 (b) is higher for primary carbon ions and lower for secondary particles. The total energy deposition is increased up to 8 % in the peak region. PARLEV(39)=0.8 increases the energy deposition from particles of generation 0 up to 11 % in the Bragg peak and diminishes the influence on the total energy deposition of particles of generations >1 by about 13 %. The ratio of energy deposition from generation 1 particles is not affected in the Bragg peak.

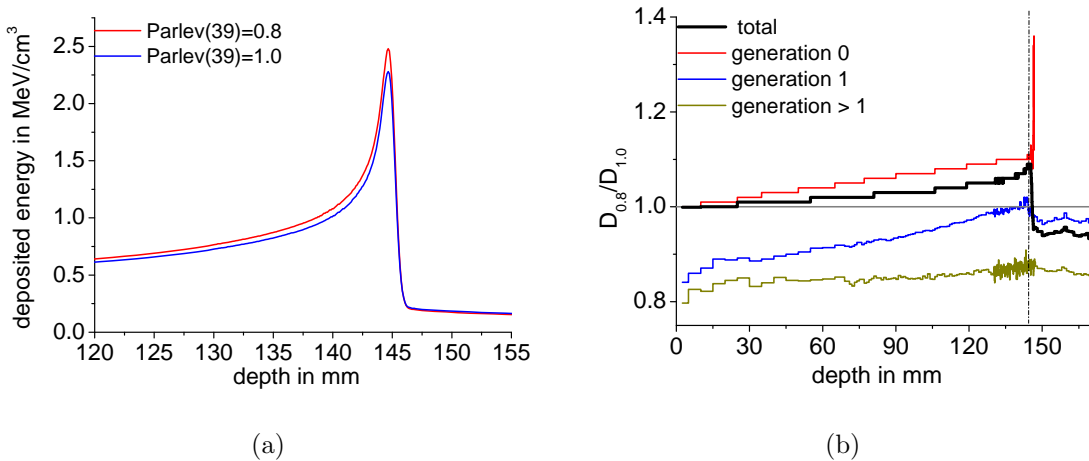


Figure 3.19: Influence of PARLEV(39) on the depth distribution for a 270 MeV/u primary carbon ion beam. PARLEV(39)=0.8 is shown in red and PARLEV(39)=1.0 in blue in (a). The histograms in (b) show the ratio between both PARLEV values depending on the generation of particles.

3.10 Test of the Total Inelastic Cross Section with an MLFC

3.10.1 The MLFC for a 160 MeV Proton Beam

SHIELD-HIT and Geant4 [Paganetti and Gottschalk, 2003] calculated charge distributions are shown together with the measured data in Figure 3.20. The abscissa in (a) and (b) shows absolute values (no normalization), since the total number of incoming protons is known in the experiment and the simulations. The EM peak is shown in a logarithmic scale in (c) and (d) in Figure 3.20 and in Figure 2 in [Henkner et al., 2009b] (appendix G on page XV). Measurement uncertainties are negligible and are discussed in more detail in [Gottschalk et al., 1999].

SHIELD-HIT underestimates the measured values up to channel 47 in mean by 18 % and overestimates them in the peak region by 11 %. In contrast, the calculations with Geant4 in (b) fit very well. Only from channel 42 to 47 and in the peak (channel 51) is an overshoot observed. However, both codes show similar results in the peak region. The semi logarithmic scale in (c) and (d) is used to show that SHIELD-HIT underestimates the build up region by about 45 %, whereas Geant4 fit very well to the measurements. The range is simulated well with both codes. The signal beyond the EM peak is not shown here, because the signal to noise ratio in the measurements is very large and no conclusions can be made.

For SHIELD-HIT the total charge is 15 % less than experimentally observed, which indicates that the total inelastic cross section is too low. However, this has no significant effect on the dose calculations for protons.

As already observed for the Bragg curves, PARLEV(39) has no influence on the simulated charge with protons.

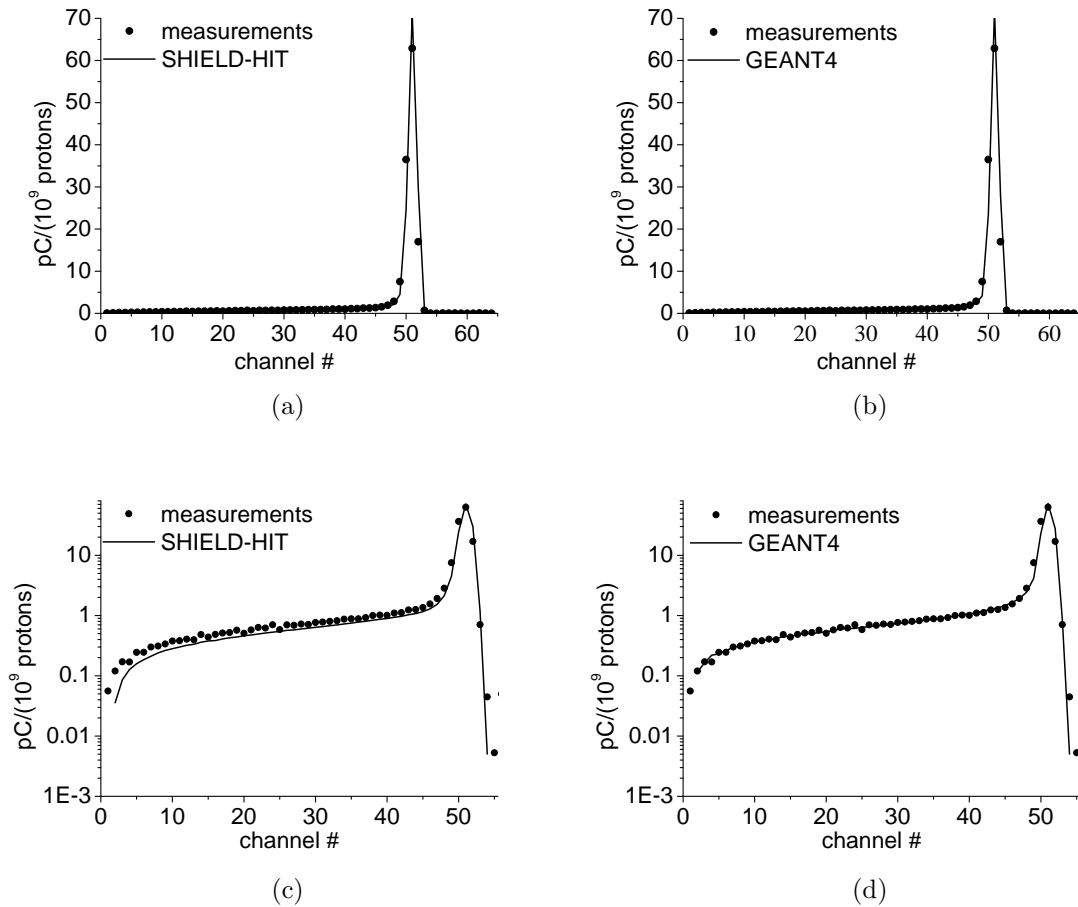


Figure 3.20: Results from calculations and measurements on the MLFC for SHIELD-HIT in (a) and (c), and Geant4 in (b) and (d). The abscissa is in absolute values. The semi logarithmical scale in (c) and (d) is used to show the influence of electromagnetic interactions.

3.10.2 The MLFC for Carbon Ions

The charge distributions for a 270 MeV/u carbon ion beam separated on generation are shown in Figure 3.21 with $\text{PARLEV}(39)=1.0$ and 0.8 in (a) and (b), respectively. The ordinate is shown only up to 60 $pC/(10^9 \text{ carbons})$ to study the influence of charge from fragments to the total charge around 0.

The width of the charge distribution is mainly characterized by particles of generations >0 . Particles from generation 1 are present right from the beam entrance, whereas the charge from particles from generations >2 increase toward the peak and have no significant influence in the Bragg peak.

The difference of the simulated charge with $\text{PARLEV}(39)=0.8$ ($C_{0.8}$) and 1.0 ($C_{1.0}$) is shown in Figure 3.22. Only within the peak region is an influence of $\text{PARLEV}(39)$ on the total charge (black) observed. Here, the maximum total charge is 10 % higher with $\text{PARLEV}(39)=0.8$ than compared to calculations with $\text{PARLEV}(39)=1.0$.

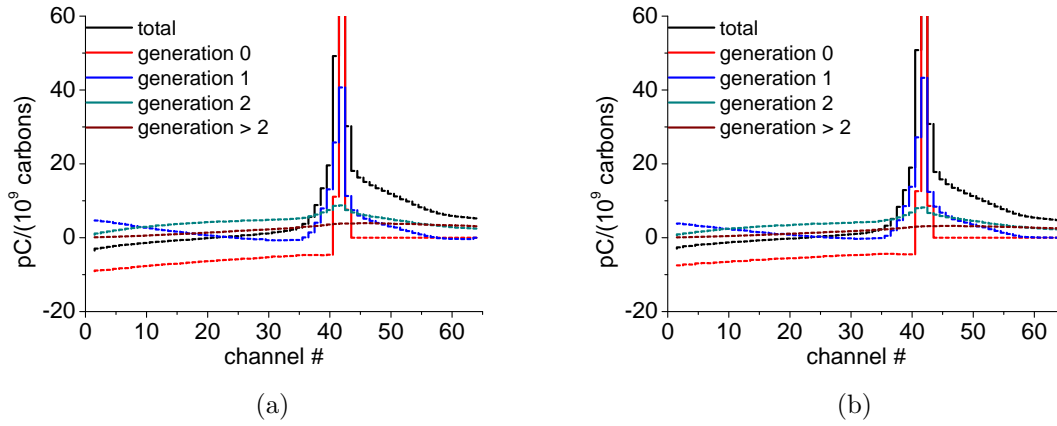


Figure 3.21: Shown are the charge distributions of particles of different generation against channel number. For a 270 MeV/u primary carbon ion beam PARLEV(39) is set to 1.0 and 0.8 in (a) and (b), respectively. The ordinate is shown up to 60 pC/(10^9 ^{12}C).

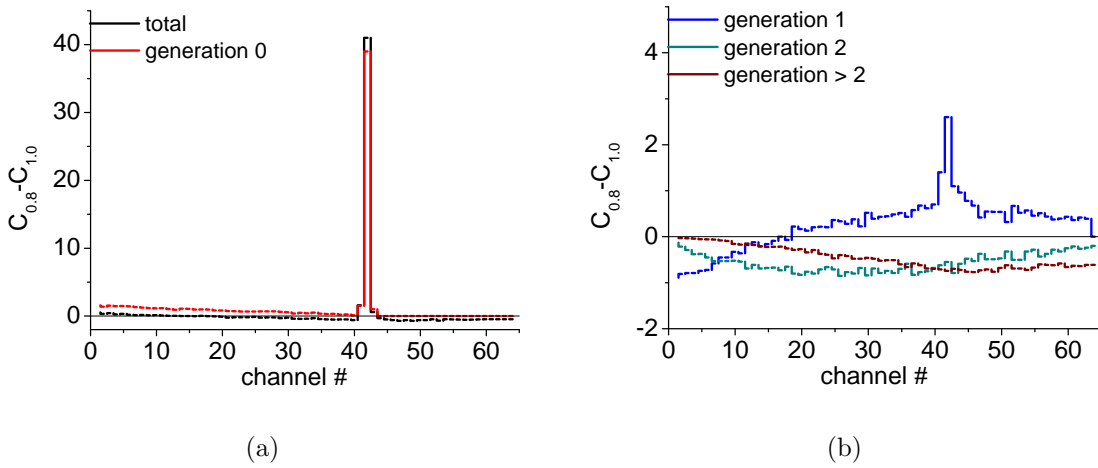


Figure 3.22: The difference of the charge for a 270 MeV/u primary carbon ion beam with PARLEV(39)=0.8 and 1.0. The charge from all particles and primary carbon ions in (a) and from different generations in (b).

3.11 Distributions of Fragments in a Carbon Ion Beam

In this chapter measured differential cross sections and depth distributions available from [Haettner, 2006] are compared to simulations with SHIELD-HIT. Several parameters are varied influencing the SHIELD-HIT results. They are summarized in Table 3.9. The set specific color is later used to show the results achieved with this setup in Figures 3.23 to 3.29.

Set A is used as a reference setup, since the previous work showed that PARLEV(39)=0.8 better agrees with measured depth-dose curves. $\Delta E/E$ and FWHM are taken from [Haettner, 2006] and PARLEV (34) and (33) are kept 1.0 as default.

The impact of PARLEV(39) on the differential cross sections for carbon ions and fragments is studied in set B. Variations in the beam spread ($\Delta E/E$ and FWHM) on the

differential cross section are studied in set C. PARLEV(34) and PARLEV(33) in set D are adjusted to improve the differential cross sections of the fragments derived from set A.

Table 3.9: SHIELD-HIT setup to simulate angular distributions. One setup belongs to one color, which is afterwards used in Figures 3.23 to 3.29. The I-value for water is always set to 80.8 eV.

set number and color	PARLEV(39)	PARLEV(34)	PARLEV(33)	ΔE	FWHM
A	0.8	1.0	1.0	0.5 %	5 mm
B	1.0	1.0	1.0	0.5 %	5 mm
C	0.8	1.0	1.0	0.0	0
D	0.8	17	0.3	0.5 %	5 mm

In Figure 3.23 (a) the measured ionization curve in depth together with the depth-dose curve from SHIELD-HIT is illustrated. The Bragg peak in the experiment is at 275 mm water depth and is shifted about 1.4 % toward lower depth for SHIELD-HIT. The position of the 80 % dose is shifted only 0.6 % toward lower depth for SHIELD-HIT. The peak height from calculations is 32 % lower than in the experiment.

In Figure 3.23 (b) the number of carbon ions per incident number of particles are shown against water depth. The depth distribution is obtained by an integration of the number of particles within 0° to 10° . SHIELD-HIT is in good agreement to the experiment up to 260 mm water depth. The difference at $y=0.184$ in (b), which is interpolated for the experiment, is 6.4 mm.

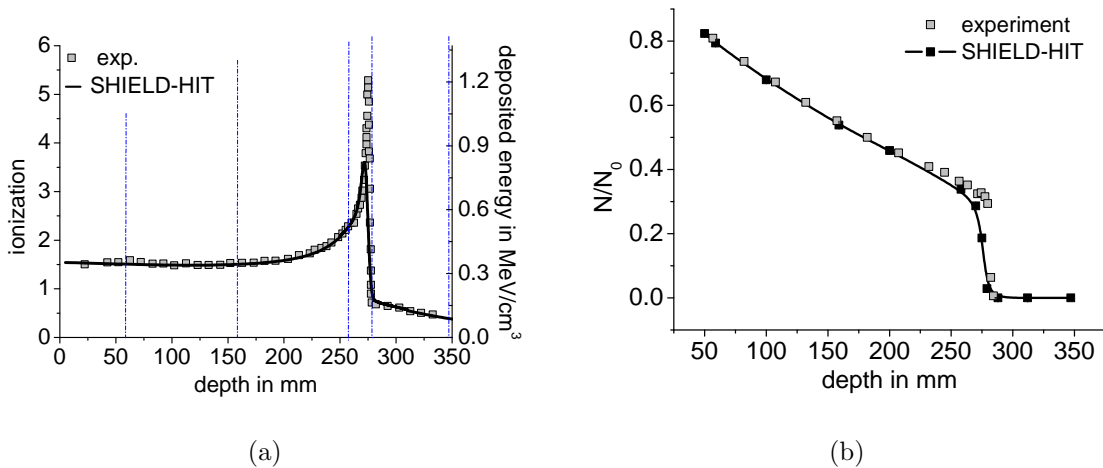


Figure 3.23: Depth distributions derived from the measurements and calculations are shown in (a). The dash-dotted lines in blue show the positions (59, 159, 258, 279 and 347 mm) where the angular distributions of the fragments are obtained. The number of carbon ions normalized to the number of incident particles against water depth is shown in (b).

The differential cross sections for carbon ions are shown in Figure 3.24 at 159 mm and 258 mm water depth in (a) and (b). PARLEV(39)=1.0 in set B does not sufficiently

reproduce the measured amount of carbon ions and underestimates them about 13 % at 0° . SHIELD-HIT calculations with set A agree very well to the measurements. The influence of PARLEV(34) and (33) in set D do not considerable influence the calculated differential cross section of carbon ions.

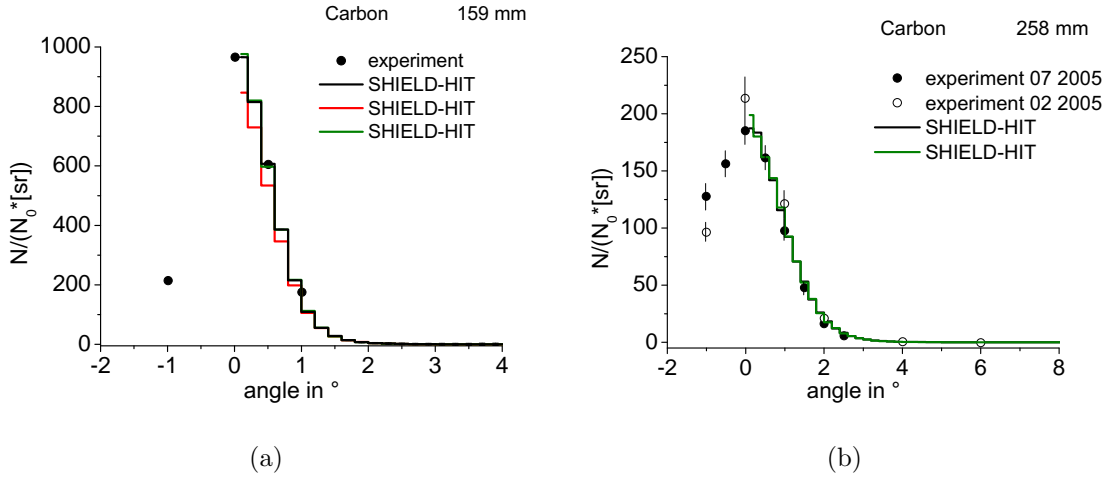


Figure 3.24: Angular distributions of carbon ions simulated with SHIELD-HIT (straight) and measured (dots) for water depth of 159 mm and 258 mm. The colors refer to the parameters given in Table 3.9.

Measured and calculated angular and depth distributions of hydrogen up to boron fragments are shown in Figure 3.25 to 3.29. In (a) to (d) the number of fragments, normalized to the number of incident particles and solid angle is shown against the angle from the central beam axes. The depth distributions in (e) show the number of fragments integrated from 0° to 10° , normalized to the number of incident particles against depth in water.

The influence of PARLEV(39)=1.0 (set B) and the beam spread (set C) on the differential cross sections are shown in Figures 3.25 to 3.29 (a) and (c) together with results from set A. PARLEV(39) and the beam spread do not greatly influence the fragment distributions. Especially for the depth distributions in (e) the influence of PARLEV(39), shown as red squares, is negligible.

The differential cross section in set A for the number of hydrogen fragments is greatly underestimated with SHIELD-HIT. It differs up to 53 % and 20 % for the 59 mm and 347 mm thick water tank from the measurements. The helium distribution is within 2 % of the experiment for all thicknesses. Lithium is overestimated up to 60 %. Beryllium and boron fragments are on average overestimated by about 120 % and 80 %. The relative deviation in percentage varies strongly with angle and water thickness, as shown in the appendix in Table C.1. This table gives a more detailed summary of the deviations of the differential cross sections in Figures (a) to (d). The deviations from depth distributions in the Figures (e) are summarized in Table 3.11.

A considerable improvement of the differential cross sections is observed in set D, where PARLEV(34) and PARLEV(33) are varied. Set D gives the best values for these parameters of 17 and 0.3, respectively. The influence on the differential cross sections is shown for single fragments downstream of a 159 mm thick water target in Figures 3.25 to

3.29 (b) and integrated from 0° to 10° for various water depth in (e). The improvement of the differential cross sections with set D compared to set A at 159 mm water depth is shown in Table 3.10. The largest improvement is obtained for H, Li and Be while for He and B no considerable improvement in the differential cross sections is achieved.

Table 3.10: Deviations between SHIELD-HIT and the experiment at about 0° and 2° for set A and D ($\pm 3\%$).

fragment type	water thickness	deviation at $0^\circ / 2^\circ$ for set A in %	deviation at $0^\circ / 2^\circ$ for set D in %
H	159 mm	-26 / -22	-10 / -6
He	159 mm	11 / -10	20 / 11
Li	159 mm	35 / 38	2 / 2
Be	159 mm	228 / 153	148 / 65
B	159 mm	84 / 2	84 / 2

Table 3.11 shows the deviations between calculations with set A and D to the measurements illustrated in Figures 3.25 to 3.29 (e). Whereas for Li an improvement in set D is only observed for large water tanks, cross sections for H and Be are improved for any water thickness. The depth distribution for boron is almost not affected by PARLEV(34) and (33).

No conclusion on the depth distributions can be made for He, because an inconsistency of the experimental depth data in (e) is observed. Comparing the differential cross section and depth distributions for He with set A, there is a disagreement. Whereas the differential cross sections fit very well to the experiment, the depth distribution does not. For hydrogen, a disagreement of the experiment with calculations with set D is observed as well. Whereas SHIELD-HIT still underestimates the differential cross sections, it overestimates the number of fragments in (e).

Table 3.11: Deviations of calculated to measured differential cross sections for various water thicknesses for set A and D (± 3 %).

fragment type	water thickness	deviation for set A in %	deviation for set D in %
H	59 mm	-17	2
	159 mm	-10	9
	258 mm	-12	5
	279 mm	-11	6
	288 mm	-7	11
	347 mm	-6	9
He	59 mm	-28	-19
	159 mm	-25	-16
	258 mm	-24	-15
	279 mm	-23	-14
	288 mm	-20	-11
	347 mm	-24	-17
Li	59 mm	13	-28
	159 mm	39	-13
	258 mm	40	-14
	279 mm	47	-10
	288 mm	54	-5
	347 mm	49	-10
Be	59 mm	109	27
	159 mm	147	54
	258 mm	124	35
	279 mm	130	43
	288 mm	116	39
	347 mm	114	54
B	59 mm	14	13
	159 mm	32	28
	258 mm	15	12
	279 mm	27	25
	288 mm	47	47
	347 mm	211	212

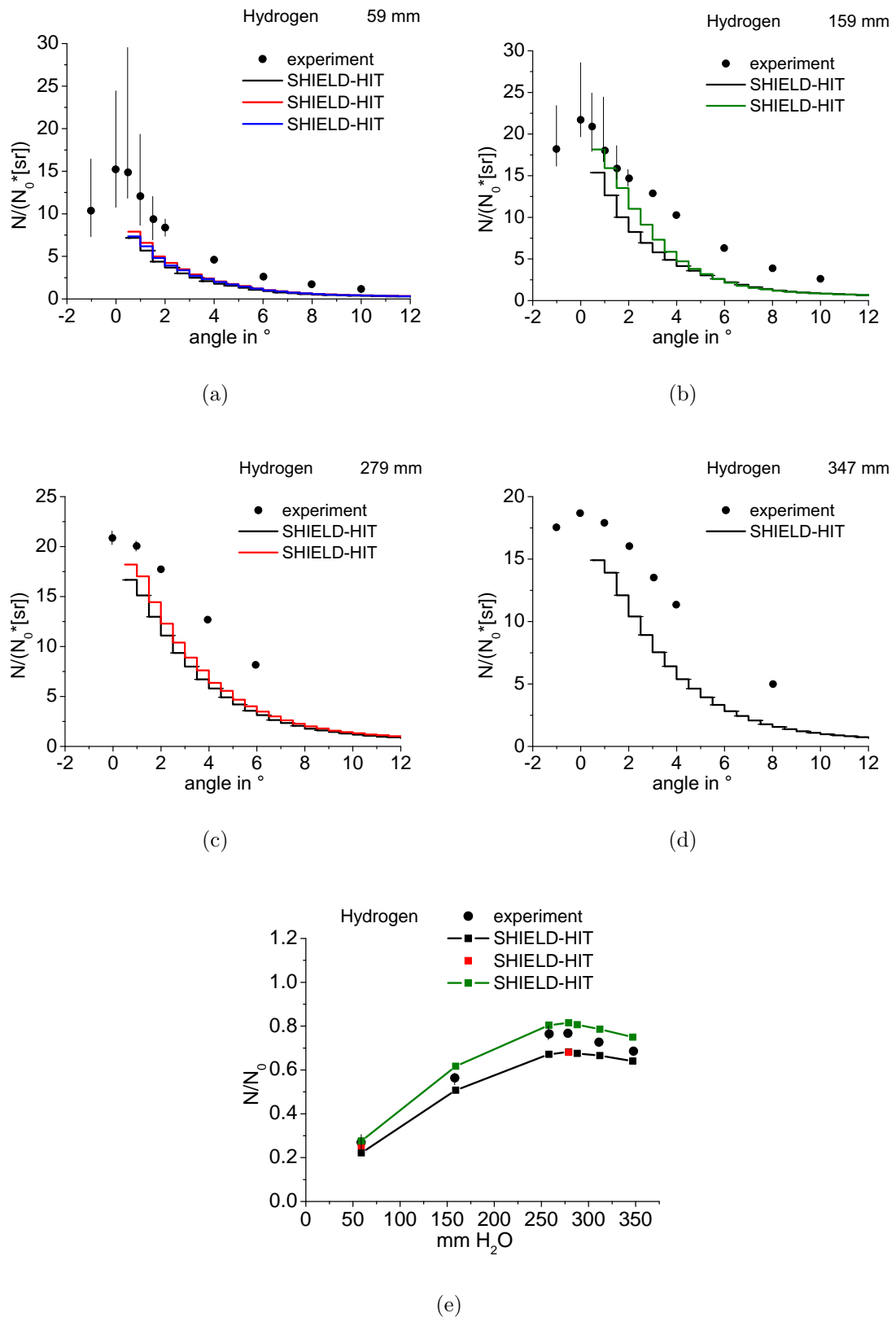


Figure 3.25: In (a) to (d) the differential cross sections of hydrogen fragments are demonstrated. The abscissa shows number of hydrogen fragments N normalized to the number of incident particles N_0 per solid angle sr. In (e) the number of fragments, integrated between 0° - 10° , are shown against water depth. The colors refer to the parameters given in Table 3.9.

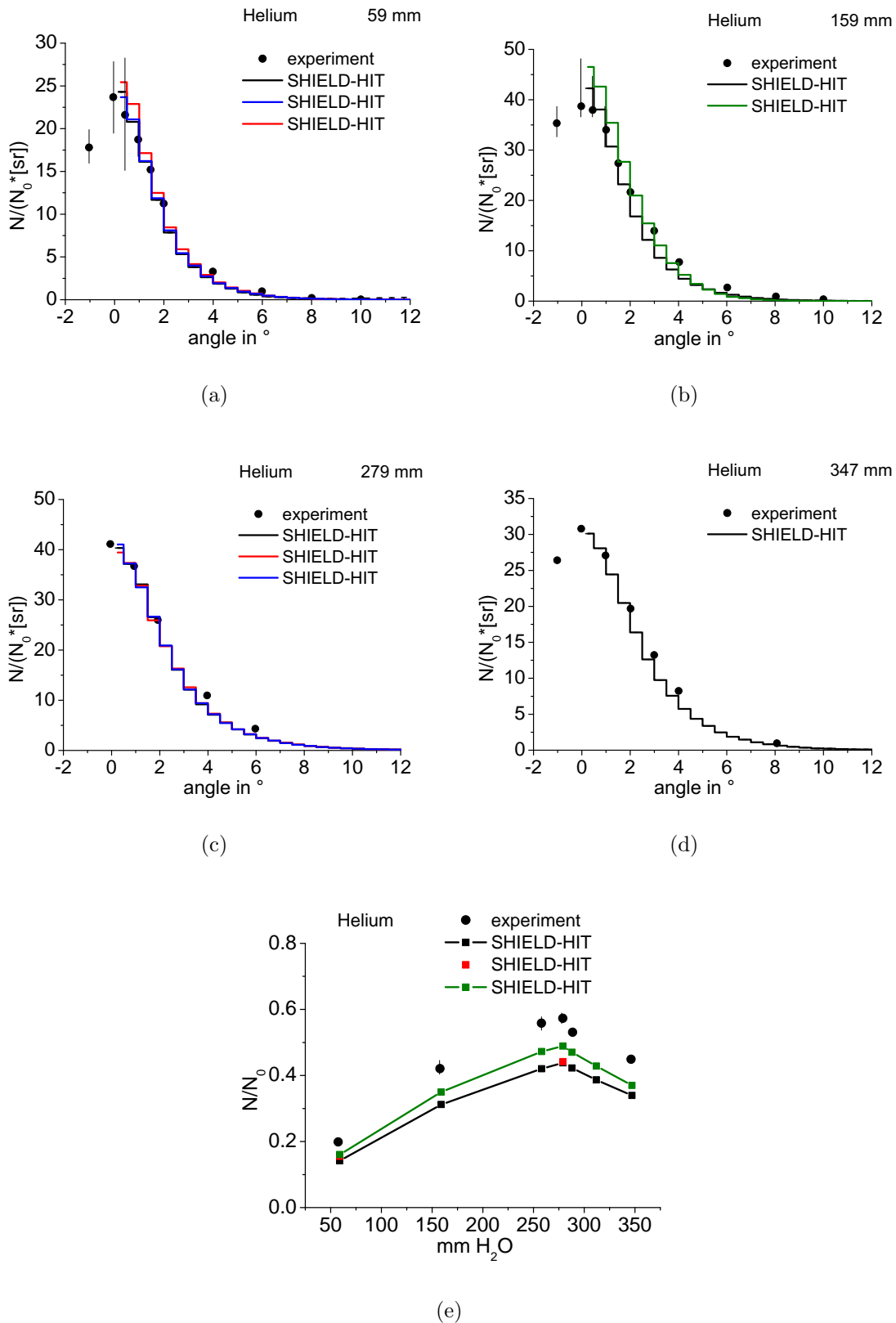


Figure 3.26: In (a) to (d) the differential cross sections of helium fragments are demonstrated. The abscissa shows number of helium fragments N normalized to the number of incident particles N_0 per solid angle sr. In (e) the number of fragments, integrated between $0^\circ - 10^\circ$, are shown against water depth. The colors refer to the parameters given in Table 3.9.

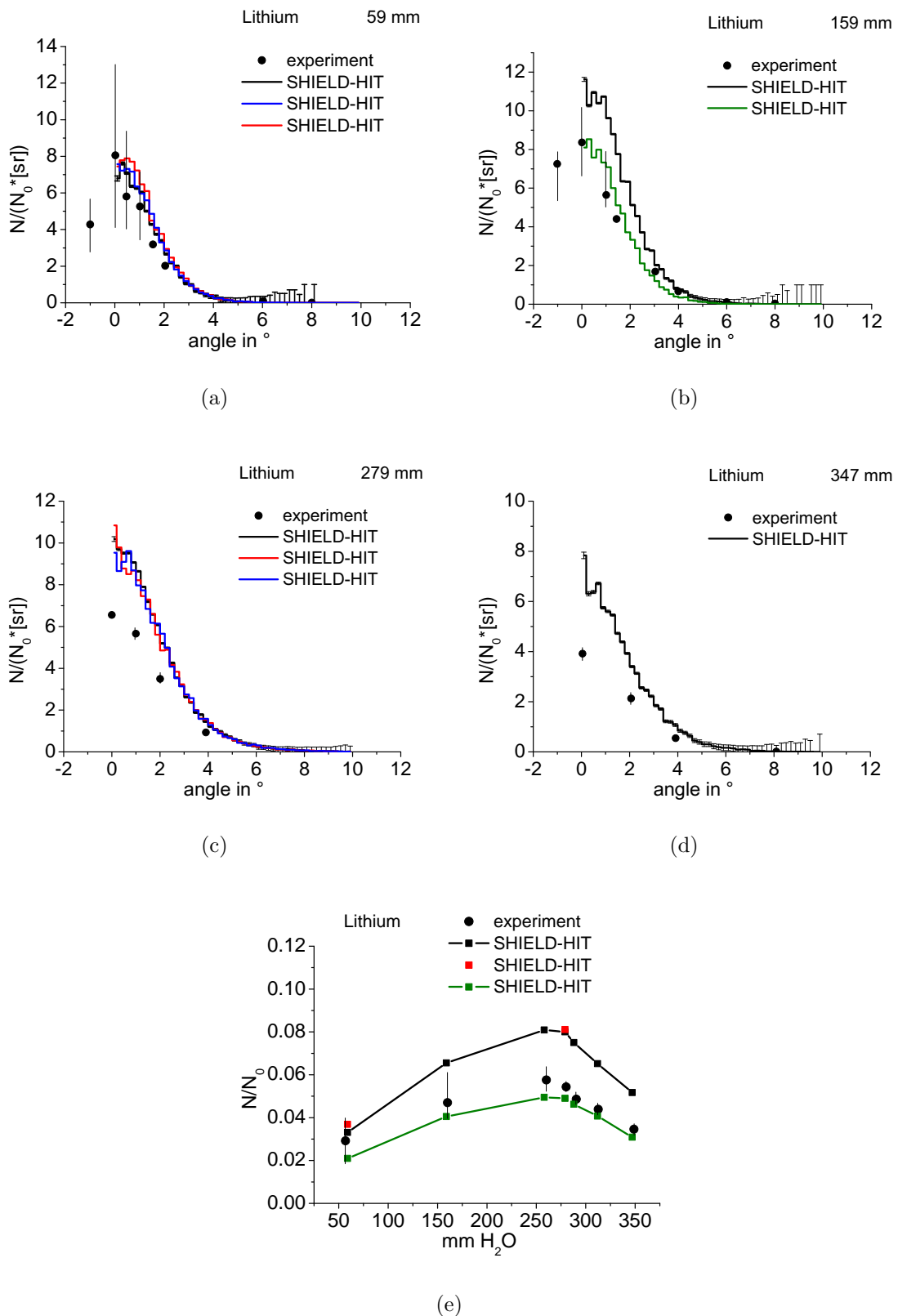


Figure 3.27: In (a) to (d) the differential cross sections of lithium fragments are demonstrated. The abscissa shows number of lithium fragments N normalized to the number of incident particles N_0 per solid angle sr. In (e) the number of fragments, integrated between $0^\circ - 10^\circ$, are shown against water depth. The colors refer to the parameters given in Table 3.9.

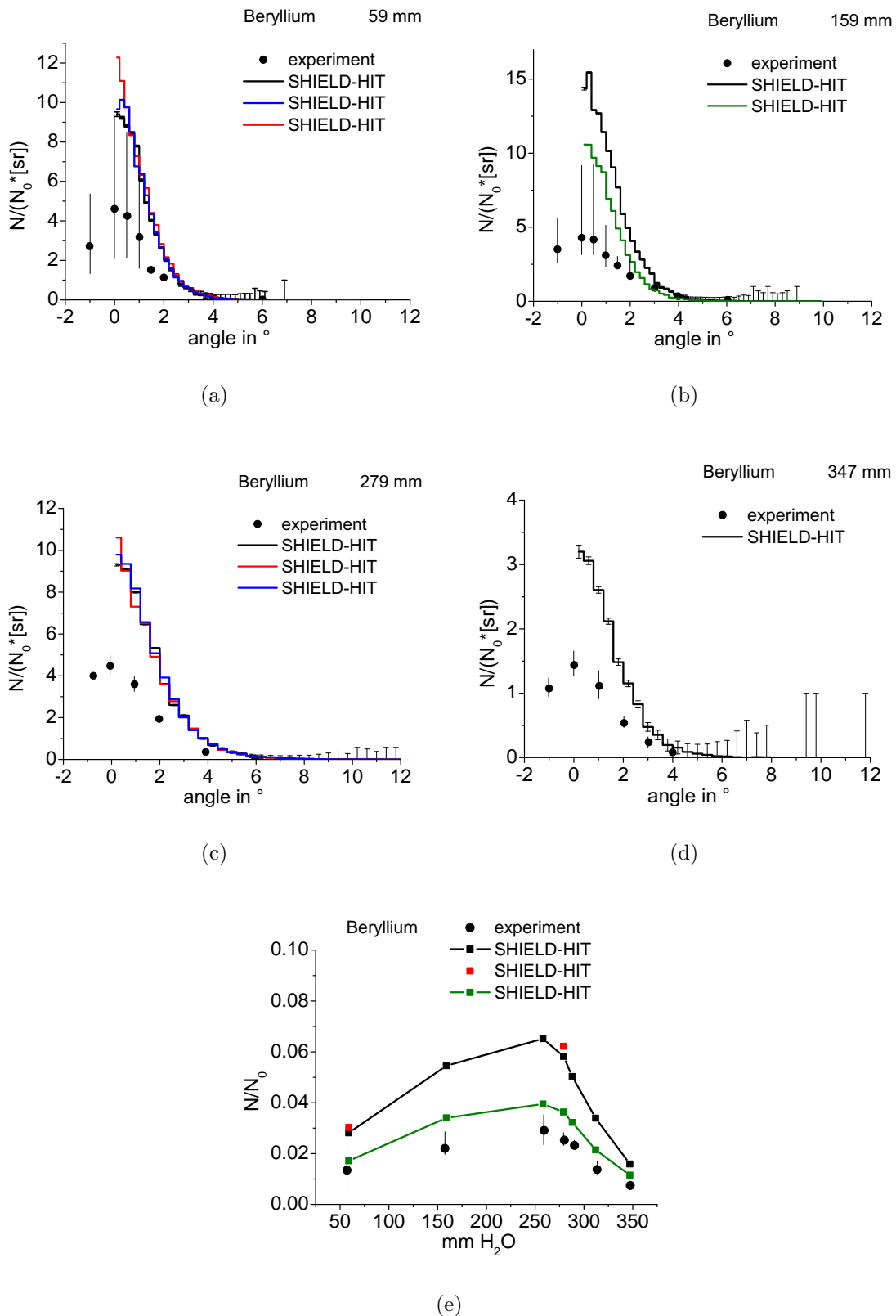


Figure 3.28: In (a) to (d) the differential cross sections of beryllium fragments are demonstrated. The abscissa shows number of beryllium fragments N normalized to the number of incident particles N_0 per solid angle sr. In (e) the number of fragments, integrated between $0^\circ - 10^\circ$, are shown against water depth. The colors refer to the parameters given in Table 3.9.

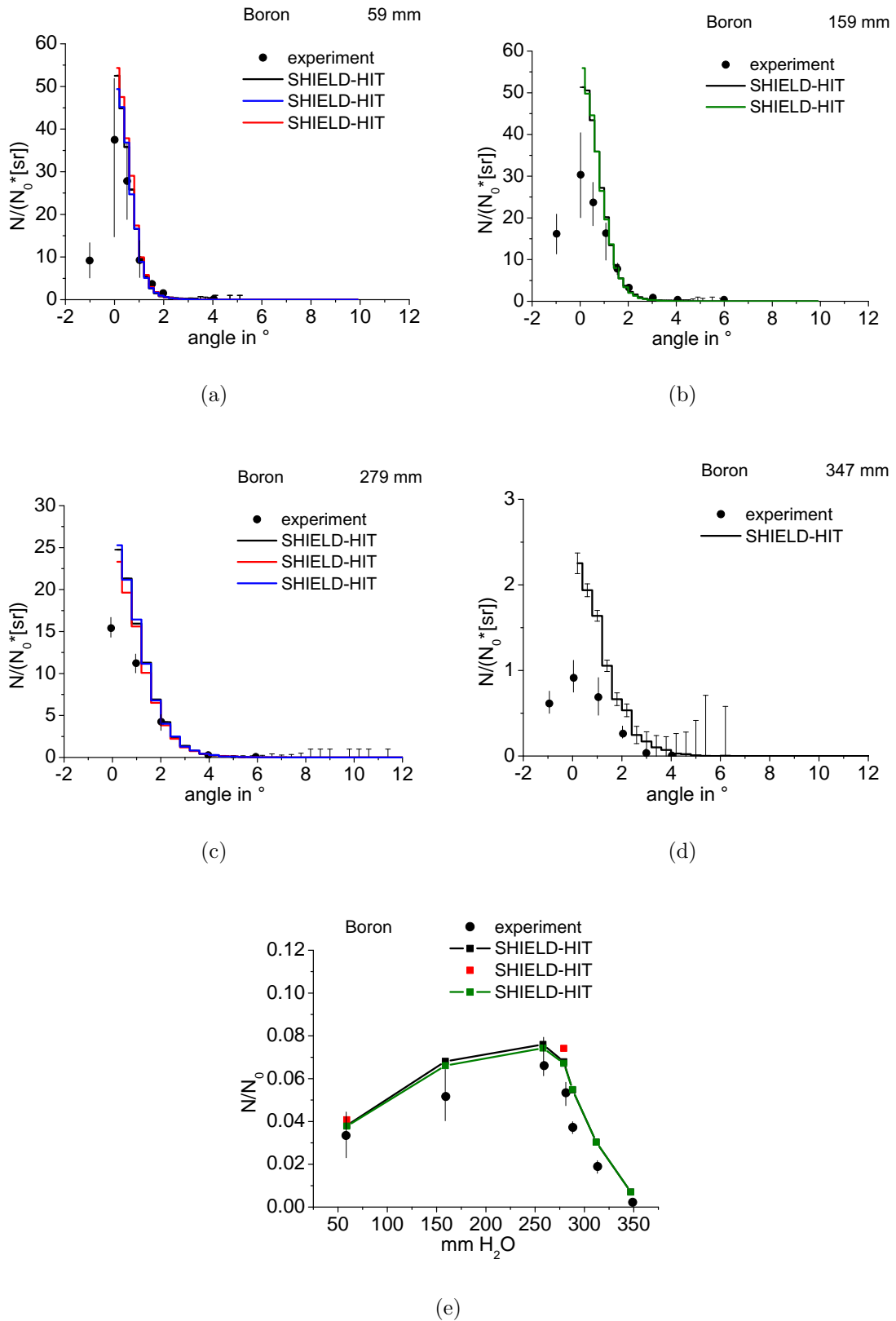


Figure 3.29: In (a) to (d) the differential cross sections of boron fragments are demonstrated. The abscissa shows number of boron fragments N normalized to the number of incident particles N_0 per solid angle sr . In (e) the number of fragments, integrated between $0^\circ - 10^\circ$, are shown against water depth. The colors refer to the parameters given in Table 3.9.

3.12 Neutron Equivalent Dose from Carbon Ion Treatment

Preliminary results of neutron equivalent doses in 2.32 in comparison to protons are shown in Figure 3.30 and 3.31 for a phantom of an eleven year old male patient irradiated in the brain with a cylindrical target volume of 60 mm diameter and an SOBP of 100 mm range and 50 mm modulation width. The relative equivalent neutron dose is given in mSv per treatment Gy for several organs. Relative neutron doses for protons shown here are taken from [Jarlskog and Paganetti, 2008a] and are only calculated from neutrons produced inside the patient, which is similar to an ideal proton beam scanning without neutrons produced outside.

The neutron dose from scanned carbon ion therapy in peripheral organs are three orders of magnitude smaller for this calculated case than compared to doses from proton therapy. As a preliminary result for this case, the neutron equivalent dose rapidly decreases with increasing distance to the target volume.

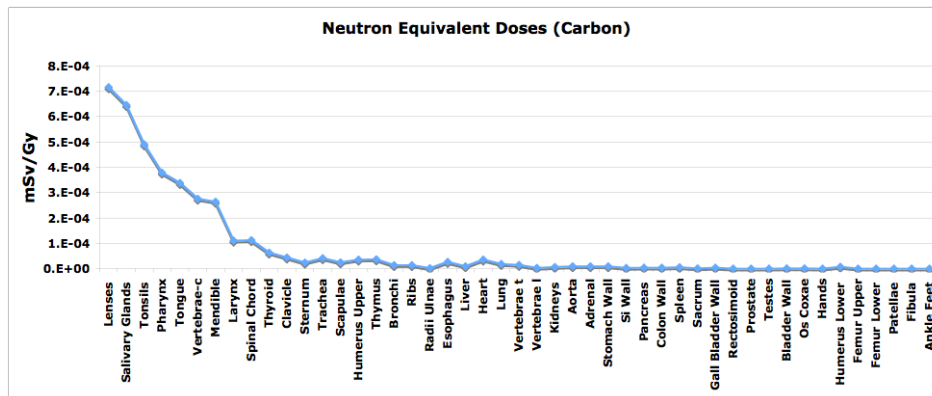


Figure 3.30: Geant4 simulated neutron equivalent doses from initial carbon beams for several organs of an eleven year old male phantom irradiated in the brain.

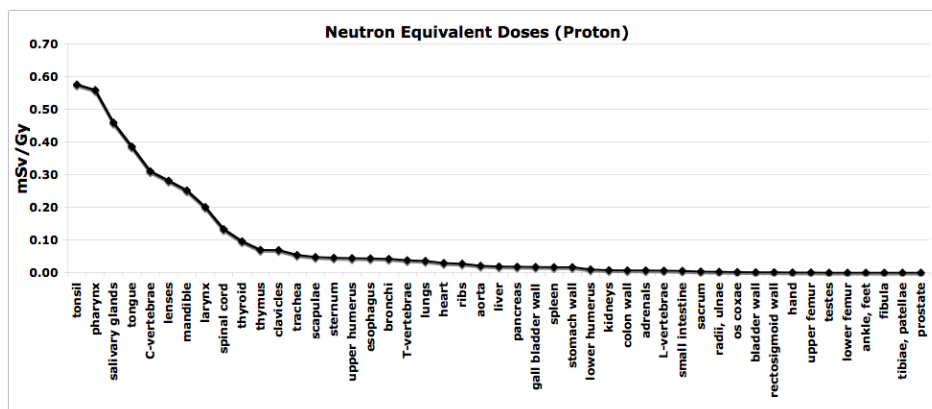


Figure 3.31: Geant4 simulated neutron equivalent doses from proton beams for several organs of an eleven year old male phantom irradiated in the brain. The neutron equivalent dose shown here is only from neutrons produced inside the patient.

4 Discussion

4.1 Monte Carlo Simulations for Dosimetry

4.1.1 The I-Value for Water and other Media

SHIELD-HIT requires a mean I-value of 80.7 ± 2.3 eV to correctly calculate the measured, not yet published, Bragg peak positions in water available from [Schardt et al., 2008] in 3.1. Calculating depth-dose curves from ICRU data with SHIELD-HIT will underestimate the measured range by about 3.3 mm.

In treatment planning, the calculation of a smaller range would increase the primary beam energy which results in an over dosage at the tissue downstream of the tumor and an under dosage at the proximal part of the tumor for an SOBP. Treatment with such an SOBP can cause severe side effects in healthy tissue and probably will not kill all tumor cells. To avoid range uncertainties due to inconsistencies in stopping power and I-value data for water it is suggested to use Bethe-Bloch calculated stopping power data and an I-value which is adjusted to measured ranges in water.

The best fit I-value decreases slightly with increasing primary beam energy in Figure 3.1. This may be due to the evaluation of I_w at the Bragg peak and not at the range defined at the 80 % dose position distal of the peak, which were not available from [Schardt et al., 2008]. The energy dependence of the I-value should be studied again, when the measured depth-dose curves are published.

Near completion of this thesis an addendum² to ICRU73 from 2005 was made and will be published. This addendum contains new stopping power data for particles with $Z > 2$ and recommends an I-value of 78 eV for water. For H and He the stopping power data in ICRU49 remain unchanged. Hence, the stopping power data are still inconsistent as compared to Bethe-Bloch calculated stopping power with a fixed I-value.

The value of 78 eV, however, still differs from the recently published value of 80.8 eV in [Paul et al., 2007] and the value of 80.7 ± 2.3 eV as determined in 3.1, but is within the standard deviation of 2.3 eV with SHIELD-HIT. Further investigations are needed to clarify the differences in I_w between SHIELD-HIT and ICRU.

A comparison of old and new stopping powers and range calculations in water is shown in Figure 4.1. The ratio of the stopping power for Li up to C is shown in Figure 4.1 (a). The new stopping power data for particles with $Z > 2$ is about 1.7 % lower than the old data from 2005 over the whole energy range. This increases the range of SHIELD-HIT by about 2.7 mm in Figure 4.1 (b) (about 0.24 mm per 1 eV, as already reported in 2.1.2). For energies smaller than 2 MeV the new stopping power is significantly smaller, but will increase the Bragg peak position only by about 0.04 mm which is negligible.

As reported in [Paul et al., 2007], the stopping power data for air in ICRU49 and 73 is inconsistent as well. Whereas in ICRU73 I_{air} is 82.8 eV, it is 85.7 eV in ICRU49, and suggested to be 88.8 eV in [Paul et al., 2007]. The range of particles in air is probably

²private communication

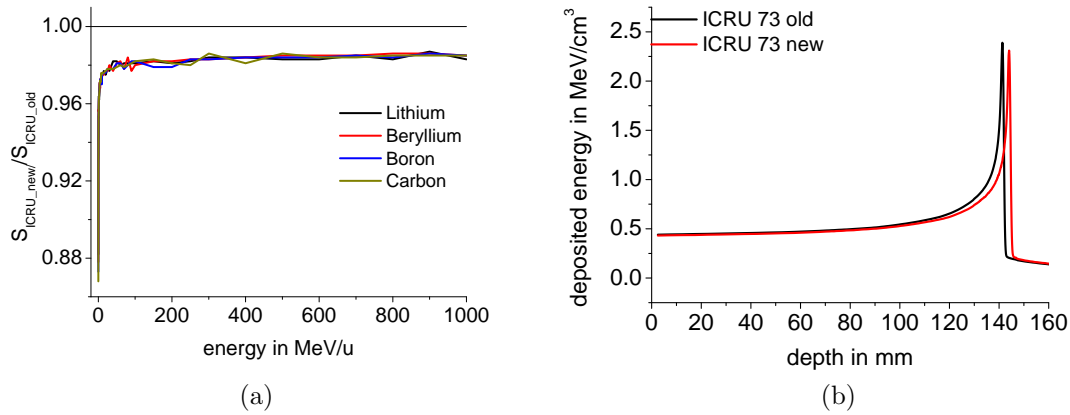


Figure 4.1: Comparison of old and new ICRU73 stopping power data. The ratio of new and old ICRU73 stopping power data is shown in (a) and the resulting depth distributions for a 270 MeV/u carbon ion beam in (b).

not significantly impacted from this inconsistency, since the energy loss is very small in air. However this further indicates that the stopping power data for all other media published in ICRU49 and 73 may be inconsistent as well and need to be further studied.

The inaccuracy in SHIELD-HIT calculated ranges in 3.2 due to I-value errors is only relevant for adipose tissue and should be considered for patients with significant body fat. The uncertainties in titanium will have no effect, since the medium produces artifacts in the CT data which will result in range uncertainties exceeding the uncertainties from the I-value [Jäkel and Reiss, 2007]. For cortical bone the effects of range uncertainties will be smaller than in the investigated case, since the fraction of cortical bone is small compared to other media. Furthermore, range uncertainties in bone or titanium are only relevant for treatments of tumors in the pelvic region, when the beam travels through the hips. For water the inaccuracy of range simulations due to I-value uncertainties can be avoided as discussed above by adjusting the MC range to measurements.

Furthermore, the Bragg additivity rule, eq. 2.9 used in [ICRU49, 1993] is only an approximation and averages over the whole molecule. [Kempe and Brahme, 2008] describe a different way to determine the average charge to mass ratio Z/A which improves the range calculations for lithium and carbon ion beams from their analytical model. Deviation of up to 3 % from ranges calculated with the Bragg rule are reported there. Whether an implementation of their formula for the average charge to mass ratio in SHIELD-HIT improves stopping power calculations should be determined in a comparison to other stopping power data in future work.

Moreover, the I-values for the elements in ICRU49 and the mean I for compounds in ICRU37 are given with uncertainties. This offers an additional possibility to study the agreement of mean I-values given there toward mean I-values calculated with the Bragg additivity rule. However, the expected influence on depth-dose curves is small in that case, but may further decrease the accuracy of range calculations with MC.

4.1.2 The Water-to-Air Stopping Power Ratio

The $S_{w/air}$ depends significant on the I-value for water in 3.3. If an I_w of 80.8 eV, [Paul et al., 2007], is used for carbon ions and protons, the constant $S_{w/air}$ of 1.13 in

IAEA TRS-398 is underestimated by about 1 %. Therefore, following eq. 2.20, the beam quality correction factor k_Q would be overestimated by about 1 %. Hence, the calculated absorbed dose to water from an ionization chamber will result in an under dosage in ion beam therapy, when using the IAEA recommendation. This should be taken into account in the clinical application of carbon and proton ion beams.

The stopping power ratio for carbon and proton beams increases by about 0.2 % from the beam entrance toward the Bragg peak in Figure 3.2, hence a practical method to correct for this effect should be considered if a precision beyond that value is aimed for. A method could be a parametrization of the correction as a function of the modulation depth and range.

In the last 1 mm toward the end of the particle range, the stopping power ratio increases by up to 2.5 % for 50 MeV protons and up to 6 % for 50 MeV/u carbon particles in Figure 3.4. This effect is restricted to a very narrow region and will thus only be relevant for plane-parallel ionization chambers at low energies.

The $S_{w/air}$ for 140 MeV protons calculated with ICRU data shows a local maximum at about 122 mm depth in set 3 in Figure 3.2, whereas with Bethe-Bloch in set 4 it shows a monotonic behavior. It is about 10 mm upstream of the expected increase of the $S_{w/air}$. The local maximum is probably due to the usage of ICRU stopping power data and SHIELD-HIT calculated particle fluences. A more detailed analysis is needed here to exclude variations within ICRU data or SHIELD-HIT calculations.

Furthermore, a shift of about 0.02 MeV of the stopping power maximum toward lower energies for the ICRU data is determined, but influences the range only by 0.3 μm and does not explain the maximum in $S_{w/air}$ at 122 mm depth. However, ICRU and SHIELD-HIT stopping power data should be compared to data from SRIM [SRIM-2008, 2008] or MSTAR [Paul and Schinner, 2002], where a first analysis showed that their stopping power maxima are amongst ICRU and SHIELD-HIT. Whether the effect of the I-value approximation with the Bragg additivity rule in SHIELD-HIT is responsible for the different stopping power maximum is unclear.

The I-value of air has an effect on the water-to-air stopping power ratio as well (Figure 3.2 an [Henkner et al., 2009a], appendix G on page XXV). An increase of I_{air} can cancel out the effect of a decrease of the $S_{w/air}$ with increasing I_w . A further study of the influence of I_{air} on the $S_{w/air}$ is needed as well as a revision of the stopping power data for air.

The $S_{w/air}$ for a homogeneous physical SOBP from carbon ions is shown in Figure 6 on page 1234 in [Henkner et al., 2009a]. The $S_{w/air}$ increases toward the distal end of the plateau. However, for a treatment with carbon ions the dose is optimized to a homogeneous biological dose plateau. The physical dose would decrease toward the end of the SOBP, because the RBE for carbon ion beams increases with depth (see Figure 2.11). The actual $S_{w/air}$ for a homogeneous biological SOBP from carbon ions needs to be studied in future work. The RBE for protons is mainly constant over the whole depth and an increase in the $S_{w/air}$ will be relevant. However, the $S_{w/air}$ within an SOBP will depend on the modulation width. For dosimetry the $S_{w/air}$ should be determined for a reference SOBP and a reference position of the measuring chamber.

4.1.3 Lateral Water Tank Length

Whereas for photons the required side length of a water tank should be at least 150 mm for a 100 x 100 mm² field size, the calculations in 3.4 show no major differences between

side length of 200 mm and 120 mm. This is due to the small lateral scattering of ion beams and the negligible effect of backscattering. The variations shown in Figure 3.5 and 3.6 are from numerical variations in SHIELD-HIT and can probably be reduced by an increase of the number of primary particles, which will increase the calculation time. An increase of the scoring volume on the central beam axis will decrease the variations, but will not reflect the dimensions of an ionization chamber as used in dosimetry any more. The variation of 2 % in Figure 3.6 (b) is assumed to come from statistical variations. The accuracy of the current simulations was, however, limited by the available computing power.

4.2 Monte Carlo Simulations for Treatment Planning

4.2.1 GSI Measurements and the WEPL

The Bragg peaks simulated downstream of adipose, cortical bone and titanium show differences in the $FWHM_{BC}$ and peak height compared to the measurements in 3.5. This indicates, that the samples from the Gammex phantom have an inhomogeneous structure. In MC codes, however, the medium is assumed to be homogeneous which will reduce the accuracy of the calculations.

The best agreement is achieved in the calculations and measurements with titanium. This is because the sample thickness was only 2.83 mm and the influence of inhomogeneous sections is reduced. To simulate inhomogeneities present in the measured samples or any other media correctly, MC calculations should be based upon an image of the medium. This can be from a CT scan as done in treatment planning.

The differences in measured peak dose with a Roos- and an Advanced Roos chamber, shown in Figure 3.7, are due to two effects: first, the sensitive diameter is larger for the Advanced Roos chamber decreasing the mean integral dose due to the larger volume. Second, the Advanced Roos chamber can detect particles scattered with a larger angle, increasing the dose especially at large depths. Hence, these two effects can cancel to a certain degree. However, for dosimetry the sensitive diameter has to be large enough to detect all particles and to measure correct doses.

The necessity of the WEPL compared to a mass density scaling becomes clear in the results in Table 3.4. The fact that the WEPL differs from the density is due to the stopping power which depends mainly on the atomic charge density of the target rather than on the mass density. The WEPL takes that effect into account, because it reflects the range of the beam and thus the stopping power.

As shown in Table 3.4 and Figure 3.8 and 3.9, a variation in energy or media thickness studied here does not influence the WEPL significantly. Hence, there is no need to convert CT Hounsfield Units to WEPL's depending on the primary ion beam energy or target media thickness and no additional look up tables are needed.

The measured WEPL at GSI, HIT and the simulated WEPL for SHIELD-HIT in Table 3.4 are in very good agreement. Only for titanium the WEPL from SHIELD-HIT is 3 % higher than for the measurements. Thus, the simulated range within titanium is smaller than the measured range which is also observed in 3.5. This might be, because SHIELD-HIT uses a density of 4.54 g/cm^3 , also stated in ICRU49, whereas various periodic tables of the elements provide values of 4.5 to 4.507 g/cm^3 . A lower medium density will increase the range and decrease the WEPL simulated with SHIELD-HIT.

A revision of the media description and I-value data in ICRU37 and 49 is suggested, especially for tissue equivalent media. Additional depth-dose measurements with titanium implants or real tissue will further improve the recently used values of WEPL in treatment planning.

The results in Table 3.4 and the study in [Ackermann et al., 2008] show that the MC is sufficient to simulate the WEPL for various tissue equivalent media. The accuracy of the WEPL in SHIELD-HIT mainly depends on the uncertainties in the I-value of the medium. However, the bin size influences the accuracy as well. The accuracy of SHIELD-HIT calculated WEPL in this work is below 2.1 % and below 1.3 % for smaller bins. In the measurements the uncertainty is only about 0.5 %. Hence, to determine the WEPL measurements may be preferred to MC calculations to avoid range uncertainties due to I-value uncertainties.

4.2.2 Carbon Ion Beam Depth-Dose Curve Scaling

Water equivalent depth-dose curve parameters can be calculated with the scaling eq. 2.31 in 3.7. Hence, the FWHM_{BC} , DEW and PED can be calculated from eq. 3.1, 3.2 and 3.3 for any media studied here and could be used to correct pencil beam calculations in water.

The scaling is applied to any medium except inflated lung, where a constant value of C in eq. 2.31 could not be determined as for the other media. Whether the use of different values of C is sufficient should be further studied. However, there is no standardized model for lung available yet to use in heavy ion MC codes and the chemical parameters describing the human lung should be studied in more detail for correct range calculations.

A comparison of MC simulations to measurements with lung media was not possible, since the tissue equivalent sample provided in the Gammex phantom (used for the measurements at GSI) shows a macroscopic spongy structure which cannot be simulated with SHIELD-HIT. Hence, it is necessary to implement new features in the MC which can describe tissue inhomogeneities according to an image of the studied medium. Furthermore, this will offer new benchmark studies for MC dose distributions within any medium, which can decrease range uncertainties in media due to I-value uncertainties.

The scaling expressions in Figures 3.10 to 3.12 are derived from Bragg curves obtained in only one target medium without inhomogeneities or interfaces parallel to the beam. Hence, the effects derived there are larger than they would be in the human body. To reflect the situation in the human body more realistically, depth distributions from 300 MeV/u carbon ion beams are simulated in water with cortical bone (cb) and titanium (Ti) inserts of different thickness (60 - 100 mm for cb and 30 - 50 mm for Ti), which are placed at the beam entrance. Other media like adipose or muscle are not discussed, since the influence on depth-dose parameters is negligible for tissue densities close to water, as seen in 3.7.

The resulting WEPL scaled depth-dose curves for cortical bone and titanium are shown in Figure 4.2. In (a) the ordinate is normalized to the maximum energy in the peak to compare the FWHM_{BC} at the 50 % dose and the DEW at the 20 % to 80 % dose. The influence of cortical bone and titanium in the beam on the DEW is negligible.

For 80 mm cortical bone and 50 mm titanium the difference of the FWHM_{BC} compared to water becomes significant by 0.7 mm and 1.8 mm (7 % and 29 %), respectively and a correction of pencil beam algorithms is suggested for titanium inclusions. The

fraction of cortical bone depends on the human skeleton and is probably small compared to less dense bone media. Hence, the effects on the FWHM_{BC} and PED observed here, could overestimate the actual values. However, a correction of pencil beam calculated depth-dose curves may be relevant for thick bone structures like the hips.

The peak to entrance dose shown in (b) depends on the thickness of the media in the beam as well. Here, the ordinate is shown in absolute values. The peak height increases with decreasing range of the particles, which is simply due to the energy straggling. An increase of the PED up to 4.6 % for 60 mm bone is probably worth considering in the TPS, to ensure the homogeneity within pencil beam calculations of SOBP's.

Furthermore, variations in the dose tail are observed in 4.2 (b). The dose depends on the density and thickness of the medium and increases for media densities smaller than water and vice versa. For 50 mm titanium, the deposited energy is about 46 % smaller than in water. This effect will be critical for media densities smaller than water, because the dose will increase and the TPS will underestimate the actual dose. The applied dose to healthy tissue and organs at risk will be larger than calculated and can cause side effects. Hence, it should be avoided to stop the beam in front of an organ at risk as already suggested due to range uncertainties, or to correct for the changes in the FWHM_{BC} and PED numerically.

The step observed in Figure 4.2 (b) in the violet curve at the interface between titanium and water decreases the deposited energy by 3 % calculated with the WEPL as compared water. Small steps for the other media are observed as well, but their dimensions vary. Since a direct conversion of dose to titanium to dose to water via the water-to-media stopping power ratio shows a smooth intersection, the step is probably due to the WEPL scaling. Furthermore, it should be determined if this effect is also observed using the treatment planning software.

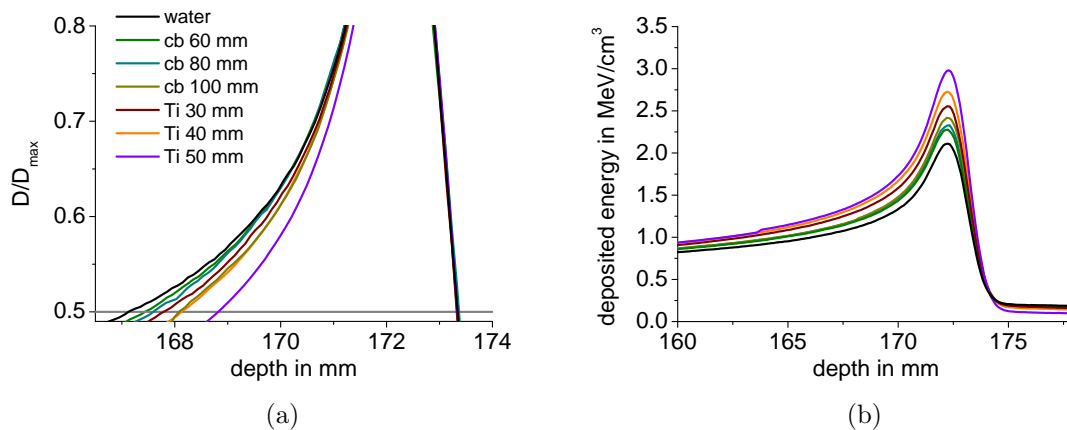


Figure 4.2: Bragg curves for a 300 MeV/u carbon ion beam after applying the WEPL scaling. The deposited energy is normalized to the maximum against water depth in (a), which is shown only up to 0.8, and in absolute deposited energy in (b).

To test the applicability of the scaling method to inhomogeneous media, the FWHM_{BC} and PED for beams passing through varying thicknesses of bone or titanium before stopping in water are calculated using both, the scaling method and directly from the depth-dose curves from SHIELD-HIT simulations in Figure 4.2 (a) and then compared. Parameters from the scaling method are found using a weighted average of parameters

calculated for each medium. This average takes the FWHM_{BC} scaled for cortical bone or titanium and for water and weights them according to the distance traveled in that medium. For titanium and bone, this distance is the sample thickness, which varies from 60 - 100 mm for cortical bone and 30 - 50 mm for Ti. The distance in water is found so that the total water equivalent range agrees with the known value of 172.9 mm for a 300 MeV/u carbon ion beam. For example, for a 20 mm thickness of bone in the beam path, the scaling derived parameters for Ti are weighted by 11.57 % compared to 88.43 % for those for water.

Table 4.1 shows the FWHM_{BC} and PED taken from Figure 4.2 and calculated from the effective atomic charge scaling as described above. The scaling underestimates the

Table 4.1: FWHM_{BC} and PED from Figure 4.2 in comparison to that weighted from the scaling in 3.7. The values for water in comparison are 6.22 mm and 5.24 or the FWHM_{BC} and PED. The values in brackets show percentage deviation to the values in water.

medium	thickness in mm	FWHM_{BC} from Figure 4.2 in mm	FWHM_{BC} from scaling in mm	PED from Figure 4.2	PED from scaling
cortical bone	60	5.90 (27)	5.16 (17)	5.41 (3)	5.58 (6)
	80	5.77 (16)	4.81 (23)	5.46 (4)	5.71 (9)
	100	5.25 (11)	4.46 (28)	5.52 (5)	5.92 (13)
titanium	30	5.54 (5)	5.39 (13)	5.51 (5)	6.24 (19)
	40	5.21 (7)	5.12 (18)	5.59 (6)	6.66 (27)
	50	4.52 (15)	4.85 (22)	5.67 (8)	7.27 (38)

FWHM_{BC} in cortical bone in Figure 4.2 by 15 % and overestimates the PED by about 5 %. For titanium the FWHM_{BC} varies between +2 % and -7 % from the values from Figure 4.2 and the PED is overestimated by about 20 % with the scaling and the PED is overestimated by about 5 %. Considering the step in the depth-dose curves in Figure 4.2 (b) the PED derived from the Figure will decrease resulting in an increase in the deviations compared to the scaling.

Compared to the values of the FWHM_{BC} and PED for water in Figure 4.2 of 6.22 mm and 5.23, respectively, the scaling of the PED does not increase the accuracy of results from a pencil beam algorithm. For the FWHM_{BC} an increase of the accuracy is observed for 60 mm and 80 mm cortical bone and for 50 mm of titanium. However, it is not trivial to implement a scaling of Bragg curves in inhomogeneous media in a TPS and a strategy to implement these has to be developed first.

Again, a considerable difference in depth-dose curve parameters derived with SHIELD-HIT compared to pencil beam algorithms is only observed for the FWHM_{BC} and PED for cortical bone thicknesses exceeding 60 mm and for titanium exceeding 20 mm. A correction may be important for example for pelvic tumors, when the beam travels through the hips, which may also be replaced by titanium implants in some cases. For such cases a different beam angle should be considered to avoid passing through the hips or a numerically derived correction factor should be applied to the FWHM_{BC} and PED. Furthermore, the fraction of cortical bone in the human skeleton should be studied in more detail. However, the equations in 3.7 are valid only for this media and initial FWHM and $\Delta E/E$ of the beam. For treatment, the values of a treatment beam should be used instead.

For proton beams, the differences in depth-dose curve parameters with MC and pencil beam will be larger than for carbon ions, since the energy straggling and scattering for protons is higher. Hence, the study should be done for protons in future work as well.

The lateral width (the actual FWHM) of the beam downstream of tissue equivalent media or interfaces is not studied in this work and will be interesting to study in future. This could relate on the paper by [Szymanowski and Oelfke, 2002], who developed an analytical model of a pencil beam scaling for protons. Whether this model is applicable for carbon ion beams should be investigated, as fragmentation is not included there.

Furthermore, the effect of interfaces parallel or at a certain angle toward the central beam axis on depth-dose curve parameters is not studied here and will influence the Bragg curve further. This needs to be studied as well, especially for interfaces with large density variations like air and bone in the head region.

4.3 Comparison of SHIELD-HIT to Geant4 and FLUKA

4.3.1 Depth Distributions

Calculating a mean difference of the root position over all particles, energies and media according to 2.8, the difference between root positions (see 3.8.1) with SHIELD-HIT and Geant4 is -0.39 ± 0.39 mm and -0.57 ± 0.54 mm to FLUKA. The standard deviation is as large as the mean calculated differences in root positions and shows the broad variations of the determined differences.

By looking at Figures 3.13 to 3.15, the agreement between SHIELD-HIT and FLUKA is superior than that of SHIELD-HIT and Geant4, but could not be quantified correctly with the root position. This is because the root position does not only reflect the range of the primary particles, but also the gradient of the Bragg peak fall-off. A steeper fall-off will result in a smaller root position. The gradient with SHIELD-HIT and Geant4 is steeper than for FLUKA, which results in a better agreement in root positions for SHIELD-HIT and Geant4, although the Bragg peak with FLUKA is at most closer to SHIELD-HIT in Figures 3.13 to 3.15. However, the small differences in the Bragg peak positions will probably not influence treatment planning.

The estimated differences in root positions given in Table 3.6 should be handled with care, since the values for particles traveling through air for the three aperture setups are not in complete agreement. Ideally the three Bragg peaks should be at exactly the same position, which they are not for any of the MC codes and are summarized in Table 4.2. The standard deviation is less than 0.3 mm, which may serve as an estimation of the accuracy of the determination of the root positions in that case.

Table 4.2: Mean root position and standard deviation in brackets derived from protons (P) and carbon ions (C) traveling through air.

energy in MeV/u	root pos. SHIELD-HIT	root pos. Geant4	root pos. FLUKA
P 100	78.61 (0.01)	78.71 (0.02)	78.66 (0.04)
P 200	263.29 (0.15)	263.59 (0.12)	163.44 (0.26)
C 400	276.10 (0.20)	276.16 (0.09)	276.92 (0.12)

The largest difference in the root position in water is obtained downstream of the lateral inhomogeneity of lung/air for 400 MeV/u carbon ions in Table 3.6. Furthermore, the underestimation of Geant4 in the entrance dose is highest for this case and could be due to fewer interactions, resulting in a larger range due to particles having more energy. The underestimation can also be due to a dose buildup of secondary electrons, which is not taken into account in SHIELD-HIT and FLUKA. The effect observed here is not present in the Geant4 version used in [Pshenichnov et al., 2006], and its origin is not solved yet. Therefore, their Geant4 version has to be compared to the version used in this thesis to ensure correct entrance dose calculations.

Bragg curves obtained from the three different MC codes do not agree due to several reasons. The main reason may be a variation in the implemented Bethe-Bloch equation where different approximations and correction factors could lead to range differences. Moreover, the electromagnetic transport and the fragmentation model implemented in the codes could differ and they are benchmarked to different experimental data. Furthermore, the I-values used for the calculations were not exactly the same (see 2.8), but this influences the range only by 0.02 mm. However, the difference in the root position or in range will not affect the accuracy of radiotherapy as long as the MC used for treatment planning at a therapy facility is benchmarked against measurements performed at the local system. To understand the differences in range, the codes should be compared to the same experimental data. In this comparison the treatment head, which is used in the experiment, should be carefully implemented in the codes to take into account secondary particles from the treatment head entering the geometry.

In section 2.8, depth-dose curves are only calculated for a cylindrical scoring radius of 100 mm. In [Henkner et al., 2009b] in appendix G on page XV, SHIELD-HIT and Geant4 are compared for a radius of 10 mm for protons as well. This gives an estimation on the predictions of the lateral scattering model. The deposited energy in the plateau region is about 5 % higher with SHIELD-HIT for a 10 mm radius than compared to Geant 4. For a 100 mm radius the mean difference is about 1.5 %. This indicates that the lateral scattering with SHIELD-HIT is smaller, which is further confirmed in the penumbra of profiles for protons in 3.8.2.

Whereas Geant4 and FLUKA are in agreement in the fragment tail, SHIELD-HIT differs by up to +35 %. An overestimation of the tail region is also observed in a comparison to measured depth-dose curves published in [Sihver et al., 1998] in Figure 4.3 (a). Furthermore, the need to decrease PARLEV(39) to 0.8 is confirmed in the peak height in Figure 4.3 (a) and (b). In (b), simulations downstream of air for 400 MeV/u carbon ions are shown for Geant4 and FLUKA as dots in blue and orange and for SHIELD-HIT with PARLEV(39)=1.0 in grey and 0.8 in black. As already mentioned, the peak height cannot be determined with the given resolution, but from the rising part toward the Bragg peak, a value of 1.0 for PARLEV(39) disagrees with the two other MC codes and a value of 0.8 is more appropriate for all simulated carbon beams.

Range uncertainties as well as the FWHM_{BC} could not be studied due to an under-sampling and will be of interest in future work with a decreased bin size. Experimental depth-dose data should be used in a comparison to results from MC codes to further clarify differences in range and lateral scattering.

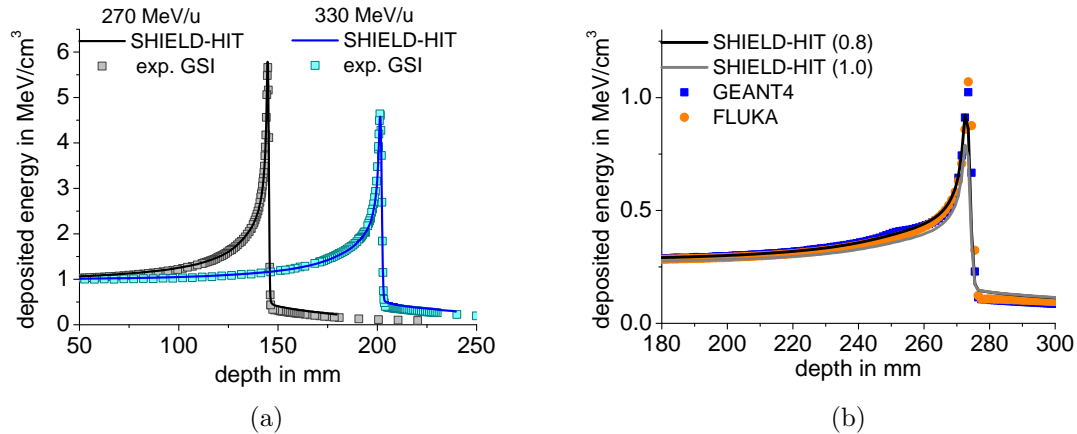


Figure 4.3: SHIELD-HIT calculations ($\text{PARLEV}(39)=0.8$) and measurements of a 270 and 330 MeV/u primary carbon ion beam in (a). SHIELD-HIT overestimates the fragment tail but describes the peak height very well.

4.3.2 Beam Profiles

The dose variations in 3.8.2 can be explained by the differences in depth-dose curves. For, e.g. beam profiles at 50 mm depth downstream of lung/air, the deviations of SHIELD-HIT to Geant4 and FLUKA are 7 % and 3.5 %, respectively. As seen in Figure 3.14 (a) the Bragg peak is at lowest depth with SHIELD-HIT and at highest with Geant4. The Bragg peak with FLUKA is in between. However, the agreement between the three codes is better than 2 % for particles traveling through air.

Deviations in the penumbra in 3.8.2 is mainly defined by the scattering model implemented in the codes. To understand the differences in range, deposited energy and penumbra the codes should be compared to experimental data including calculations of the treatment head. A comparison of Bethe-Bloch calculated stopping powers used in the MC codes can further clarify whether the differences are due to the physical transport and nuclear models or from the stopping power calculations.

As reported in 2.4.3, the MC is used to simulate depth-dose curves in water for different energies used for treatment planning. It would be useful to compare treatment plans calculated with two sets of simulated depth-dose curves, coming from two different codes, to estimate the robustness of treatment planning in terms of MC based depth-dose data in water.

4.4 Benchmark of SHIELD-HIT

4.4.1 The MLFC for Protons and Carbon Ions

About 0.15 % of the incoming protons leave the MLFC with SHIELD-HIT in 3.10.1. This is not forbidden by conservation laws and can be due to neutrons kicking out protons, but is neither observed in the calculations with Geant4 nor in the experiment. However, the influence of the particles leaving the MLFC and the underestimated total inelastic cross section with SHIELD-HIT on proton depth-dose curves is negligible and will not affect the accuracy of proton dose treatment planning.

The MLFC is sensitive to the fragmentation of a carbon ion beam, but only to the

total amount of charge produced by the fragments in the peak region in 3.10.2. The same information can in principle be obtained by measuring a depth-dose curve. As shown in Figure 3.19, the Bragg peak height is sensitive to PARLEV(39) and the total inelastic cross section as well. Thus, a measurement with an MLFC in an ion beam would probably not lead to a better understanding of fragmentation, which would be of significant interest for radiobiological calculations, since the response of the tissue depends on the fragment type.

4.4.2 Distributions of Fragments in a Carbon Ion Beam

Variations in measured and calculated ranges and peak heights in Figure 3.23 indicate that the actual value for $\Delta E/E$ differs from the 0.5 % as given in [Haettner, 2006]. Furthermore, there seems to be an inconsistency in the measured depth data. Whereas for hydrogen in Figure 3.25 (b) the calculated differential cross sections are lower than measured, the calculations of set D in Figure 3.25 (e) are larger than the measurements. It is assumed that the integration or interpolation of the angular distributions may be inaccurate in the range between 0° to 10° . Therefore, the partially published experimental data may have to be reviewed.

However, the initial beam spread might be relevant for the fragment production at the Bragg peak, which was not measured at GSI, but should be studied in future experiments.

In Figure 3.24, a value of PARLEV(39) of 1.0 in set B, Table 3.9, does not reproduce the measured amount of carbon ions. Hence, a reduction to 0.8 in Set A is required for correct calculations.

The error in the number of carbon ions in Figure 3.24 (b) of $\pm 17\%$ at 0° for measurements from February and July 2005 are huge, since carbon ions are the primary particles and the signal to noise ratio is assumed to be small. Big uncertainties, which can be even larger for the fragments and thin water tank thicknesses, make it more difficult to reasonably benchmark MC codes. Nevertheless, the measurements are still useful to improve the cross sections in SHIELD-HIT and other MC codes.

The new values for PARLEV(34) and (33) of 17 and 0.3, respectively, show a considerable improvement in differential cross sections 3.11. The differential cross sections for hydrogen for angles above 2° could not be improved with the setup in D. Improvements in this region can probably only be achieved by changes in the lateral scattering model. Therefore, the nuclear and electromagnetic calculations in SHIELD-HIT should be studied separately and the lateral scattering cross sections should be revised.

A comparison of SHIELD-HIT calculated depth-dose curves with set A and set B is shown in Figure 4.4. The grey squares, which belong to the right abscissa, show the ratio of the deposited energy with these two sets. The deposited energy increases toward the Bragg peak up to 2 % and is 1.8 % higher at the peak for set D, which is mainly due to an increased number of hydrogen fragments. At the end of the range and the first 50 mm of the fragment tail an increase by 5 % is observed with set D. Compared to Figure 4.3 this will further increase the already observed overestimation of the measured tail of 35 % by about 3 %. Whether the overestimation in the tail region comes from increased differential cross sections for B and Be in SHIELD-HIT, should be studied in a revision of the cross section data in future. The FWHM of the Bragg curve is increased by 4 mm for set D and should be validated against experimental Bragg curves in future studies.

The origin of the overestimation of dose in the tail region with SHIELD-HIT should be studied in future work as well as the possibility to further improve the calculated differential cross sections for RBE calculations. A more comprehensive comparison of nuclear- and electromagnetic cross sections to experimental data may be needed. Furthermore, the sensitivity of variations in fragments on the RBE calculations should be studied with the treatment planning software.

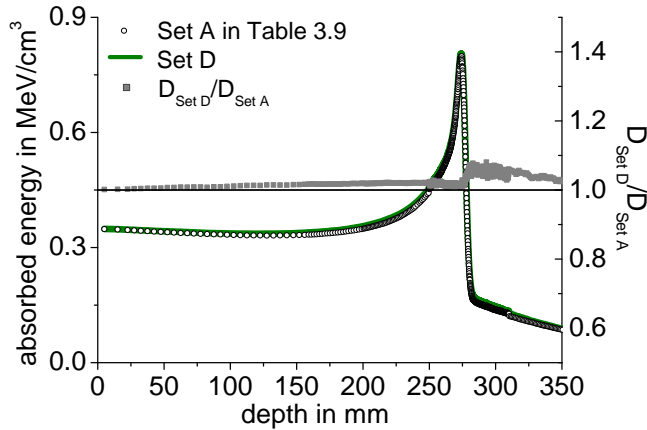


Figure 4.4: Influence of PARLEV(34) and (33) on the Bragg curve for a 400 MeV/u carbon ion beam. The deposited energy is increased in the tail region up to 5 % for values of 17 and 0.3 for PARLEV(34) and (33) in green.

4.5 Neutron Equivalent Dose from Carbon Ion Treatment

The neutron equivalent dose from a carbon ion treatment calculated in a phantom of an eleven year old male patient in the brain region is about three orders of magnitude smaller than compared to protons for the investigated case (3.12). This is probably because carbon ions are very energetic and the neutrons produced are directed forward and mostly leave the body without interactions.

Neutrons produced or scattered from the treatment room are not considered here and probably increase the number of neutrons in the patient due to backscattering especially for carbon. The reduced number of primary particles as well as the increased RBE for carbon ions compared to protons will decrease the neutron dose needs. However, final statements for carbon ions on age or target volume dependent neutron equivalent doses can only be made when all data are analyzed and the treatment room configuration are included.

As reported in [Yonai et al., 2008], the neutron dose depends on the beam setting and the arrangement of the beamline. However, similar to the findings here, the neutron dose due to scattered carbon ions is smaller than for scattered protons.

As known from protons in [Jarlskog and Paganetti, 2008a], the neutron equivalent dose increases with decreasing patient age due to the smaller body size as the organs are closer to the target. Hence, attention must be paid to the treatment of pediatric patients, since also the cancer risk increases with decreasing patient age [Beir, 2006]. Furthermore, the neutron equivalent dose increases with increasing target volume size due to an increase in particle fluence required to cover the target volume.

5 Conclusions and Outlook

The I-value and Water-to-Air Stopping Power Ratio

- It is suggested to use an I-value for water of 80.8 eV as published in [Paul et al., 2007] in SHIELD-HIT.
- A revision of the inconsistent stopping power and I-value data for water in ICRU49 and 73 is suggested.
- It should be studied if the stopping power and I-value data are inconsistent for other media published in ICRU49 and 73.
- The adopted constant of 1.13 in IAEA TRS-398 overestimates the $S_{w/air}$ with $I_w=80.8$ eV and $I_{air}=85.7$ eV by about 1 %, which reduces the accuracy of dose measurements with ionization chamber by 1 %.
- Whether the use of a constant value of $S_{w/air}$ is practical for pencil beams and SOBPs should be discussed as well as a suggestion for a reference position for dosimetry in SOBP's.
- The $S_{w/air}$ can be simplified with sufficient accuracy by the approximation given in equation 2.22. MC is only required if a high precision is needed at the end of the range, e.g in plane-parallel ionization chambers.
- To reduce range uncertainties, e.g. due to I-value inaccuracies, several improvements could be made. E.g. an increase of the tumor margin and the delineated volume of organs at risk, and the usage of multiple beam directions.
- SHIELD-HIT calculates the mean I-value of the compound via the Bragg additivity rule, which can only approximate the I-values. The effects are restricted to a very small shift in the range of 0.02 mm in water. For future comparisons to ICRU data or other MC codes it is suggested to use fixed mean I-values for any media in SHIELD-HIT.

Comparison of MC codes

- SHIELD-HIT, Geant4 and FLUKA do not exactly show the same results in Bragg peak position and lateral energy deposition, which is probably due to model implications and cross section data. To further study the differences in MC codes and to recommend a single code, a comparison of experimental data to calculations including simulations of the treatment head are needed, as done in the IAEA Coordinated Research Project [IAEA, 2007].
- Range deviations as well as stopping power uncertainties will not influence the accuracy of treatment planning in water, when MC hadron transport codes are

adjusted to measured depth-dose curves in water. Furthermore, it is suggested to simulate the treatment head geometry in the MC as well. This ensures a correct calculation of the primary particle field entering the patient.

- The comparison to Geant4 and FLUKA showed further:
 - To make SHIELD-HIT more powerful the main code and all sub programs should be transferred completely to Linux.
 - It is suggested to write an English manual for SHIELD-HIT.
 - For CT based treatment planning with SHIELD-HIT the voxel geometry needs to be implemented. Currently SHIELD-HIT cannot calculate on CT data, which makes it very difficult to determine patient related studies for, e.g. radiation induced secondary doses in patient phantoms.

Pencil Beam Scaling Methods

- The effective atomic number of a medium can be used to scale depth-dose curve parameters to parameters in water.
- The difference of the values of FWHM_{BC} and PED calculated with SHIELD-HIT and the pencil beam algorithm depends on the amount and type of media in the beam path. For cortical bone and titanium a correction with MC calculated FWHM_{BC} and PED values is suggested. However, it is not straightforward to apply the scaling developed here to inhomogeneous media.
- The primary beam energy as well as the thickness of the media do not have to be included in the currently used WEPL look up table.
- The WEPL for titanium should be measured for a clinically used titanium sample to check the currently used look up table, since an inconsistency in the data of the mass density is observed.
- A recommendation on how to handle lung tissue in MC is needed.
- It is suggested to benchmark MC depth-dose curve calculations to measurements with media samples based on images of these samples, e.g. a CT, to account for inhomogeneities. As shown in 3.5, SHIELD-HIT always regards a medium being homogeneous. Heterogeneous structures inside the medium, which will influence the shape of the Bragg curve, are not calculated.
- For CT based MC calculations an unambiguous classification of CT HU to the media type is needed while CT data only provide the electron density of the medium. It is suggested to use the CT HU to media correlation in [Jiang et al., 2007] for carbon ion MC calculations.
- Absolute dose values in media calculated with MC should be converted into dose to water by the water-to-media stopping power ratio to successfully compare them to measurements in water, e.g. in dosimetry or treatment plan verification measurements. For protons this was already done in [Paganetti, 2009]. The same idea can be used for carbon ion beams as well.

Benchmark of the Fragmentation Model

- For correct SHIELD-HIT depth-dose and carbon differential cross section calculations it is urgently suggested to use $\text{PARLEV}(39)=0.8$.
- It is suggested to change the default values of 1.0 for $\text{PARLEV}(34)$, and (33) to 17 and 0.3, respectively, which will considerably improve the calculation of differential cross sections of fragments compared to measurements. Thus, SHIELD-HIT08 calculations can be used as an input in the LEM model [Scholz et al., 1997], which is used to calculate the radiobiological effectiveness (RBE) of a mixed particle field from primary protons and carbon ions.
- To further improve the nuclear and electromagnetic cross sections in SHIELD-HIT, it is suggested to separate the nuclear from the electromagnetic model and to revise the total inelastic cross section for protons and boron ions.
- It is suggested to measure differential cross sections in the Bragg peak as well, because the RBE significantly increases toward the end of the Bragg peak and a correct MC calculation of the RBE is mandatory for correct doses in carbon ion therapy.
- Due to an inconsistency in differential cross sections for hydrogen and helium, it is suggested to review the data published in [Haettner et al., 2006] as well as the not yet published data in [Haettner, 2006], .
- MLFC data from carbon ions will not give additional information about the fragmentation model in the MC, hence it is not recommended as a standard test for MC codes for carbon ions.

Neutron Equivalent Dose from Carbon Ion Treatment

The equivalent neutron dose study from carbon ion treatment has to be further analyzed to make final conclusions. The preliminary results show a considerable decrease of neutron dose from a carbon ion treatment compared to a proton treatment. However, the influence of the treatment room configuration has to be included.

Bibliography

- [Ackermann et al., 2008] Ackermann, B., Henkner, K., Parodi, K., Ellerbrock, M., and Jäkel, O. (2008). Vergleich von relativen Reichweiten bei Protonen- und Kohlenstoffionenstrahlen. *TagungsCD der 39. Jahrestagung Oldenburg. Deutsche Gesellschaft für Medizinische Physik (DGMP)*.
- [Agostinelli et al., 2003] Agostinelli et al. (2003). Geant4 - a simulation toolkit. *Nuclear Instruments and Methods, A* 506:250–303.
- [Andreo, 1991] Andreo, P. (1991). Monte Carlo techniques in medical radiation physics. *Phys. Med. Biol.*, 36 No. 7:861–920.
- [Andreo, 2009] Andreo, P. (2009). On the clinical spatial resolution achievable with protons and heavier charged particle radiotherapy beams. *Phys. Med. Biol.*, 54:N205–N201.
- [ATIMA, 2007] ATIMA (2007). <http://www-linux.gsi.de/weick/atima/>.
- [Barashenkov and Toneev, 1973] Barashenkov, V. S. and Toneev, V. D. (1973). Neutron fluxes generated by high energy protons in the thick uranium block. *Atomic Energy*, 53:163.
- [Battistoni et al., 2007] Battistoni, G., Muraro, S., Sala, P. R., Cerutti, F., Ferrari, A., Roesler, S., Fasso, A., and Ranft, J. (2007). Proceedings of the Hadronic Shower Simulation Workshop 2006, Fermilab 6–8 September 2006, M. Albrow, R. Raja eds. *AIP Conference Proceeding*, 896:31–49.
- [Beir, 2006] Beir (2006). Health risks from exposure to low levels of ionizing radiation. *BEIR VII (Phase 2. National Research Council, National Academy of Science)*.
- [Bichsel and Hiraoka, 1992] Bichsel, H. and Hiraoka, T. (1992). Energy loss of 70 MeV protons in elements. *Nucl. Instrum. Methods B*, 66:435.
- [Bichsel et al., 2000] Bichsel, H., Hiraoka, T., and Otama, K. (2000). Aspects of fast-ion dosimetry. *Rad.Res.*, 153:208–19.
- [Botvina et al., 1987] Botvina, A. S., Iljinov, A. S., and Mishustin, I. N. (1987). Statistical simulation of the break-up of highly excited nuclei. *Nucl. Phys.*, 475:663.
- [Brandt, 1975] Brandt, W. (1975). *Atomic Collisions in solids (Plenum, New York)*, 1:261.
- [Brun et al., 1987] Brun, R., Bruyant, F., Maire, M., McPherson, A. C., and Zanarini, P. (1987). *GEANT 3: user's guide Geant 3.10, Geant 3.11; rev. version*. CERN, Geneva.
- [CERN, 1994] CERN (1994). CERN W5013 Program Library Long Writeup. *section PHYS325*.
- [Coleman and Armstrong, 1971] Coleman, W. A. and Armstrong, T. W. (1971). NMTC-A Nucleon-Meson Transport Code. *Nucl. Sci. Eng.*, 43:353.
- [Fasso et al., 2005] Fasso, A., Ferrari, A., Ranft, J., and Sala, P. R. (2005). FLUKA: a multi-particle transport code. *INFN/TC_05/11, SLAC-R-773*.

- [Fry et al., 2005] Fry, D., Sewchand, W., and Connell, J. (2005). An in-depth generic characterization of monte carlo generated proton depth-dose. *PTCOG Abstract book*.
- [Geant4, 1999] Geant4 (1999). Collaboration. <http://geant4.web.cern.ch>.
- [Geithner, 2006] Geithner, O. (2006). *Monte Carlo simulations for heavy ion dosimetry*. PhD thesis, Combined Faculties for the Natural Sciences and for Mathematics of the Ruperto-Carola University of Heidelberg.
- [Geithner et al., 2006] Geithner, O., Andreo, P., Sobolevsky, N., Hartmann, G., and Jäkel, O. (2006). Calculation of stopping power ratios for carbon ion dosimetry. *Phys. Med. Biol.*, 51:2279–92.
- [Gottschalk et al., 1999] Gottschalk, B., Platais, R., and Paganetti, H. (1999). Nuclear interactions of 160 MeV protons stopping in copper: A test of monte carlo nuclear models. *Med. Phys.*, 26:2597–2601.
- [Gudima et al., 1983] Gudima, K. K., Mashnik, S. G., and Toneev, V. D. (1983). Cascade-excitation model of nuclear reactions. *Nucl. Phys.*, A401:329.
- [Gudowska et al., 2004] Gudowska, I., Sobolevsky, N., Andreo, P., Belkic, D., and Brahme (2004). Ion beam transport in tissue-like media using the monte carlo code SHIELD-HIT. *Phys. Med. Biol.*, 49:1933–58.
- [Haberer et al., 1993] Haberer, T., Becher, W., Schardt, D., and Kraft, G. (1993). Magnetic scanning system for heavy ion therapy. *Nucl. Instrum. Meth. Phys. Res.*, A330:296–305.
- [Haettner, 2006] Haettner, E. (2006). Experimental study on carbon ion fragmentation in water using GSI therapy beams. Master’s thesis, Kungliga tekniska högskolan, Stockholm.
- [Haettner et al., 2006] Haettner, E., Iwase, H., and Schardt, D. (2006). Experimental fragmentation studies with ^{12}C therapy beams. *Radiation Protection Dosimetry*, Vol. 122, No. 1-4:485–87.
- [Henkner et al., 2009a] Henkner, K., Bassler, N., Sobolevsky, N., and Jäkel, O. (2009a). Monte carlo simulations on the water-to-air stopping power ratio for carbon ion dosimetry. *Med. Phys.*, 36 (4):1230–35.
- [Henkner et al., 2009b] Henkner, K., Sobolevsky, N., Jäkel, O., and Paganetti, H. (2009b). Test of the nuclear interaction model in SHIELD-HIT and comparison to energy distributions from GEANT4. *Phys. Med. Biol.*, 54:N509–N517.
- [Hollmark et al., 2008] Hollmark, M., Gudowska, I., Belkic, D., Brahme, A., and Sobolevsky, N. (2008). An analytical model for light ion pencil beam dose distributions: multiple scattering of primary and secondary ions. *Phys. Med. Biol.*, 53:3477–91.
- [Hubert et al., 1989] Hubert, F., Bimbot, R., and Gauvin, H. (1989). Semi-empirical formulae for heavy ion stopping powers in solids in the intermediate energy range. *Nucl. Instrum. Meth. Phys. Res.*, B36:357–63.
- [Hughes et al., 1997] Hughes, G., Adams, K. J., Chadwick, M. B., Comly, J. C., Frankle, S. C., Hendricks, J. S., Little, R. C., Prael, R. E., Waters, L. S., and Young, P. G. (1997). MCNPXTM-The LAHETTM/MCNPXTM Code Merger. *Proc. of Third Workshop on Simulating Accelerator Radiation Environments (SARE 3)*.
- [IAEA, 2007] IAEA, C. (2007). Coordinated Research Project, Heavy Charged-Particle Interaction Data for Radiotherapy (codename charpar), 2007-2009.

- [ICRP, 2003] ICRP (2003). Basic anatomical and physiological data for use in radiological protection: reference values. *International Commission on Radiological Protection (Oxford: Pergamon)*, page 60.
- [ICRU37, 1984] ICRU37 (1984). Stopping powers for electrons and positrons. *International Commission on Radiation Units and Measurements, Bethesda*.
- [ICRU49, 1993] ICRU49 (1993). Stopping powers and ranges for protons and alpha particles. *International Commission on Radiation Units and Measurements, Bethesda*.
- [ICRU73, 2005] ICRU73 (2005). Stopping of ions heavier than helium. *Oxford University Press*.
- [Iwase et al., 2002] Iwase, H., Niita, K., and Nakamura, T. (2002). Development of general-purpose Particle and Heavy Ion Transport Monte Carlo code. 39(11):1142–51.
- [Jäkel and Reiss, 2007] Jäkel, O. and Reiss, P. (2007). The influence of metal artefacts on the range of ion beams. *Phys. Med. Biol.*, 52 No 3:635–44.
- [Jäkel et al., 2007] Jäkel, O., Schulz-Ertner, D., and Debus, J. (2007). Specifying carbon ion dose for radiotherapy: the Heidelberg approach. *Journal of Radiation Research*, 48(Suppl.A):A87–A95.
- [Jarlskog and Paganetti, 2008a] Jarlskog, C. Z. and Paganetti, H. (2008a). Physics settings for using the GEANT4 toolkit in proton therapy. *IEEE TRANSACTIONS ON NUCLEAR SCIENCE*, Vol. 5 No. 3:1018–25.
- [Jarlskog and Paganetti, 2008b] Jarlskog, C. Z. and Paganetti, H. (2008b). Risk of developing second cancer from neutron dose in proton therapy as function of field characteristics, organ, and patient age. *Int. J. Rad. Oncol. Biol. Phys.*, 72 Issue 1:228–35.
- [Jiang et al., 2007] Jiang, H., Seco, J., and Paganetti, H. (2007). Effects of Hounsfield number conversion on CT based Monte Carlo dose calculations. *Med. Phys.*, 43 (4):1439–49.
- [Kempe and Brahme, 2008] Kempe, J. and Brahme, A. (2008). Energy-range relation and mean energy variation in therapeutic particle beams. *Med. Phys.*, 35:159–70.
- [Kinney, 1964] Kinney, W. E. (1964). The nucleon transport code, NTC. *NTC Report*, ORNL-3610.
- [Koehler et al., 1977] Koehler, A. M., Schneider, R. J., and Sisterson (1977). Flattening of proton dose distributions of large-field radiotherapy. *Med. Phys.*, 4:297–301.
- [Kraft, 2007] Kraft, G. (2007). *Tumor Therapy with Heavy Ions*. Verein zur Förderung der Tumorthherapie mit schweren Ionen e.V.
- [Krämer et al., 2000] Krämer, M., Jäkel, O., Haberer, T., Kraft, G., and Weber, U. (2000). Treatment planning for heavy-ion radiotherapy: Physical beam model and dose optimization. *Phys. Med. Biol.*, 45:3199 – 3317.
- [Krämer and Scholz, 2001] Krämer, M. and Scholz, M. (2001). Treatment planning for heavy-ion radiotherapy: Calculation and optimization of biological effective dose. *Phys. Med. Biol.*, 45:3319 – 30.
- [Kumazaki et al., 2007] Kumazaki, Y., Akagi, T., Yanou, T., Suga, D., and Hishikawa, Y. (2007). Determination of the mean excitation energy of water from proton beam ranges. *Rad. Measurements*, 42:1683.

- [Lee et al., 2006] Lee, C., Williams, J. L., and Bolch, W. E. (2006). Whole-body voxel phantoms of paediatric patients UF Series B. *Phys. Med. Biol.*, 51:4649–61.
- [Metroplis and Ulam, 1949] Metroplis, M. and Ulam, S. M. (1949). The monte carlo method. *J. Am. Stat. Assoc.*, 44:335–41.
- [Molière's, 1984] Molière's, G. (1984). Theory of scattering of fast charged particles: plural and multiple scattering. *Z. Naturforsch.*, 3a, 78.
- [Murty, 1965] Murty, R. C. (1965). Effective atomic numbers of heterogeneous materials. *Nature*, 207:398–399.
- [Paganetti, 2009] Paganetti, H. (2009). Dose to water versus dose to medium in proton beam therapy. *Phys. Med. Biol.*, 54:4399–4421.
- [Paganetti and Gottschalk, 2003] Paganetti, H. and Gottschalk, B. (2003). Test of GEANT3 and GEANT4 nuclear models for 160 MeV protons stopping in CH_2 . *Med. Phys.*, 30:1926–31.
- [Paul and Schinner, 2002] Paul, H. and Schinner, A. (2002). MSTAR: Stopping power for light ions. <http://www.exphys.uni-linz.ac.at/stopping>.
- [Paul et al., 2007] Paul, O., Geithner, H., and Jäkel, O. (2007). The influence of stopping powers upon dosimetry for radiation therapy with energetic ions. *Adv. in Q. Chem.*, Vol. 52:p.290.
- [Podgorsak, 2003] Podgorsak, E. B. (2003). Review of radiation oncology physics: A handbook for teachers and students. *IAEA Educational Report Series*.
- [Pshenichnov et al., 2005] Pshenichnov, I., Mishustin, I., and Greiner, W. (2005). Neutrons from fragmentation of light nuclei in tissue-like media: a study with the GEANT4 toolkit. *Phys. Med. Biol.*, 50:5493–5507.
- [Pshenichnov et al., 2006] Pshenichnov, I., Mishustin, I., and Greiner, W. (2006). Distribution of positron-emitting nuclei in proton and carbon-ion therapy studied with GEANT4. *Phys. Med. Biol.*, 51:6099–6112.
- [Remizovich et al., 1988] Remizovich, V. S., Rogozkin, D. B., and Ryazanov, M. I. (1988). Fluctuations of ranges of charged particles. *Moscow: Energoatomizdat*, chapters 2 and 3:32–99.
- [Rietzel et al., 2007] Rietzel, E., Schardt, D., and Haberer, T. (2007). Range accuracy in carbon ion treatment planning based on CT-calibration with real tissue samples. *Rad. Oncol.*, 2:14.
- [Rossi, 1953] Rossi, B. (1953). *High Energy Particles (Englewood Cliffs, NY: Prentice-Hall)*, page chapter 2.
- [Schardt et al., 1996] Schardt, D., Schall, I., Geissel, H., Irnich, H., Kraft, G., Magel, A., Mohar, M. F., Munzenberg, G., Nickel, F., Schwab, W., and E, C. S. K. (1996). Charge-changing nuclear reactions of relativistic light ion beams ($5 < Z < 10$) passing through thick absorbers. *Nucl. Instrum. Meth. Phys. Res.*, B 117:221–34.
- [Schardt et al., 2008] Schardt, D., Steidl, P., Krämer, M., Weber, U., Parodi, K., and Brons, S. (2008). Gsi scientific report 2007. *GSI Report 2008-1*.
- [Scholz et al., 1997] Scholz, M., Kellerer, A. M., Kraft-Weyrather, W., and Kraft, G. (1997). Computation of cell survival in heavy ion beams for therapy - the model and its approximation. *Radiat. Environ. Biophysics*, 36:59–66.

- [Schümerer et al., 1990] Schümerer, K., Brüchle, W., Morissey, D. J., Schädel, M., Szweryn, B., and Weifan, Y. (1990). Target fragmentation of Au and Th by 2.6 GeV protons. *Phys. Rev.*, C 42:2546–61.
- [SHIELD-HIT, 2008] SHIELD-HIT (2008). <http://www.inr.ru/shield/>.
- [Sihver et al., 1998] Sihver, L., Scharadt, D., and Kanai, T. (1998). Depth-dose distributions of high-energy carbon, oxygen and neon beams in water. *Jpn. J. Med. Phys.*, 18:1–21.
- [Sobolevsky, 1970] Sobolevsky, N. (1970). Program for calculations nucleon-meson cascade in media with monte carlo method. *Dubna (in Russian)*.
- [Sommerer et al., 2006] Sommerer, F., Parodi, K., Ferrari, A., Poljanc, C., Enghardt, W., and Aigner, H. (2006). Investigating the accuracy of the FLUKA code for transport of therapeutic ion beams in matter. *Phys. Med. Biol.*, 51:4385–98.
- [Soukup et al., 2005] Soukup, M., Fippel, M., and Alber, M. (2005). A pencil beam algorithm for intensity modulated proton therapy derived from monte carlo simulations. *Phys. Med. Biol.*, 50:5089–5104.
- [SRIM-2008, 2008] SRIM-2008 (2008). <http://www.srim.org/>.
- [Sternheimer and Peierls, 1971] Sternheimer, R. M. and Peierls, R. F. (1971). General expression for the density effect for the ionization loss of charged particles. *Phys. Rev. B*, 3:3681–92.
- [Szymanowski and Oelfke, 2002] Szymanowski, H. and Oelfke, U. (2002). Two-dimensional pencil beam scaling: an improved proton dose algorithm for heterogeneous media. *Phys. Med. Biol.*, 47:3313–30.
- [Toneev and Gudima, 1983] Toneev, V. D. and Gudima, K. K. (1983). Particle emission in light and heavy ion reactions. *Nucl. Phys.*, A400:173.
- [TRS-398, 2000] TRS-398 (2000). Absorbed dose determination in external beam radiotherapy: An international code of practice for dosimetry based on standards of absorbed dose to water. *International Atomic Energy Agency*.
- [Tuli, 1987] Tuli, J. (1987). Evaluated nuclear structure data file. *BNL-NCS-51655-Rev87*.
- [Vavilov, 1957] Vavilov, P. V. (1957). Ionizational losses of high energy heavy particles. *J. Exp. Theor. Phys.*, 32:920–3.
- [Weber and Kraft, 1999] Weber, U. and Kraft, G. (1999). Design and construction of a ripple filter for a smoothed depth dose distribution in conformal particle therapy. *Phys. Med. Biol.*, 44:2765–75.
- [Wilson, 1946] Wilson, R. R. (1946). Radiological use of fast protons. *Radiology*, 47:487–491.
- [Xu et al., 2000] Xu, X. G., Chao, T. C., and Bozkurt, A. (2000). VIP-MAN: an image-based whole-body adult male model constructed from color photographs of the Visible Human Project for multi-particle Monte Carlo calculations. *Health Phys.*, 78:476–85.
- [Yarlagadda et al., 1978] Yarlagadda, B. S., Robinson, J. E., and Brandt, W. (1978). Effective-charge theory and the electronic stopping power of solids. *Phys. Rev. B*, 17:3473–83.
- [Yonai et al., 2008] Yonai, S., Matsufuji, N., Kanai, T., Matsui, Y., Matsushita, K., Yamashita, H., Numano, M., Sakae, T., Terunuma, T., Nishio, T., Kohno, R., and Akagi, T. (2008). Measurement of neutron ambient dose equivalent in passive carbon-ion and proton radiotherapies. *Med. Phys.*, 35(11):4782–92.

A Comparison of MC codes

Complete set of depth-dose curves from section 3.8.

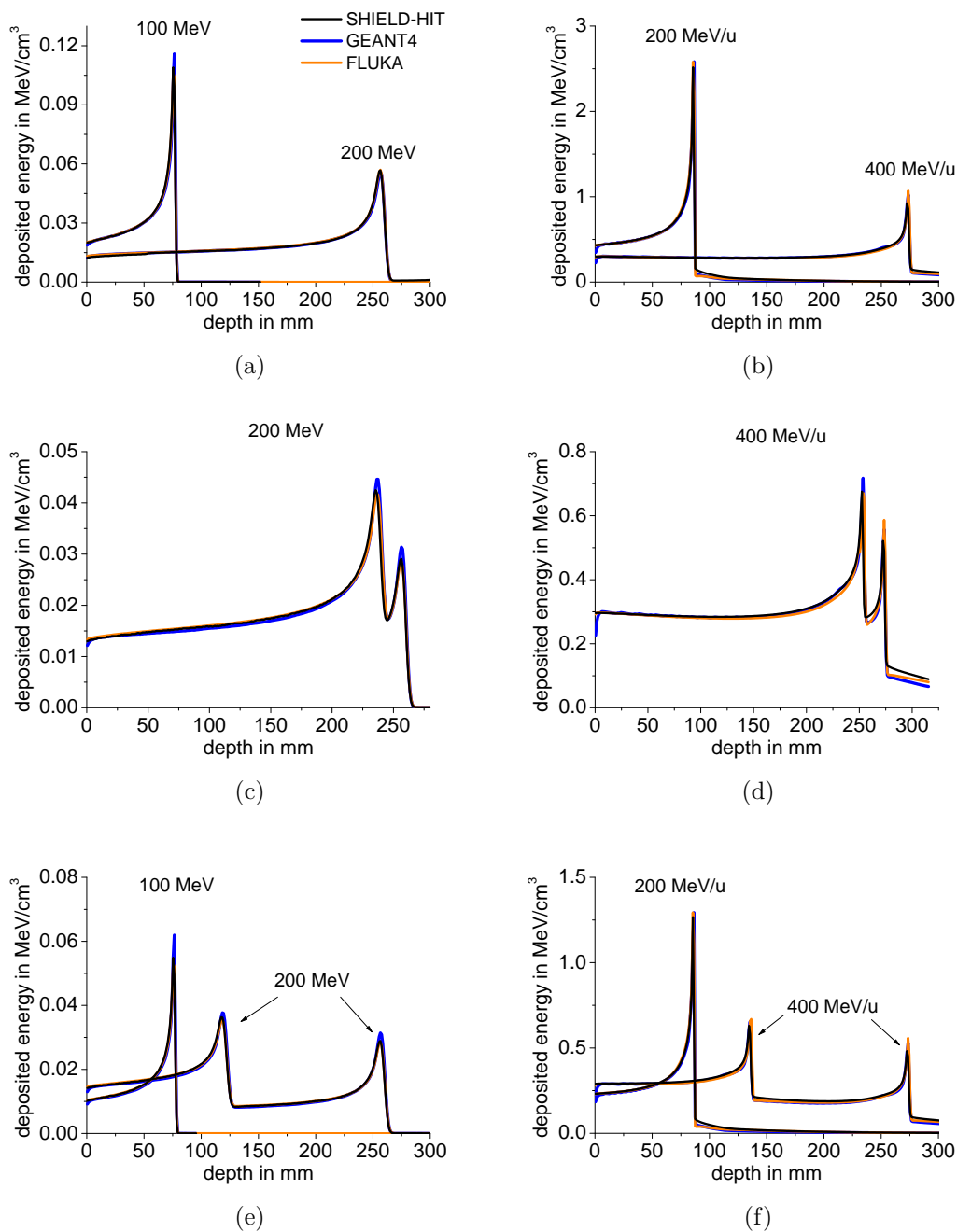


Figure A.1: MC simulated proton and carbon ion depth-dose curves in water downstream of air in (a) and (b), lung/air for 200 MeV protons in (c) and 400 MeV/u carbon ions in (d) and bone/air in (e) and (f).

B Depth Distributions measured at GSI

Shown are the complete depth distribution from 3.5. Figure B.1 shows measured and simulated depth distributions for water, 56.2 mm adipose or cortical bone or 28.3 mm titanium in the beam path. The distributions are measured with a Roos- and an Advanced Roos chamber in water.

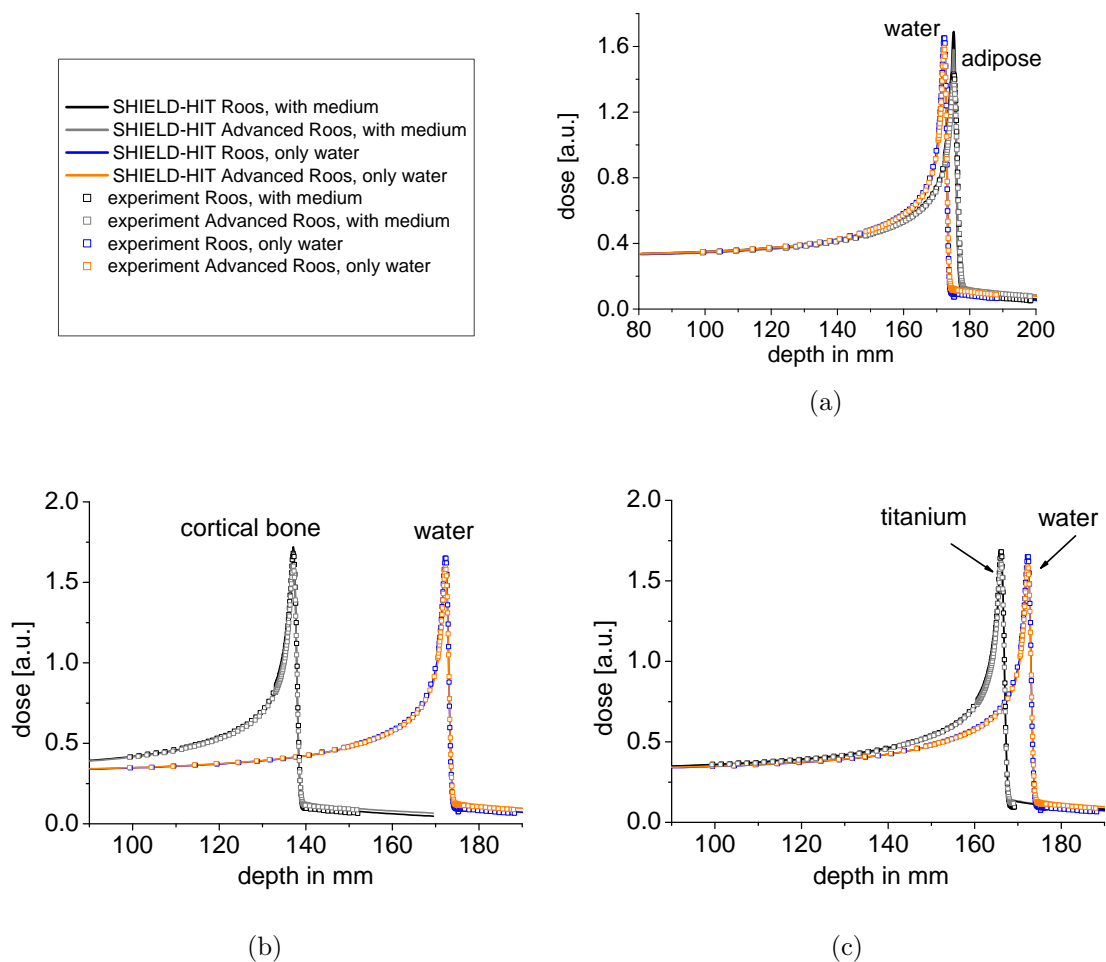


Figure B.1: Measurements (squares) and SHIELD-HIT calculations (line) on the GSI experiment with samples from the Gammex phantom. Black and blue colored curves represent the data for the Advanced Roos chamber and grey and orange curves for the Roos chamber.

C Deviations between Measured and Simulated Angular Distributions

Table C.1: Deviation between SHIELD-HIT data (set A) and the experiment at angles of 0° and 2° and various water depth. The value is rounded up and gives only an estimation on the differences.

fragment type	water thickness	deviation at about $0^\circ / 2^\circ$ in %
H	59 mm	-53 / -52
H	279 mm	-15 / -31
H	347 mm	-20 / -24
He	59 mm	11 / -17
He	279 mm	-2 / -1
He	347 mm	-2 / -2
Li	59 mm	15 / 30
Li	279 mm	34 / 60
Li	347 mm	79 / 57
Be	59 mm	106 / 120
Be	279 mm	121 / 124
Be	347 mm	127 / 146
B	59 mm	40 / -50
B	279 mm	64 / 30
B	347 mm	155 / 120

D Data Table from ICRU37 and 44

Table D.1: Density, mean excitation energy and compositions of media from ICRU37.

medium	mass density in g/cm^3	mean excitation energy I in eV	composition Z of constituent: fraction by weight
adipose	0.92	63.2	1:0.119477; 6:0.637240; 7:0.007970; 8:0.232333; 11:0.000500; 12:0.000020; 15:0.000160; 16:0.000730; 17:0.001190; 19:0.000320; 20:0.000020; 26:0.000020
bone, compact	1.85	91.9	1:0.063984; 6:0.278000 7:0.027000; 8:0.410016; 12:0.002000; 20:0.147000;
bone, cortical	1.85	106.4	1:0.047234; 6:0.144330; 7:0.041990; 8:0.446096; 12:0.002200; 15:0.104970; 16:0.003150; 20:0.209930; 30:0.000100
muscle, skeletal	1.04	75.3	1:0.100637; 6:0.107830; 7:0.027680; 8:0.754773; 11:0.000750; 12:0.000190; 15:0.001800; 16:0.002410; 17:0.000790; 19:0.003020; 20:0.000030; 26:0.000040; 30:0.000050
muscle, striated	1.04	74.7	1:0.101997; 6:0.123000; 7:0.035000; 8:0.729003; 11:0.000800; 12:0.002000; 15:0.002000; 16:0.00500; 19:0.003000

Table D.2: Density, mean excitation energy and compositions of inflated lung from ICRU 44.

medium	mass density in g/cm^3	mean excitation energy I in eV	composition Z of constituent: fraction by weight
inflated lung	0.52	75.02	1:0.103; 6:0.105; 7:0.031; 8:0.749; 11:0.002; 15:0.002; 16:0.003; 17:0.003; 19:0.002

E Data Table from Gammex Phantom Descriptions

Table E.1: Mass density and compositions of media according to the Gammex phantom 467.

medium	mass density in g/cm ³	composition Z of constituent: fraction by weight
lung(LN40)	0.460	1:0.0847;6:0.5957;7:0.0197;8:0.1811; 12:0.1121;14:0.0058;17:0.0010
adipose RMI 453	0.942	1:0.0906;6:0.7230;7:0.0225;8:0.1627; 17:0.0013
BR 12 breast RMI 454	0.988	1:0.0859;6:0.7011;7:0.0233;8:0.1790; 17:0.0013;20:0.0095
muscle RMI 452	1.050	1:0.0810;6:0.6717;7:0.0242;8:0.1985; 17:0.0014;20:0.0232
SR2 brain	1.052	1:0.1083;6:0.7254;7:0.0169;8:0.1486; 17:0.0008
liver LV1 RMI	1.089	1:0.0806;6:0.6701;7:0.0247;8:0.2001; 17:0.0014;20:0.0231
inner bone (rez.2)	1.147	1:0.0671;6:0.5549;7:0.0198;8:0.2360; 15:0.0324;17:0.0011;20:0.0887
bone mineral (B200)	1.153	1:0.0665;6:0.5551;7:0.0198;8:0.2364; 15:0.0324;17:0.0011;20:0.0887
SB3 bone, cortical RMI 450	1.823	1:0.0341;6:0.3141;7:0.0184;8:0.3650; 17:0.0004;20:0.2681

F Data Table from ICRU49

Table F.1: Excitation energy for several elements and compounds according ICRU49. The I for liquids and solids not listed in the table, the elemental values times 1.13 are used.

Z of element	I in eV	I for a liquids and solids in eV
1	19.2 ± 0.4	19.2
6	78.0 ± 7.0	81.0
7	82.0 ± 2.0	82.6
8	95.0 ± 2.0	106.0
9	19.2 ± 0.4	112.0
11	149.0	
12	156.0	
14	173.0 ± 3.0	
15	173.0	
16	180.0	
17	174.0	180.0
19	190.0	
20	191.0 ± 8.0	
26	286.0 ± 9.0	
30	330.0 ± 10.0	

G Publications resulting from this thesis

Per-Reviewed

Henkner, Sobolevsky, Paganetti and Jäkel "The Feasibility to Test Fragmentation Models in Monte Carlo Codes with a Multi Layer Faraday Cup in Proton and Carbon Ion Beams"; Rad. Env. Biophysics, submitted

Henkner, Sobolevsky, Jäkel and Paganetti "Test of the nuclear interaction model in SHIELD-HIT and comparison to energy distributions from Geant4"; Phys. Med. Biol. (2009) N509-N517, page XV

Henkner, Bassler, Sobolevsky and Jäkel "Monte Carlo Simulations on the water-to-air stopping power ratio for carbon ion dosimetry"; Med. Phys. Vol. 36 (4) (2009) 1230-35; page XXV

Henkner, Bassler, Sobolevsky and Jäkel "Monte Carlo Simulations on the water-to-air stopping power ratio for carbon ion dosimetry"; Virt. J. of Biol. Phys. Reas. Vol. 17 (7) (2009)

Henkner, Jäkel and Bassler "Verifying the WEPL approximation for several tissue substitutes - A Monte Carlo Study"; International Journal of Radiation Oncology Biology Physics 72 (Suppl. 1) (2008) S669; page XXXI

Invited Talks

Henkner, Sobolevsky, Jäkel and Paganetti "Test of the Nuclear Interaction Model in the Monte Carlo Code SHIELD-HIT"; In Program and Abstracts of Heavy Ions in Therapy and Space Symposium 2009. Hrsg.: Deutsches Zentrum für Luft- und Raumfahrt (DLR). Köln (2009) 57. **Awarded by a Travel Award**

Conference Proceedings

Henkner, Sobolevsky and Jäkel "Improvements in the fragmentation model in SHIELD-HIT"; PTCOG 48, Abstract Book, Heidelberg, (2009)

Ackermann, Henkner, Parodi, Ellerbrock and Jäkel "Vergleich von relativen Reichweiten bei Protonen- und Kohlenstoffionenstrahlen"; TagungsCD der 39. Jahrestagung Oldenburg. Deutsche Gesellschaft für Medizinische Physik (DGMP) (2008)

Henkner, Jäkel, Sobolevsky and Bassler "What is the correct I-value for water?"; PTCOG

47, Abstract Book, Jacksonville, Florida (2008) 148-149

Henkner and Jäkel "Monte Carlo depth-dose calculations for different l-values in Heavy Ion Therapy"; Ion Beams in Biology and Medicine, Proceedings of the 39th Annual Conference of the German-Swiss Association for Radiation Protection and the 11th Workshop of Heavy Charged Particles in Biology and Medicine. Hrsg. J. Debus, K. Henrichs, G. Kraft. TÜV Media GmbH Köln, (2007) 37-38

NOTE

Test of the nuclear interaction model in SHIELD-HIT and comparison to energy distributions from GEANT4

K Henkner^{1,3}, N Sobolevsky², O Jäkel^{1,3} and H Paganetti⁴

¹ Department of Medical Physics in Radiation Oncology, German Cancer Research Center (DKFZ), Heidelberg 69120, Germany

² Department of Neutron Research, Institute for Nuclear Research of the Russian Academy of Sciences, Moscow 117312, Russia

³ Heidelberg Ion Beam Therapy Center (HIT), Heidelberg University Hospital, Heidelberg 69120, Germany

⁴ Department of Radiation Oncology, Massachusetts General Hospital and Harvard Medical School, Boston, MA 02114, USA

E-mail: Katrin.Henkner@med.uni-heidelberg.de

Received 18 March 2009, in final form 25 June 2009

Published 28 October 2009

Online at stacks.iop.org/PMB/54/N509

Abstract

Monte Carlo codes are widely used to simulate dose distributions in ion radiotherapy. The benchmark of the implemented physical models against experimental data plays an important role in improving the accuracy of the simulations. To estimate the accuracy of the inelastic cross sections in SHIELD-HIT, the simulated charge is compared to measured data from a Multi Layer Faraday Cup. In addition, the results are compared to GEANT4, which are already published. Furthermore, energy distributions are simulated with SHIELD-HIT07 and GEANT4.8.1. From a comparison of depth distributions and beam profiles of 100 and 200 MeV protons, we estimate the level of agreement of the two codes. Nuclear interactions predicted by SHIELD-HIT underestimate the total amount of measured charge. The energy distributions from SHIELD-HIT and GEANT4 show differences exceeding the statistical uncertainties of 2%. Due to a difference of the Bragg curve of 0.5 ± 0.3 mm on average, the mean difference in dose is 3.5% with a maximum deviation of 7% for the simulated cases.

1. Introduction

Therapy with protons has advantages compared to therapy with photons, since the beneficial dose profile with a sharp dose fall-off at the end of the particle range provides an accurate covering of the tumor volume and spares the healthy tissue. The Monte Carlo (MC) technique is a very common method for simulating dose distributions in radiation therapy. MC codes use electromagnetic (EM) and nuclear interaction models to estimate the primary, secondary

and neutron (Jiang *et al* 2005, Paganetti 2002) dose to the patient, the relative biological effectiveness (RBE), the distribution of positron emitters (Parodi and Enghardt 2000) and shielding solutions. To achieve accurate results with MC simulations, the code is benchmarked to experimental data.

There exist several electromagnetic (EM) and nuclear interaction models which can be used in the MC. The absorbed dose is mainly described by EM interactions, whereas nuclear interactions influence the spectra of secondary particles and neutron dose to the patient. Charge calculations from nuclear interactions in SHIELD-HIT are compared to experimental data with a Multi Layer Faraday Cup (MLFC) for 160 MeV protons. Experiments were performed at the Harvard Cyclotron Laboratory (HCL) by Gottschalk *et al* (1999) and Paganetti and Gottschalk (2003) and comparisons are already published for GEANT4 (Zacharatou Jarlskog and Paganetti 2008). Here we implement the set-up and scoring method in SHIELD-HIT.

Dose distributions from SHIELD-HIT (Dementyev and Sobolevsky 1999) and GEANT4 (Agostinelli *et al* 2003) are compared in this work. The agreement in range and dose is studied on Bragg curves and beam profiles. They are simulated downstream of air and interfaces of lung/air and bone/air for 100 MeV and 200 MeV protons.

2. Materials and methods

2.1. The MC code SHIELD-HIT

The version SHIELD-HIT07 is the most recent version of the Monte Carlo Code SHIELD-HIT. Stopping power values are calculated from the Bethe–Bloch equation, including the effective charge model, and for low energies with the Lindhard–Scharff formula. One can also implement stopping power data from ICRU 49 (ICRU 1993) for protons and He particles and from ICRU 73 (ICRU 2005) for heavier ions. The energy straggling can be simulated by Vavilov (1957) or Gaussian (Remizovich *et al* 1988, Rossi 1953) distributions. Multiple Coulomb scattering is simulated by a Gaussian distribution or according to Moliere’s (CERN 1994) theory. The multi-stage dynamical model (MSDM) (Botvina *et al* 1997) was developed at the Institute for Nuclear Research of the Russian Academy of Science (INR RAS, Moscow), and in the Joint Institute for Nuclear Research (JINR, Dubna) and is used for inelastic nuclear interaction modeling. As a default model it considers a fast cascade stage, which brings the interaction between the projectile and target to a sequence of binary collisions between nuclear constituents and/or produced hadrons (Toneev and Gudima 1983). Furthermore, it considers pre-equilibrium emission (Gudima *et al* 1983) and equilibrium de-excitation of residual nuclei with Fermi break up of light nuclei and evaporation/fission competition and multi-fragmentation of highly excited nuclei (Botvina *et al* 1987).

All simulations are performed with stopping power calculations from the Bethe–Bloch equation, Vavilov energy straggling and Moliere multiple scattering, which are successfully benchmarked in (Geithner *et al* 2006, Gudowska *et al* 2004 and Hollmark *et al* 2008).

2.2. The MC code GEANT4

The GEANT4 MC code is a result of a collaboration of many research facilities headed by CERN to simulate high-energy physics. It was completely redesigned and rewritten based on the GEANT3 simulation package using C++ and the object-oriented paradigm. It contains different methods and classes to provide basic tools for the simulation of particles, materials and physical processes in matter. GEANT4 is an open source program, which allows the user to modify the settings for a particular task. For each simulation, the user has to define the

Test of the nuclear interaction model in SHIELD-HIT and comparison to energy distributions from GEANT4 N511

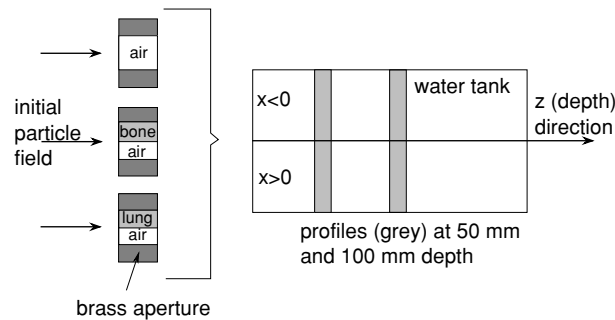


Figure 1. Arrangement to obtain interfaces of equal or different material used for dose calculations. The Bragg curves are scored along the z -axis and beam profiles along the x -axis.

incoming beam properties, the geometry and media and the physics settings. Therefore, the *PhysicsList* contains several EM and nuclear models addressing different types of interactions of particles with matter.

The physics settings for our calculations with GEANT4.8.1 are the standard electromagnetic model, low-energy parameterized elastic model, and the binary cascade model for inelastic scattering of protons and heavier ions.

2.3. The Multi Layer Faraday Cup model

The MLFC separates between nuclear and electromagnetic interactions, measures charge and is used to test the nuclear models of MC codes. The MLFC geometry is simulated by alternating brass and CH_2 sheets. The brass sheets have dimensions of $150 \times 150 \times 0.0254 \text{ mm}^3$ and a density of 8.489 g cm^{-3} . The thickness of the $150 \times 150 \text{ mm}^2$ polyethylene sheets is monotone increasing from 3.134 to 3.202 mm and their mean thickness is 3.17 mm. The incident proton beam properties are $E = 159.7 \text{ MeV}$ and $\Delta E = 0.5 \text{ MeV}$ and are taken from measurements at the HCL. A more detailed description of the properties and the design of the MLFC, the electronics, and the implementation in GEANT4 can be found in Gottschalk *et al* (1999) and Paganetti and Gottschalk (2003).

For the calculations with SHIELD-HIT, we modify the code to score the net charge in each geometrical zone and implement the geometry of the MLFC as given above. We use 20 million protons for each simulation.

2.4. Simulations on energy distributions

Bragg curves and lateral profiles for 100 MeV and 200 MeV protons are simulated with SHIELD-HIT07 and GEANT4.8.1. The initial proton field of 10 million particles is entering a 20 mm air gap, is afterwards shaped to a $100 \times 100 \text{ mm}^2$ field by brass apertures, passes 100 mm air and enters a $500 \times 500 \times 500 \text{ mm}^3$ water tank, in which the dose is scored. The Bragg curves are simulated within cylindrical water targets with radius of 10 mm and 100 mm to estimate the agreement of both codes concerning lateral scattering. The beam profiles are scored in 50 and 100 mm depth. The step size is 1 mm for Bragg curves and profiles. Within the 80 mm long apertures we simulate three different cases shown in figure 1. In the first case, the aperture is filled with air, in the second it is half filled with bone and air, and in the

Table 1. Overview of the composition and I-value of material used in the simulations.

Material	Air	Lung	Water	Bone
Composition	N 75.5%, O 24.5% (by weight)	According to ICRU 44 (ICRU 1989) for lung	2 H, 1 O (by composition)	According to ICRU 49 for compact bone
Density	0.0012 g cm ⁻³	0.25 g cm ⁻³	1.00 g cm ⁻³	1.85 g cm ⁻³
Excitation energy	85.108 eV/	75.201 eV/	74.991 eV/	91.902 eV/
I for SHIELD- HIT/GEANT4	85.7 eV	75.2 eV	75.0 eV	91.9 eV

last case there is half lung and air. The chemical compositions of the simulated materials are summarized in table 1. The mean I-values are slightly different for the two codes. Whereas SHIELD-HIT calculates the mean I-value of the material from its elemental values, GEANT4 uses the mean value given by the user. To achieve a certain mean I-value in SHIELD-HIT, the elemental values are varied until the best approximation of the desired mean value is achieved.

3. Results and discussion

3.1. The Nuclear interaction model in SHIELD-HIT

The simulated and experimental results for SHIELD-HIT and GEANT4 are shown in figure 2. The abscissa is shown in absolute values (no normalization), since the total number of incoming protons is known in the experiment and the simulations. Measurement uncertainties were negligible and are discussed in more detail in this reference. SHIELD-HIT underestimates the measurements up to channel 47 and overestimates them in the peak region, which is suppressed by a factor of 0.04 for illustration purposes. The simulations with GEANT4 fit very well. Only from channels 42–47 and in the peak an overshoot is observed. However, both codes show similar results in the peak region. The semi-logarithmical scale is used to show the electromagnetic peak. The peak height is predicted very well with both codes. SHIELD-HIT underestimates the build-up region, whereas GEANT4 fit very well to the measurements. The small positive signal beyond the EM peak is due to an imbalance of protons produced by neutrons entering and leaving the sheet. The fact that the MC does not agree with the measurement signal is probably due to measurement uncertainties from noise. The total charge with SHIELD-HIT is less than experimentally observed, which indicates, that the non-elastic cross section is very low.

3.2. Simulated energy distributions for SHIELD-HIT and GEANT4

3.2.1. Depth distributions. In figure 3, the deposited energy against water depth for a 100 MeV and 200 MeV proton beam is shown in MeV per cm³ and number of incident particles. Simulations with SHIELD-HIT are in lines and GEANT4 in symbols. Thick lines and circles represent dose distributions with 10 mm scoring radius and thin lines and triangles with 100 mm.

Within the plateau region the agreement of both codes is on average 2% and 5% for 100 mm and 10 mm scoring radii, respectively, and SHIELD-HIT is superior to GEANT4. Within a radius of 100 mm all particles contribute to the energy deposition, whereas the

Test of the nuclear interaction model in SHIELD-HIT and comparison to energy distributions from GEANT4 N513

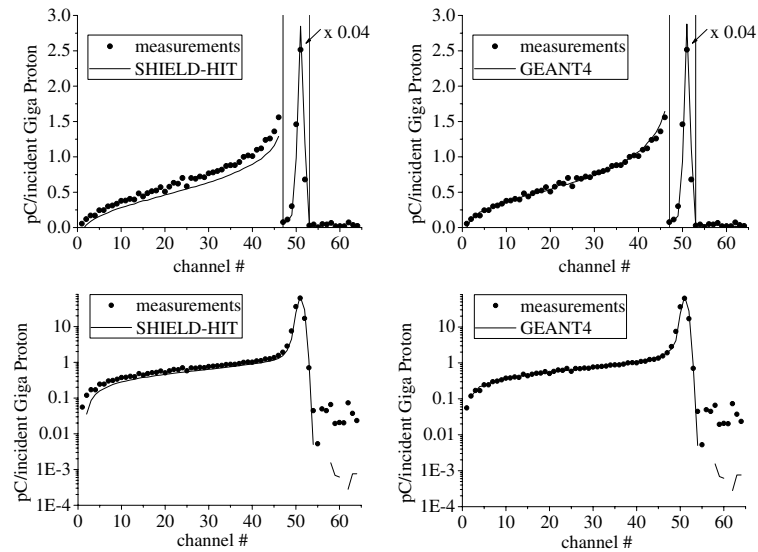


Figure 2. SHIELD-HIT (left) and GEANT4 (right) calculations (line) and experiment (circles). The ordinate shows absolute values and the abscissa is the channel number.

deposition within 10 mm is sensitive to lateral scattering. Furthermore, the statistical uncertainties are higher for the 10 mm radius.

A very dominant difference is observed in the Bragg curves. SHIELD-HIT results are shifted toward lower depth. Table 2 shows the mean difference of the distal fall-off of the Bragg peak for both codes and scoring radii. The number in brackets is the standard deviation from the difference with 100 and 10 mm radii. The Bragg peak number is taken from the position of the Bragg peak according to figure 3. For example, for 100 MeV in lung, (b), Bragg peak number 1 belongs to the peak with the shortest range and number 2 to the second largest for this energy. The first peak belongs to particles traveling through lung and the second from particles passing through air. In figure 3(c) for 100 MeV only one Bragg peak is obtained, because particles passing the bone part within the aperture already stop in the material. For 200 MeV two Bragg peaks are obtained again.

The mean difference is obtained from a fitting of the lateral fall-off at $y = 0$, because the Bragg peak and hence the 80% dose cannot be determined with a scoring of 1 mm bins. The mean difference depends on the material and on the primary energy, and is on average (average over the mean values) 0.5 ± 0.3 mm. SHIELD-HIT and GEANT4 Bragg curves do not agree due to several reasons. The development of SHIELD-HIT and GEANT4 was completely independent. Whereas the physical models in SHIELD were developed in Moscow, Russia, GEANT4 was developed at CERN, Switzerland. SHIELD-HIT is a heavy ion code and benchmarked on carbon ion depth-dose curves from GSI (Gesellschaft fuer Schwerionenforschung, Darmstadt, Germany). GEANT4 is tuned on proton curves measured at the Burr Proton Center (Boston, USA). Furthermore, the I-values used for the simulations were not exactly the same, but this has no major influence on the range (0.02 mm).

N514

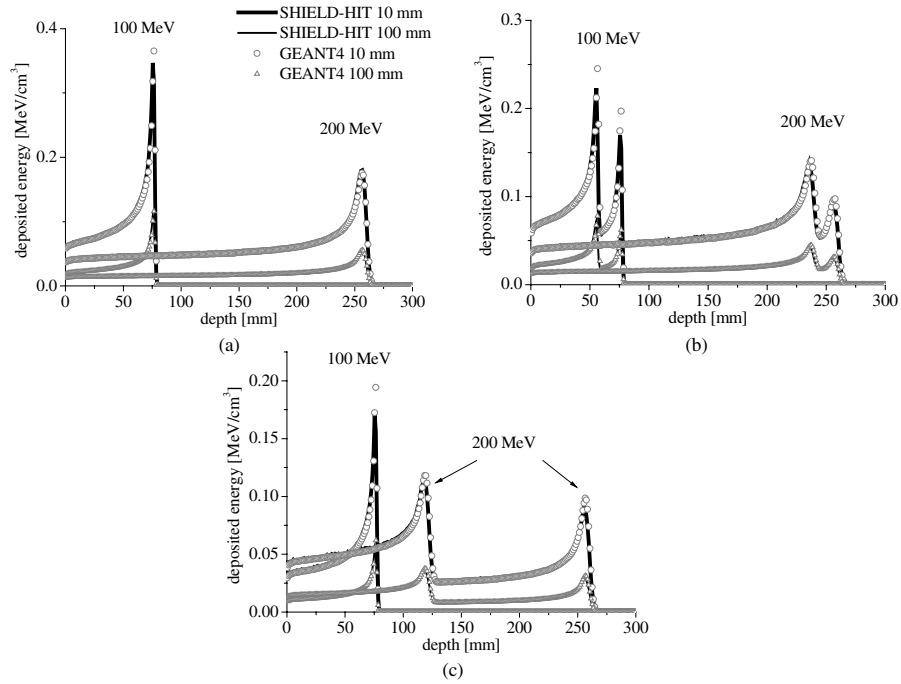
K Henkner *et al*

Figure 3. The deposited energy against water depth downstream of air (a), lung/air (b) and bone/air (c) are shown for 100 MeV and 200 MeV protons. Upper curves belong to a radius of 10 mm.

Table 2. Mean difference of Bragg peaks downstream of different material from figure 1. The difference is determined at the lateral fall-off of GEANT4 minus SHIELD-HIT.

Material	Energy (in MeV)	Bragg peak #	Difference (in mm)
Air	100		0.4 (0.03)
	200		0.3 (0.04)
Lung	100	1	0.1 (0.03)
	100	2	0.5 (0.02)
	200	1	1.1 (0.13)
	200	2	0.4 (0.13)
Bone	100		0.4 (0.05)
	200	1	0.8 (0.04)
	200	2	0.6 (0.06)

3.2.2. Beam profiles. The beam profiles are shown in figure 4. For $x > 0$ the beam traveled always through air. For $x < 0$ the beam passes through air or bone (shown in (a), (c) and (e)) and lung (in (b), (d) and (f)). Profiles at 50 mm depth for 100 MeV are shown in (a) and (b)

Test of the nuclear interaction model in SHIELD-HIT and comparison to energy distributions from GEANT4 N515

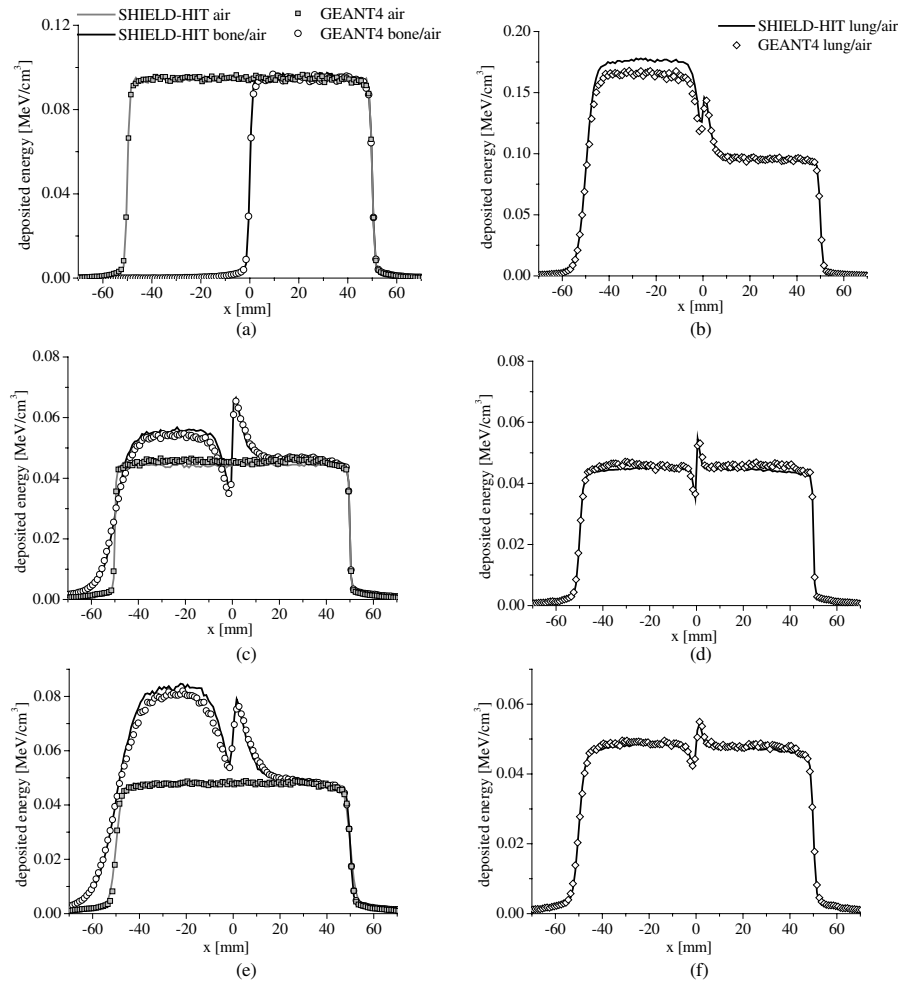


Figure 4. Beam profiles downstream of air and bone/air are shown on the left side, and lung/air is on the right. Profiles for 100 MeV protons in 50 mm are shown in (a) and (b). Profiles for 200 MeV protons in 50 mm are shown in (c) and (d), and profiles for 200 MeV protons in 100 mm are shown in (e) and (f). The ordinate is shown in absolute values.

and for 200 MeV in (c) and (d). The profiles at 100 mm depth for 200 MeV are shown in (e) and (f).

In (a) we show the results at 50 mm depth for 100 MeV protons. For simulations downstream of air and bone/air, both MC codes are identical within the statistical uncertainties of on average 2%. SHIELD-HIT differs about 7% for $x < 0$ from GEANT4 downstream of the interface lung/air in (b). This deviation comes from the difference of the Bragg curves, which has a big influence in the Bragg peak region. The Bragg peak in this case is at 65 mm and the profile is taken in 50 mm.

In (c) and (d) the mean deviations are 3.5% with maximum deviations up to 7% in the over- and undershooting area observed behind interfaces at $x = 0$. The minimum and maximum around $x = 0$ mm are caused by an imbalance of particles scattered to the left ($-x$) and right ($+x$) sides at the interface. The height of the maximum and minimum is larger for high-density differences (compare bone/air and lung/air in figures 4(c) and (d)).

The mean difference in (e) is 5% and at maximum 10% for $x \leq 0$, 5% in the overshoot region and 3.5% for $x > 0$. In (f) the mean difference is 3.5%.

4. Conclusion

The nuclear interaction model in SHIELD-HIT underestimates the total cross section measured with an MLFC, whereas the model in GEANT4 fits very well to the experiment. Total and differential cross sections for both MC codes should be compared to adjust the accuracy of the nuclear interaction model in SHIELD-HIT. Both codes simulate the EM peak correctly and a difference of the range with both codes is not determined with a mean spatial resolution of 3.2 mm in the MLFC. From measurements with a decreased slab thickness the range can be determined more accurately.

Measurements for heavier ions, e.g. carbon ions, would be useful to estimate the accuracy of the MC codes due to fragmentation processes, which, in contrary to protons, will have an effect on the depth-dose curve.

The simulated energy differs on average by 3.5%. SHIELD-HIT is up to 7% above GEANT4 downstream of the interfaces of lung/air and bone/air. This deviation is the result of a difference of the Bragg curves of 0.5 ± 0.3 mm on average toward lower depth for SHIELD-HIT. However, the difference does not affect the accuracy of radiotherapy as the MC used at therapy facilities are always benchmarked against the local system. To understand the differences in range, both codes should be compared to the same experimental data. In this comparison the treatment head, which is used in the experiment, should be carefully implemented in both codes.

Acknowledgment

Ms Henkner was supported by the German Research Foundation (DFG) under the contract number JA 1687/1-1.

References

- Agostinelli S *et al* (GEANT4 Collaboration) 2003 Geant4—a simulation toolkit *Nucl. Instrum. Methods A* **506** 250–303
- Botvina A S, Demityev A V, Smirnova N O, Sobolevsky N and Toneev V D 1997 *International Codes and Model Intercomparison for Intermediate Energy Activation Yields* p 307 NSC/DOC(97)-1, NEA/P&T No 14 (Paris: OECD)
- Botvina A S, Iljinov A S and Mishustin I N 1987 Statistical simulation of the break-up of highly excited nuclei *Nucl. Phys. A* **475** 663
- CERN 1994 Program Library Long Writeup W5013 GEANT, Detector Description and Simulation Tool, section PHYS325
- Demityev A V and Sobolevsky N M 1999 *Radiat. Meas.* **30** 553
- Geithner O, Andreo P, Sobolevsky N, Hartmann G and Jäkel O 2006 Calculation of stopping power ratios for carbon ion dosimetry *Phys. Med. Biol.* **51** 2279–92
- Gottschalk B, Platais R and Paganetti H 1999 Nuclear interactions of 160 MeV protons stopping in copper: a test of monte carlo nuclear models *Med. Phys.* **26** 2597–601
- Gudima K K, Mashnik S G and Toneev V D 1983 Cascade excitation model of nuclear reactions *Nucl. Phys. A* **401** 329

Test of the nuclear interaction model in SHIELD-HIT and comparison to energy distributions from GEANT4 N517

- Gudowska I, Sobolevsky N, Andreo P, Belkic D and Brahme A 2004 Ion beam transport in tissue-like media using the Monte Carlo code SHIELD-HIT *Phys. Med. Biol.* **49** 1935–58
- Hollmark M, Gudowska I, Belkić D, Brahme A and Sobolevsky N 2008 An analytical model for light ion pencil beam dose distributions: multiple scattering of primary and secondary ions *Phys. Med. Biol.* **53** 3477–91
- ICRU 1993 Stopping Powers and Ranges for Protons and Alpha Particles *ICRU Report 49* (Bethesda, MD: International Commission on Radiation Units and Measurements)
- ICRU 2005 Stopping of Ions Heavier than Helium *ICRU Report 73* (Bethesda, MD: International Commission on Radiation Units and Measurements)
- ICRU 1989 Tissue Substitutes in Radiation Dosimetry and Measurement Particles *ICRU Report 44* (Bethesda, MD: International Commission on Radiation Units and Measurements)
- Jiang H, Wang B, Xu X G, Suit H D and Paganetti H 2005 Effects of Hounsfield number conversion on CT based Monte Carlo dose calculations *Phys. Med. Biol.* **50** 4337–53
- Paganetti H 2002 Nuclear interactions in proton therapy: dose and relative biological effect distributions originating from primary and secondary particles *Phys. Med. Biol.* **47** 747–64
- Paganetti H and Gottschalk B 2003 Test of GEANT3 and GEANT4 nuclear models for 160 MeV protons stopping in CH₂ *Med. Phys.* **30** 1926–31
- Parodi K and Enghardt W 2000 Potential application of PET in quality assurance of proton therapy *Phys. Med. Biol.* **45** N151–6
- Remizovich V S, Rogozkin D B and Ryazanov M I 1988 *Fluctuations of Ranges of Charged Particles* (Moscow: Energoatomizdat) pp 32–99 chapters 2 and 3 (in Russian)
- Rossi B 1953 *High Energy Particles* (Englewood Cliffs, NY: Prentice-Hall) chapter 2
- Toneev V D and Gudima K K 1983 Particle emission in light and heavy ion reactions *Nucl. Phys. A* **400** 173
- Vavilov P V 1957 Ionizational losses of high energy heavy particles *J. Exp. Theor. Phys.* **32** 920–3 (in Russian)
- Zacharatou Jarlskog C and Paganetti H 2008 Physics settings for using the GEANT4 toolkit in proton therapy *IEEE Trans. Nucl. Sci.* **5** 1018–25

Monte Carlo simulations on the water-to-air stopping power ratio for carbon ion dosimetry

Katrin Henkner^{a)}

Department of Medical Physics in Radiation Oncology, German Cancer Research Center (DKFZ), Heidelberg 69120, Germany

Niels Bassler

Department of Medical Physics in Radiation Oncology, German Cancer Research Center (DKFZ), Heidelberg 69120, Germany; Department of Experimental Clinical Oncology, Aarhus University Hospital, Aarhus 8000, Denmark; and Department of Clinical Radiation Oncology, University of Heidelberg, Heidelberg 69120, Germany

Nikolai Sobolevsky

Department of Neutron Research, Institute for Nuclear Research of the Russian Academy of Sciences, Moscow 117312, Russia

Oliver Jäkel

Department of Medical Physics in Radiation Oncology, German Cancer Research Center (DKFZ), Heidelberg 69120, Germany and Heidelberg Ion Beam Therapy Center (HIT), Heidelberg University Hospital, Heidelberg 69120, Germany

(Received 19 June 2008; revised 28 January 2009; accepted for publication 29 January 2009; published 18 March 2009)

Many papers discussed the I value for water given by the ICRU, concluding that a value of about 80 ± 2 eV instead of 67.2 eV would reproduce measured ion depth-dose curves. A change in the I value for water would have an effect on the stopping power and, hence, on the water-to-air stopping power ratio, which is important in clinical dosimetry of proton and ion beams. For energies ranging from 50 to 330 MeV/u and for one spread out Bragg peak, the authors compare the impact of the I value on the water-to-air stopping power ratio. The authors calculate ratios from different ICRU stopping power tables and ICRU reports. The stopping power ratio is calculated via track-length dose calculation with SHIELD-HIT07. In the calculations, the stopping power ratio is reduced to a value of 1.119 in the plateau region as compared to the cited value of 1.13 in IAEA TRS-398. At low energies the stopping power ratio increases by up to 6% in the last few tenths of a mm toward the Bragg peak. For a spread out Bragg peak of 13.5 mm width at 130 mm depth, the stopping power ratio increases by about 1% toward the distal end. © 2009 American Association of Physicists in Medicine. [DOI: [10.1118/1.3085877](https://doi.org/10.1118/1.3085877)]

Key words: stopping power ratio, I value, dosimetry, Monte Carlo

I. INTRODUCTION

The recommended method to measure absorbed dose in ion beam therapy is to use air filled ionization chambers, calibrated in terms of absorbed dose to water in a reference beam quality. In the International Atomic Energy Agency (IAEA) Report No. TRS-398,¹ a quality correction factor k_Q is used to obtain the absorbed dose to water measured for any radiation quality. This quality correction factor crucially depends on the water-to-air stopping power ratio which is derived as a fluence weighted average over the particle spectra in water. The stopping power of fast charged particles is described by the Bethe formula and includes the I value in a logarithmic term. The I value, or mean excitation energy of an atom, as used in ICRU 49,² is defined as a weighted mean of all ionization and excitation potentials of an atom of the absorbing medium and is approximately proportional to the atomic number of the target medium. The I value can be obtained by integrating experimental data or from theoretical oscillator strength functions. An effective I value for compounds can be calculated by the Bragg additivity rule using

the elemental values as shown in ICRU 49. Common I values for water found in the literature are shown in Table I.

Calculating stopping power values via the Bethe formalism is implemented in most Monte Carlo (MC) codes. Currently, MC particle transport codes provide an accurate way of physical dose calculation for ion dosimetry. The most common codes in ion therapy are SHIELD-HIT,⁹ GEANT4,^{10,11} and FLUKA,^{12,13} where stopping power values, fluences, and dose distributions for all relevant particles can be calculated for a given geometrical setup. In this study, SHIELD-HIT07, which is the most recent version of SHIELD-HIT, is used for all calculations. SHIELD-HIT07 calculates stopping power values using the Bethe formula, including the effective charge, and for low energies using the Lindhard–Scharff formula. The recent improvement in SHIELD-HIT07 as compared to SHIELD-HITv2 used by Geithner *et al.*¹⁴ is the inclusion of Moliere's scattering theory according to Ref. 15 and is further discussed by Hollmark *et al.*¹⁶ Gaussian and Vavilov distributions for energy straggling, as well as Coulomb multiple scattering are also implemented in SHIELD-HIT07. To simulate

TABLE I. Overview of the common published mean ionization potentials for water and tabulated stopping power data found in ICRU reports.

I value I_w for water (eV)	Reference	Tabulated stopping power data
67.2	ICRU73 (Ref. 3)	From lithium up to argon
75 ± 3	ICRU49 (Ref. 2)	For protons and alpha particles
80.8 ± 2	Paul <i>et al.</i> (Ref. 4)	
80	Bichsel <i>et al.</i> (Refs. 5 and 6)	
78.4 ± 1	Kumazaki <i>et al.</i> (Ref. 7)	
78	Schardt <i>et al.</i> (Ref. 8)	

inelastic nuclear interactions the multistage dynamical model is used.¹⁷

With the increasing interest in ion beam radiotherapy and the desire to raise the accuracy of ion beam dosimetry to the same level as in conventional radiotherapy, the discussion about the correct value of the ionization potential for water became increasingly important during recent years. The largest source of uncertainty in the determination of absorbed dose was identified in TRS-398 as the water-to-air stopping power ratio. Furthermore, the inconsistency of the I values in the ICRU 49 and 73 (Ref. 3) reports, which were used in the analysis of stopping power ratios by Geithner *et al.* needs to be resolved.

Several benchmark studies using different I values for water have been published so far. For example, Geithner *et al.* used a mixture of tabulated stopping power values: ICRU 49 for proton and alpha particles and ICRU 73 for lithium to argon ions and internal SHIELD-HIT calculations, with the Bethe and Lindhard-Scharff formula, for potassium and calcium. Sihver *et al.*,¹⁸ Gudowska *et al.*,¹⁹ and Pshenichnov *et al.*²⁰ used a value of 75 eV and Matsufuji *et al.*²¹ used the value of 67.2 eV. (The used value in Ref. 20 is from a personal communication with Mr. Matsufuji in 2007.) They all compared their calculations with the same experimentally derived depth-dose curves from GSI (Gesellschaft für Schwerionenforschung mbH, Darmstadt) or NIRS (National Institute of Radiological Sciences, Chiba). Most calculated results match the behavior of depth-dose curves very well, but many modeled results have in common that the peak positions had to be shifted in order to reach agreement with the experimental data. Hence, an absolute Bragg peak position is a difficult benchmark to achieve, which is noted in only some of the mentioned papers.

The inconsistency of the I value for various reports for water was first discussed by Paul *et al.*, who concluded that the value of 67.2 eV, as assumed in ICRU 73, is too low [The value of 67.2 eV is not mentioned in ICRU 73, it is from a personal communication of P. Sigmund to H. Paul (see Ref. 26) in our Ref. 4.]. Since a change in the I value would change the stopping power, also the water-to-air stopping power ratio which is used in ion chamber dosimetry, would change. In our work we reanalyze the impact of different sets of I values for water and air on the stopping

power ratio for a pristine Bragg peak from a carbon ion pencil beam, and a spread out Bragg peak (SOBP) in a more consistent way as compared to the previous analysis in Geithner *et al.*

II. METHODS

II.A. Stopping power

The energy loss of fast ions to atomic electrons is described by the Bethe theory, as shown in ICRU 49. The mass stopping power is defined as the stopping power per unit distance traversed normalized to the media density ρ and is given by $S/\rho = -(1/\rho)dE/dx$, where E is the particle energy and x is the path length. It was first calculated by Bohr and later on by Bethe and Bloch using quantum mechanical approaches, and its final expression is presented by the Bethe equation,

$$\frac{S}{\rho} = \frac{4\pi r_e^2 m c^2}{\beta^2} \frac{1}{u} \frac{z_{\text{eff}}^2 Z}{A} \left(\frac{1}{2} \ln \frac{2m c^2 \beta^2 W_{\text{max}}}{1 - \beta^2} - \beta^2 - \ln I - \frac{C}{Z} - \frac{\delta}{2} \right). \quad (1)$$

Here r_e is the classical electron radius, m is the rest electron mass, $\beta = v/c$ is the particle speed divided by the speed of light, Z and A are the atomic number and atomic mass of the target medium respectively, and z_{eff} is the effective charge of the projectile. I is the mean ionization potential and W_{max} is the maximum energy transfer in a single collision. δ is the density correction, which in SHIELD-HIT07 is considered according to Sternheimer *et al.*,²² whereas the shell correction C and the Barkas and Bloch corrections are omitted. The Barkas and Bloch corrections, which are not shown in Eq. (1), are discussed in Ref. 2.

In SHIELD-HIT07 the mean ionization potential I for compounds is calculated using Bragg's additivity rule (see Chap. 2.52 in Ref. 2) from the I values I_i of the compound elements by the relative weight w_i , the atomic mass A_i , and the atomic number Z_i of element i , according to the equation

$$\ln I = \frac{[\sum_i w_i (Z_i/A_i) \ln I_i]}{\sum_i w_i (Z_i/A_i)}. \quad (2)$$

To adjust the mean excitation energy of a compound to a desired value, we change the I values of the elements in SHIELD-HIT07 appropriately. Considering the compound constituents of the elements according to Table 2.1 in ICRU 49, a mean I value for the compound is used for the stopping power and depth-dose curve calculations in SHIELD-HIT07.

In order to estimate the accuracy of the stopping power calculations in the MC, we compared the stopping power data for carbon ions from MSTAR (Ref. 23) with the values calculated with SHIELD-HIT07 ($I_w = 75$ eV). For energies around 1 MeV, which refer to a particle range of about 0.0038 mm, the deviation to the MSTAR data is up to 12%. For 2 MeV (corresponding to a range of 0.036 mm) up to 4 MeV (corresponding range of 0.096 mm), we obtained deviations between 6.3% and 0.9%. For energies above 10 MeV and in a range of 0.43 mm, the deviation is less than 0.2%.

TABLE II. An overview of the combination of I values for water and air, which we use for stopping power ratio calculations.

set #	I_{air}	I_w	Source for air value	Source for water value	Water value used by
1	82.8 eV	67.2 eV	ICRU 73	ICRU 73	Matsufuji <i>et al.</i> (Ref. 21)
2	85.7 eV	67.2 eV	ICRU 49	ICRU 73	
3	Tabulated stopping power data	Tabulated stopping power data	ICRU 49 for proton and alpha particles, and ICRU 73 for heavier ions	ICRU 49 for proton and alpha particles, and ICRU 73 for heavier ions	Geithner <i>et al.</i> (Ref. 14)
4	85.7 eV	75 eV	ICRU 49	ICRU 49	Gudowska <i>et al.</i> (Ref. 19) and Shiver <i>et al.</i> (Ref. 18)
5	85.7 eV	80.8 eV	ICRU 49	Paul <i>et al.</i>	Paul <i>et al.</i> (Ref. 4)

II.B. Stopping power ratio

In heavy ion dosimetry the applied dose is verified by air filled ionization chamber measurements. The absorbed dose is obtained by detecting the charge emerging from the ionized air in the cavity of the chamber. From the measured charge M in air, the absorbed dose to water D_w is calculated via a chamber specific calibration factor N and the beam quality correction factor k_Q . D_w is the basic reference quantity used for most clinical applications and is calculated according to equation,

$$D_w = M * N * k_Q. \quad (3)$$

k_Q is recommended in IAEA TRS-398 as a beam quality correction factor to obtain the absorbed dose in water in a radiation field with quality Q from the dose measured in an air filled ionization chamber calibrated in absorbed dose to water in a reference beam quality Q_0 according to the equation,

$$k_Q = \frac{(S_{w/\text{air}})_Q \left(\frac{W_{\text{air}}}{e} \right)_Q p_Q}{(S_{w/\text{air}})_{Q_0} \left(\frac{W_{\text{air}}}{e} \right)_{Q_0} p_{Q_0}}. \quad (4)$$

Here, Q is the beam quality during measurements, i.e., in an ion beam in our case, Q_0 is the reference beam quality which is a ^{60}Co beam, W_{air}/e is the mean energy required to produce an electron-ion pair in air, p is a chamber specific correction factor, and $S_{w/\text{air}}$ is the water-to-air stopping power ratio. The factor p is a product of various factors correcting for changes in the radiation field by introducing an air filled ionization chamber into the field in water. These are effects of the chamber wall, the air cavity, and the central electrode.

The stopping power ratio $S_{w/\text{air}}$ according to IAEA TRS-398, is given as a particle fluence weighted average over all primary and secondary particles and is derived by calculating the dose ratio via track-length fluence $\Phi_{E,i,w}$ for water w from particle i with energy E and mass stopping power $S(E)/\rho$ for water and air with SHIELD-HIT07,

$$S_{w/\text{air}} = \frac{\sum_i \int_{E_i > \Delta}^{E_{\text{max}}} \Phi_{E,i,w} (S_i(E)/\rho)_w dE}{\sum_i \int_{E_i > \Delta}^{E_{\text{max}}} \Phi_{E,i,w} (S_i(E)/\rho)_{\text{air}} dE}. \quad (5)$$

Here, Δ is the Monte Carlo transport cutoff specific energy, which was set to 25 keV/u in our calculations.

A first approximation for the stopping power ratio of a monoenergetic beam is the ratio of stopping powers of the primary ion. As suggested by Paul *et al.*, it can be expressed by the ionization potential I_w for water and I_{air} for air, as well as the classical electron rest mass m and speed of the incoming particle v by the equation

$$\frac{(S(E)/\rho)_w}{(S(E)/\rho)_{\text{air}}} = \frac{0.5551 \ln(2mv^2/I_w)}{0.4992 \ln(2mv^2/I_{\text{air}})}. \quad (6)$$

The calculation of the stopping power ratio in our simulations differs slightly from the approach used by Geithner *et al.* We neglect the contribution of particles with energy below 25 keV/u, stopping in the volume, which result in a very small contribution to the stopping power ratio of less than 0.00015%, according to our calculations. We use SHIELD-HIT07 for dose calculations in water via track-length fluences, and also for further stopping power ratio calculations, whereas Geithner *et al.* used an external program to obtain the stopping power ratios from SHIELD-HITV2.

Table II shows five sets of I values which we use for stopping power ratio calculations of monoenergetic carbon pencil beams. In addition, we calculate the stopping power for particles from ^1H up to ^{12}C in water and air, and the track-length fluence for a water cylinder with length of 300 mm and a radius of 100 mm, which is divided into equal slices along the axis of symmetry with 0.1 mm thickness in the Bragg peak region and 1 mm elsewhere.

The stopping power ratio is also calculated for a spread out Bragg peak which is built by adding weighted carbon depth-dose curves from 252 up to 270 MeV/u. The SOBPs has a homogenous dose plateau from 130 to 143.5 mm in depth. Here, we use set 5 (Table II).

III. RESULTS

The comparison between a calculated depth-dose curve of 270 MeV/u carbon ions (black line) and the water-to-air stopping power ratio [Eq. (5), gray squares] for this energy and using the I values in set 5 of Table II is shown in Fig. 1. The stopping power ratio has a maximum in the sharp dose fall off of the depth-dose curve behind the Bragg peak. The fact that these two maxima do not coincide is not surprising since also the stopping power reaches a maximum beyond the Bragg peak. The dose maximum appears at a somewhat shallower depth because of the decreasing particle fluence.

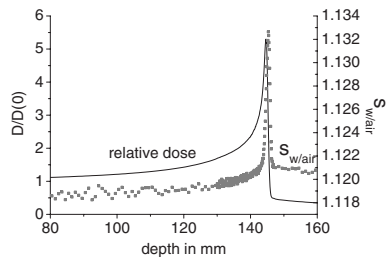


FIG. 1. The depth-dose distribution, relative to the entrance dose, and the stopping power ratio for a 270 MeV/u carbon ion beam in water for set 5 are shown.

The effect of varying the I value (taken from Table II) on the stopping power ratio is demonstrated in Fig. 2 for a 270 MeV/u carbon ion pencil beam. The derived stopping power ratio from ICRU tabulated stopping power data, set 3 (thick black solid line), shows an unphysical minimum in the plateau region and has a 1.3% lower peak as compared to the ratio calculated with the Bethe formula and a consistent I value of 67.2 eV, set 1 (thin black solid line). An increase to $I_w = 80.8$ eV will reduce the stopping power ratio from 1.13, as recommended by the IAEA, down to 1.119. Furthermore, the $S_{w/air}$ is not constant within the whole plateau region. An increase of 0.2% toward the Bragg peak is observed (from 1.118 to 1.12 for set 5). Shown as “+” is the $S_{w/air}$ as a result of Eq. (6) for I values from set 5. It differs by about 0.2% from the SHIELD-HIT07 calculations.

ICRU tabulated (set 3) and SHIELD-HIT07 calculated values with set 5 for carbon energies from 50 up to 330 MeV/u are shown in Fig. 3. The maximal derived stopping power ratio in the tail of the depth-dose curve decreases with increasing energy. For the ICRU tabulated values (set 3) the stopping power ratio is noticeably higher for 50 MeV/u. The values $S_{w/air}$ are larger than in Fig. 4 in Geithner *et al.*, which is due to a higher resolution of 0.1 mm.

Figure 4 shows the stopping power ratios for different

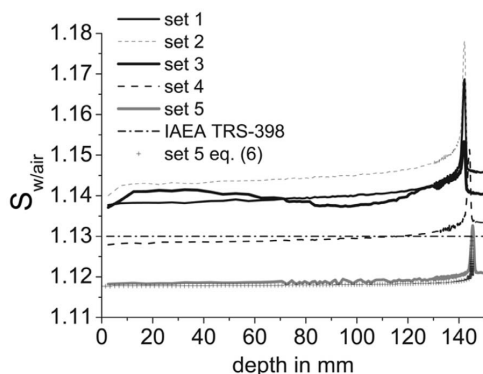


FIG. 2. Shown is the water-to-air stopping power ratio $S_{w/air}$ for sets 1–5 from Table II for a 270 MeV/u carbon ion beam as a function of the depth in water. The $S_{w/air}$ is compared to the IAEA constant value of 1.13.

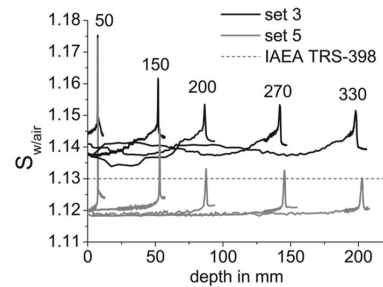


FIG. 3. Water-to-air stopping power ratio for sets 3 and 5 (Table II) as a function of depth in water for beams of different energy in MeV/u. The fluctuations in the data set calculated with ICRU tabulated data (set 3) are present for all beam energies.

beam energies, displayed as a function of the residual range. The residual range of the ions is 0 mm at the Bragg peak, increases toward the entrance region, and has a negative value behind the Bragg peak. Plotted this way, the ratios for 50, 150, 200, 270, and 330 MeV/u are almost identical and the stopping power ratio, closed to the Bragg peak, is constant at 1.12. For the lowest energy, the ratio increases at maximum by as much as 6% toward the Bragg peak.

In Fig. 5 we show the influence of secondary particles on the water-to-air stopping power ratio for a 330 MeV/u carbon ion beam of I values from set 5. Therefore, we successive added one particle type after another. In the plateau region there is no influence from secondary particles on the $S_{w/air}$, whereas at the end of the range, adding heavier particles decreases the maximal derived $S_{w/air}$. Adding particle after particle to the $S_{w/air}$ from carbon and proton ions increases the ratio by 0.12% for helium, 0.08% for beryllium and lithium, and 0.01% for boron particles (sum over all particles). The influences of hydrogen, deuterium, and tritium on the total ratio are 0.21%, 0.58%, and 0.65%, respectively.

The stopping power ratio (gray squares) for a 13.5 mm wide SOBP (black line) is displayed in Fig. 6, showing an increase at the proximal start of the SOBP region. The ratio is very inhomogeneous, increasing toward the peak, having a surge at the beginning of the SOBP from 1.119 to 1.121, further increasing to 1.125 at the end of the plateau, and

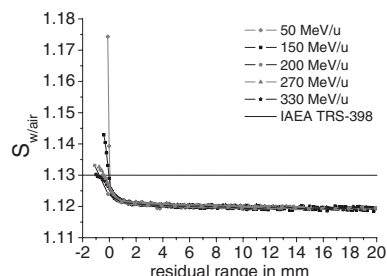


FIG. 4. Water-to-air stopping power ratios for set 5 are shown according to the residual range of carbon beams for 5 different beam energies in water.

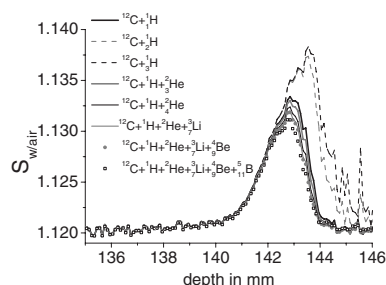


Fig. 5. Shown is the influence of secondary particles on the water-to-air stopping power ratio for a 330 MeV/u carbon ion beam. Compared to the $S_{w/air}$ from all particles, it increases for tritium to the end of the particle range.

having a maximum of 1.128 in the tail region of the SOBP. The overall variation, however, is only about 1%.

IV. DISCUSSION

The resulting stopping power ratio calculated from ICRU 73 and 49 tabulated stopping power data shows a minimum in the plateau region, whereas the calculations with a single set of I values show a monotone behavior (set 3, Figs. 2 and 3). As mentioned in Ref. 4 the variations in the plateau region are due to the use of tabulated stopping power data from ICRU 73 for ions $Z > 2$ and ICRU 49 for proton and alpha particles.

Since the stopping power ratio is slightly increasing (about 0.2%) from the beam entrance toward the Bragg peak (set 5, Fig. 2), a practical method to correct for this effect should be considered, e.g., a parametrization of the correction as a function of the modulation depth and range. In the last 1 mm toward the Bragg peak, the stopping power ratio increases by up to 2% for energies above 150 MeV/u and up to 6% for 50 MeV/u (Fig. 3). This effect is restricted to a very narrow region and will thus only be relevant for plane parallel ionization chambers at low energies.

Considering the inconsistency of I values in ICRU 73 and 49, and following Paul *et al.*, set 5 in Table II would best represent the existing water-to-air stopping power ratio. The ratio of 1.12 for a residual range above a few millimeters is overestimated by the IAEA constant value of 1.13. There-

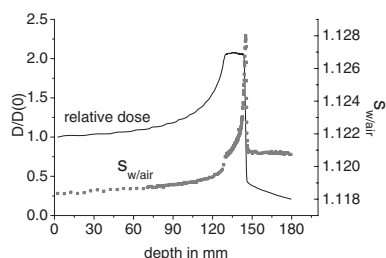


Fig. 6. Dose distribution (line) of a SOBP and the calculated stopping power ratio (squares) as a function of depth in water.

fore, following Eq. (4), the beam quality correction factor k_Q would be overestimated by 1% and will decrease the accuracy of dose measurements. The calculated absorbed dose to water from an ionization chamber will result in an under dosage in ion beam therapy when using the IAEA constant. This should be taken into account in the clinical application of ion beams.

The influence of secondary particles on the $S_{w/air}$ of a 330 MeV/u carbon ion beam is only observed in the tail region of the Bragg peak. The total water-to-air stopping power ratio is increased by 0.65% for carbon+tritium ions only and decreases by adding heavier particles. The position of the maximal derived $S_{w/air}$ for carbon+tritium is shifted by 0.07 mm toward higher depth as compared to the total ratio. This is due to the higher range of secondary particles building the fragment tail behind the Bragg peak.

It should be noted that the I value of air has an effect on the water-to-air stopping power ratio, as well. Shown in Fig. 2 for set 1 and set 2, a decrease in the I value for air to 82.8 eV increases the stopping power ratio by about 0.43%. The ICRU data for air should therefore be reinvestigated as well.

The uncertainty in the determination of the stopping power ratio from dose calculations via the track-length is estimated by propagating the uncertainties in the track-length calculations for each particle. The resulting overall mean uncertainty up to the Bragg peak and beyond is $\pm 0.11\%$ and $\pm 0.12\%$, respectively. The corresponding maximum uncertainties are $\pm 0.46\%$ and $\pm 0.63\%$, respectively. This evaluation is, however, only approximated and was done for a 270 MeV/u carbon ion beam only. Additional statistical uncertainties in the $S_{w/air}$ calculations are within $\pm 0.06\%$. The uncertainty of the I value also has a considerable effect on the accuracy of the stopping power ratio. For example, in ICRU 49, the I value is given by 75 ± 3 eV, which results in an uncertainty in the stopping power ratio for 270 MeV/u carbon ions of $\pm 0.5\%$ in the plateau region and up to $\pm 1.5\%$ toward the end of the range, which is due to a higher range for higher I and vice versa.

In a spread out Bragg peak, the former recommendation will also lead to an under dosage. The ratio, however, sharply increases toward the distal end of the SOBP from 1.121 to 1.128, and the under dosage is reduced toward the end of the SOBP. The absorbed dose to water measured for a uniform SOBP with a constant stopping power ratio would in reality be inhomogeneous. Since this effect depends on the depth modulation of the SOBP and, furthermore, the absorbed doses applied in ion beam therapy are modulated to account for the variation in the biological effect, it is not straightforward to correct for this effect and a more detailed analysis is needed here.

V. CONCLUSION

With respect to the work done by Geithner *et al.* there are some discrepancies concerning depth-dose curve and stopping power ratio calculations. Especially when comparing their results with the work done by Gudowska *et al.*,¹⁹ depth-

dose curves shown in Ref. 14 do not seem to be consistent with regard to the absolute positions of the Bragg peak in depth.

As noted already by Paul *et al.*,⁴ the tabulated data in the ICRU 73 report have to be reviewed. A new and valid I value for water is very important for the calculation of stopping powers, which again has an impact on depth-dose distribution and the stopping power ratio.

When adopting a new value for I_w , the IAEA constant $S_{w/air}$ of 1.13 should also be revisited. If an I value in the region of 80.8 eV is chosen, the $S_{w/air}$ would be reduced to 1.119 (mean over the plateau region). Finally, it should be discussed whether the use of a constant value, which would not take into account an increase toward the Bragg peak, is practical for pencil beams and SOBPs.

The accuracy of the stopping power ratio depends mostly on the accuracy of the I value and would be influenced by the maximum energy transfer W_{max} in Eq. (1), as well. The effect of W_{max} on the $S_{w/air}$ and the accuracy in the track-length calculation needs further study.

Since the I value for air has an effect on the stopping power ratio, it should be analyzed if an I value of 82.8 eV (ICRU 73) or 85.7 eV (ICRU 49) or 88.8 eV (Paul *et al.*)⁴ is appropriate.

ACKNOWLEDGMENT

This project is supported by the German Research Foundation (DFG) under Contract No. JA 1687/1-1. Niels Bassler acknowledges support from the Danish Cancer Society.

^aElectronic mail: k.henkner@dkfz.de

¹IAEA 2000 Technical Reports Series 398, "Absorbed dose determination in external beam radiotherapy," International Code of Practice for Dosimetry, Vienna.

²ICRU 49, "Stopping powers and ranges for protons and alpha particles," International Commission on Radiation Units and Measurements, Bethesda, Maryland (1993).

³ICRU 73, "Stopping of ions heavier than helium," International Commission on Radiation Units and Measurements, Oxford University Press (2005).

⁴H. Paul, O. Geithner, and O. Jäkel, "The influence of stopping powers upon dosimetry for radiation therapy with energetic ions," *Adv. Quantum Chem.* **52**, 290–308 (2007).

⁵H. Bichsel and T. Hiraoka, "Energy loss of 70 MeV protons in elements,"

Nucl. Instrum. Methods Phys. Res. B **66**, 345–351 (1992).

⁶H. Bichsel, T. Hiraoka, and K. Omata, "Aspects of fast-ion dosimetry," *Radiat. Res.* **153**, 208–219 (2000).

⁷Y. Kumazaki, T. Akagi, T. Yanou, D. Suga, and Y. Hishikawa, "Determination of the mean excitation energy of water from proton beam ranges," *Radiat. Meas.* **42**, 1683–1691 (2007).

⁸D. Schardt, P. Steidl, M. Krämer, U. Weber, K. Parodi, and S. Brons, "GSI Scientific Report 2007," GSI Report No. 2008-1, July 2008.

⁹A. V. Dementyev and N. M. Sobolevsky, "SHIELD—Universal Monte Carlo hadron transport code: Scope and applications," *Radiat. Meas.* **30**, 553–557 (1999).

¹⁰J. Allison *et al.*, "Geant4 developments and applications," *IEEE Trans. Nucl. Sci.* **53**(1), 270–278 (2006).

¹¹S. Agostinelli *et al.*, "Geant4—A simulation toolkit," *Nucl. Instrum. Methods Phys. Res.* **506**, 250–303 (2003).

¹²A. Fasso, A. Ferrari, J. Ranft, and P. R. Sala, "FLUKA: A multi-particle transport code," CERN-2005-10 (2005), INFN/TC_05/11, SLAC-R-773.

¹³G. Battistoni *et al.*, "The FLUKA code: Description and benchmarking," *Proceedings of the Hadronic Shower Simulation Workshop 2006*, Fermilab 6–8 September 2006, edited by M. Albrow and R. Raja, AIP Conference Proceedings 896, 31–49 (2007).

¹⁴O. Geithner, P. Andreo, N. Sobolevsky, G. Hartmann, and O. Jäkel, "Calculation of stopping power ratios for carbon ion dosimetry," *Phys. Med. Biol.* **51**, 2279–2292 (2006).

¹⁵CERN Program Library Long Writeup W5013, GEANT, Detector Description and Simulation Tool, (1994), Sec. PHYS325.

¹⁶M. Hollmark, I. Gudowska, D. Belkić, A. Brahme, and N. Sobolevsky, "An analytical model for light ion pencil beam dose distributions: Multiple scattering of primary and secondary ions," *Phys. Med. Biol.* **53**, 3477–3491 (2008).

¹⁷A. S. Botvina, A. V. Dementyev, O. N. Smirnova, N. M. Sobolevsky, and V. D. Toneev, "MSDM—multistage dynamical model," In *International Codes and Model Intercomparison for Intermediate Energy Activation Yields*, edited by R. Michel and P. Nagel, NSC/DOC(97)-1, NEA/P&T No 14, OECD, Paris, p. 307, (1997).

¹⁸L. Sihver, D. Schardt, and T. Kanai, "Depth-dose distributions of high-energy carbon, oxygen and neon beams in water," *Jpn. J. Med. Phys.* **18**, 1–21 (1998).

¹⁹I. Gudowska, N. Sobolevsky, P. Andreo, D. Belkić, and A. Brahme, "Ion beam transport in tissue-like media using the Monte Carlo code SHIELD-HIT," *Phys. Med. Biol.* **49**, 1933–1958 (2004).

²⁰I. Pshenichnov, I. Mishustin, and W. Greiner, "Distribution of positron-emitting nuclei in proton and carbon-ion therapy studied with GEANT4," *Phys. Med. Biol.* **51**, 6099–6112 (2006).

²¹N. Matsufuji, A. Fukumura, M. Komori, T. Kanai, and T. Khono, "Influence of fragment of relativistic charged particles on heavy ion radiotherapy," *Phys. Med. Biol.* **48**, 1605–1623 (2003).

²²R. M. Sternheimer and R. F. Peierls, "General expression for the density effect for the ionization loss of charged particles," *Phys. Rev. B* **3**, 3681–3692 (1971).

²³H. Paul and A. Schinner, 2002 MSTAR—Stopping power for light ions. Available at <http://www.exphys.uni-linz.ac.at/stopping>.

workflow. This workflow is expected to contribute to the easy implementation of hospital information system and medical safety.

Materials/Methods: The Japanese IHE-RO committee was organized from users and vendors at February 2006 to develop the workflow suitable for the CPOE/EMR environment. We divided the process of radiation treatment into (1) initial visiting, (2) treatment planning, (3) daily treatment, (4) finish of treatment, (5) patient follow-up. We analyzed this workflow of physicians, nurses and technologist and cooperation between the radiotherapy information system and other CPOE/EMR systems.

Results: We studied the process of the clinical procedure and arranged suitable actors that the IHE technical frameworks defined in the Radiology, Laboratory, Cardiology and Radiation Oncology domains. The actors include the Order Placer (OP), Order Filer (OF), Treatment Management System (TMS), Therapy delivery system (TDS), Therapy planning system (TPS), Acquisition Modality, Contourer, Geometric Planner, Dosimetric Planner, Dose Displayer, Archive and Image Display (ID). The Japanese IHE-RO committee is making the workflow document that describes the communication methods among systems. We are discussing the role of Oncology Information System and Treatment Management System to improve the radiation workflow. We think that we can easily migrate to IHE system from existing system using the IHE-RO workflow. We also discuss how to follow-up patients after treatment using Electronic Medical Record. We are planning to perform Japanese connection and demonstration in the JASTRO 2009.

Conclusions: This paper reports the activity of Japanese IHE-RO committee. We think that the analysis of the radiation department workflow is very important for implementation of the information system. By using this workflow we can realize an easy and effective implementation of the system. Workflow analysis contributes to IT promotion in a radiotherapy department, and also seamless communication is useful for medical safety.

Author Disclosure: Y. Ando, None; N. Tsukamoto, None; O. Kawaguchi, None; M. Mukai, None; H. Numasaki, None.

3111 Verifying the WEPL Approximation for Several Tissue Substitutes - A Monte Carlo Study

K. Henkner¹, O. Jäkel^{1,2}, N. Bassler^{1,3}

¹German Cancer Research Center, Heidelberg, Germany, ²Heidelberg Ion Beam Therapy Center (HIT), Heidelberg University Hospital, Heidelberg, Germany, ³Department of Experimental Clinical Oncology, Aarhus University Hospital, Aarhus, Denmark

Purpose/Objective(s): For the calculation of treatment plans in ion therapy, the stoichiometric calibration of CT Hounsfield units is used to convert the tissue electron densities in the CT image into water equivalent path lengths (WEPLs). The WEPL is used for range calculations of ion beams in therapy planning. Here, each medium is treated like water and the fragmentation process and the spectrum of fragments in the tissue is assumed to be the same as in water. To estimate how good this approach is, we calculated longitudinal and lateral dose distributions of carbon ion beams in water, and compared these with calculations where we substituted the material in the entry region with cortical bone, lung, adipose tissue substitutes and metal implants.

Materials/Methods: We used the Monte Carlo code SHIELD-HIT07 to calculate monoenergetic pencil beams and rectangular beams for carbon ions. The stopping power data is calculated by the Bethe-Bloch and the Lindhard-Scharff formula. For depth-dose determination, we simulated a cylindrical water phantom of length 30 cm, radius 10 cm, and scoring radii of 10 cm and 1 cm along the central beam. For the lateral dose distribution we applied a beam with a FWHM of 5 mm. The chemical composition of the substitutes is related to the "Gammex 467 Electron Density CT Phantom". We compared depth-dose and lateral dose curves in water equivalent depths to obtain changes in the fragment spectrum, using different substitute thickness.

Results: Preliminary results indicate no significant change in the fragmentation spectrum, when having a 1 cm tissue substitute in the plateau region instead of water. For a 1 cm bone substitute, the deviation of the Bragg peak position compared to water is less than 0.1%. For 5 cm bone substitute it is about 0.5% and increases with increasing thickness and density of the substitute.

Conclusions: The WEPL is a good approximation. For tissue substitutes up to several cm, the perturbation of the fragment spectrum and the shift of the Bragg peak position compared to water are very small. Expecting a perturbation of the fragment spectrum behind thick bone tissue, metal implants and in the central beam region, further studies are necessary.

Author Disclosure: K. Henkner, None; O. Jäkel, None; N. Bassler, None.

3112 A Novel Applicator System for HDR Treatment of Endometrial and Cervical Cancer

E. I. Parsai, Z. Zhang, J. J. Feldmeier

University of Toledo Health Science Campus, Toledo, OH

Purpose/Objective(s): A novel HDR applicator system has been designed to treat gynecological cancers with following specific goals in mind: 1) Provide the ability to do volumetric image based patient specific dosimetry, 2) ability to significantly spare the surrounding critical structures, 3) moving away from Manchester point calculation and computing target based dose instead, and 4) provide patient comfort. It is expected that this system will provide all the functionality of a Fletcher-Suit Delclos (FSD) device and has more versatility in treatment of these cancers.

Materials/Methods: A disposable applicator manufactured* from plastic material with inflatable partitioned sections to displace rectum and bladder away from the radiation source has been designed. The Tandem constructed from rigid plastic mimics the conventional tandem used in FSD device, with a balloon system attached to it. Catheters are assembled to the sectioned balloon to provide pathway for delivery of dose to vaginal fornices and other affected areas. The balloons are inflated after insertion in patient and secured in position to exact patient size. Sectional CT or MRI is acquired to perform patient specific dosimetry.

Acknowledgments

It was a pleasure for me to write this thesis between October 2006 and September 2009 at the German Cancer Research Center (DKFZ) in Heidelberg and I like to thank all the people who made this thesis possible. They are:

Prof. Dr. Wolfgang Schlegel, head of the department, for giving me the opportunity of growing up at DKFZ already for my Diploma thesis. **Prof. Dr. Oliver Jäkel**, head of the Heavy Ion Group, and my direct supervisor at DKFZ, for offering me several possibilities on training and to present my work at international conferences. I am grateful for his support in my six month research stay at the Physics Research Group at the Massachusetts General Hospital in Boston, USA. **Prof. Dr. Nikolai Sobolevsky**, one of the SHIELD-HIT developers and my contact person in all technical questions about SHIELD-HIT. **Prof. Dr. Harald Paganetti** from MGH, Boston, for supporting my stay at MGH and the Geant4 calculations. **Prof. Dr. Steffen Trimper**, my supervisor at the Martin-Luther University Halle-Wittenberg. **Dr. Dieter Schardt**, for providing me with his experimental data. **Dr. Niels Bassler**, for several discussions and setting up the group computer cluster. **Benjamin Ackermann** for his help in the GSI measurements. **Dr. Basit Athar** for the carbon ion Geant4 calculations and the collaboration in the neutron dose study. **Rochus Herrmann** for FLUKA calculations. **Christoph Döttling** for his support on computers.

I am grateful to all colleagues at the Department of Medical Physics in Radiation Oncology, especially to the **group members of the Heavy Ion Group** who made my stay a very enjoyable period of my life. I wish to thank the colleagues at the **Physics Research Group and Francis H. Burr Proton Center at MGH**, for the pleasant stay.

I wish to thank my grandparents for their support during my studies as well as my family.

Lastly, but most importantly I thank my fiancé Thomas for his patience and care during this time. My life had never been more enjoyable till I have met you.

Eidesstattliche Erklärung

Ich erkläre an Eides statt, dass ich die vorliegende Arbeit

Monte Carlo Simulations for Dosimetry and Treatment Planning in Hadron Therapy

selbstständig und ohne fremde Hilfe verfasst und keine als die von mir angegebenen Quellen und Hilfsmittel benutzt habe.

Die wissenschaftliche Arbeit wurde in gleicher oder ähnlicher Form an keiner anderen wissenschaftlichen Einrichtung zur Erlangung eines akademischen Grades eingereicht.

Heidelberg, January 22, 2010

Dipl.-Phys.(Med.) Katrin Henkner

LEBENS LAUF

■ Persönliche Daten

Name: Katrin Henkner
Geburtstag/ -ort: 16.05.1983, Grimma

■ Ausbildung

Seit Oktober 2009 Heidelberg Ionenstrahl Therapie Centrum (HIT)
- Medizinphysikexpertin

Oktober 2006 -
September 2009 Promotion an der Martin-Luther Universität Halle-
Wittenberg
- Verfassung der Arbeit am Deutschen
Krebsforschungszentrum Heidelberg;
- Gruppe: "Heavy Ion Therapy Project"
Promotionsarbeit zum Thema:
"Monte Carlo Simulations for Dosimetry and Treatment
Planning in Hadron Therapy"

Oktober 2005 -
September 2006 Diplomarbeit am Deutschen
Krebsforschungszentrum Heidelberg;
- Gruppe: "Physical Quality Assurance in Radiation
Therapy"
zum Thema: "Verwendung eines 2D-
Ionisationskammerarrays zur Bestimmung von
Feldparametern eines Linearbeschleunigers"

Oktober 2001 -
September 2005 Studium der Medizinischen Physik (Diplom) an der
Martin- Luther Universität Halle- Wittenberg;

